

REPORT DOCUMENTATION PAGE

*Form Approved
OMB No. 0704-0188*

Public reporting burden for this collection of information is estimated to average 1 hour per response, including the time for reviewing instructions, searching data sources, gathering and maintaining the data needed, and completing and reviewing the collection of information. Send comments regarding this burden estimate or any other aspect of this collection of information, including suggestions for reducing this burden to Washington Headquarters Service, Directorate for Information Operations and Reports, 1215 Jefferson Davis Highway, Suite 1204, Arlington, VA 22202-4302, and to the Office of Management and Budget, Paperwork Reduction Project (0704-0188) Washington, DC 20503.

PLEASE DO NOT RETURN YOUR FORM TO THE ABOVE ADDRESS.

1. REPORT DATE (DD-MM-YYYY) 15-06-2002			2. REPORT DATE FINAL		3. DATES COVERED (From - To) 01-10-1993-31-12-2001	
4. TITLE AND SUBTITLE Thermo -Fluid Mechanic Study of Thermoacoustic Devices			5a. CONTRACT NUMBER 5b. GRANT NUMBER N000149410063			
6. AUTHOR(S) Andrea Prosperetti Cila Herman Omar Knio			5c. PROGRAM ELEMENT NUMBER 61153N 5d. PROJECT NUMBER 5e. TASK NUMBER 5f. WORK UNIT NUMBER			
7. PERFORMING ORGANIZATION NAME(S) AND ADDRESS(ES) Dept. of Mechanical Engineering Johns Hopkins University/ 3400 N. Charles Baltimore, MD 21218-2686				8. PERFORMING ORGANIZATION REPORT NUMBER		
9. SPONSORING/MONITORING AGENCY NAME(S) AND ADDRESS(ES) Office of Naval Research ONR 331 800 N. Quincy St. Arlington, VA 22217-5660				10. SPONSOR/MONITOR'S ACRONYM(S) 11. SPONSORING/MONITORING AGENCY REPORT NUMBER		
12. DISTRIBUTION AVAILABILITY STATEMENT Approved for public release, Distribution Unlimited						
13. SUPPLEMENTARY NOTES						
14. ABSTRACT The research described is articulated in three parts. (a) Development and study of a quasi-one-dimensional, time-domain, non-linear, simplified model of a thermoacoustic device. (b) Multidimensional numerical modeling based on low-Mach-number asymptotics. (c) Visualization of high-speed oscillating temperature fields in a thermoacoustic stack by means of holographic interferometry combined with high-speed cinematography.						
15. SUBJECT TERMS Thermoacoustic, Refrigeration, Flow visualization, low-Mach-Number approximation, multiscale computing						
16. SECURITY CLASSIFICATION OF: a. REPORT b. ABSTRACT c. THIS PAGE Unclassified Unclassified Unclassified			17. LIMITATION OF ABSTRACT -----	18. NUMBER OF PAGES 101	19a. NAME OF RESPONSIBLE PERSON 19b. TELEPHONE NUMBER (Include area code)	

115 045

Part I

SIMPLIFIED MODELLING

OF

THERMOACOUSTIC DEVICES

A. Prosperetti

Contents

1	Introduction and Summary	I-3
1.1	Publications	I-3
1.2	Personnel	I-5
2	A Simplified Nonlinear Model of Thermoacoustic Devices	I-6
2.1	Introduction	I-6
2.2	Mathematical Model	I-7
2.3	Boundary conditions	I-9
2.4	Exchange Terms	I-10
2.5	Numerical Method	I-18
2.6	Results	I-22
2.6.1	A Prime Mover	I-22
2.6.2	Piston-Driven Refrigerator	I-26
2.6.3	Thermoacoustic Refrigerator Coupled with Prime Mover	I-28
2.7	Conclusions	I-32
References	I-33
3	Linear and Weakly Nonlinear Theory of Thermoacoustic Devices	I-37
3.1	Introduction	I-37
3.2	The First-Order Problem	I-40
3.3	Second-Order Problem	I-41
3.4	The Landau Equation	I-42
3.4.1	Linear regime	I-43
3.4.2	Nonlinear regime	I-44
3.5	Conclusions	I-46
References	I-48
4	Bubble Screens	I-49
4.1	Mathematical model	I-50
4.2	Results	I-52
4.3	Conclusions	I-55
References	I-57

Chapter 1

Introduction and Summary

This part of the ONR-funded project was principally devoted to the development of a simplified time-domain nonlinear model of thermoacoustic devices.

The starting point for the development of this model is the observation that, in most cases, the size of these devices in the direction normal to the wave fronts is usually greater than the length scales parallel to the wave fronts. This circumstance suggests the use of a well-known approximation in Fluid Mechanics, consisting in the averaging of the conservation equations over the cross section.

A difficulty inherent in this procedure is that averaging removes information of the exchange processes of momentum and energy between the working fluid and the solid structure in contact with it. These processes are of crucial importance in thermoacoustic phenomena and, therefore, it is essential to reintroduce the lost information into the mathematical model, albeit approximately.

This has been the greatest difficulty encountered in this work, but we believe to have found a satisfactory solution as described in Chapter 2. This chapter contains a detailed exposition of the model and its rationale and presents several numerical examples which demonstrate its versatility: a prime mover, an externally driven thermoacoustic refrigerator, and a combined prime mover/refrigerator system. In addition to the analytical formulation of the model, we have also developed a robust numerical method for the solution of the equations.

The outcome of this work is therefore a complete (if approximate) fully nonlinear time-domain model of thermoacoustic devices – the first of its kind. While certainly incomplete, the model agrees reasonably well with data, is numerically efficient and, at the very least, it is useful to compare design options.

In parallel with this work, we have also developed a time-domain formulation of the linear theory of thermoacoustic devices, as well as a weakly non-linear theory; these results are described in chapter 3.

The last part of the study concerns a different topic – the propagation of pressure waves through layers of bubbly liquids. The motivation of the work is the possible use of such systems as parametric arrays for the generation of low-frequency sound, and also for the attenuation of strong waves; these results are described in chapter 4.

1.1 Publications

The work has given rise to the following publications, which are here listed with the respective abstracts:

Watanabe, M., Prosperetti, A. & Yuan, H., A Simplified Model for Linear and Nonlinear Processes in Thermoacoustic Prime Movers. Part I. Model and linear theory. *J. Acoust. Soc. Am.* **102, 3484-3496, 1997**

ABSTRACT: A simplified quasi-one-dimensional model of thermoacoustic devices is formulated by averaging the conservation equations over the cross section. Heat transfer and drag effects are introduced by means of suitable coefficients. While the primary motivation for this work is the development of a model approximately

valid in the nonlinear regime, the focus of this paper is the proper formulation of the transfer coefficients and the analysis of the linear problem. The accuracy of the model is demonstrated by comparison with existing more precise theories and data. Examples of devices with variable cross section demonstrate the flexibility of the approach.

Yuan, H., Karpov, S. & Prosperetti, A., A Simplified Model for Linear and Nonlinear Processes in Thermoacoustic Prime Movers. Part II. Nonlinear Oscillations. *J. Acoust. Soc. Am.* **102, 3497-3506, 1997**

ABSTRACT: The simplified quasi-one-dimensional model of thermoacoustic devices formulated in Part I (Watanabe, Prosperetti, & Yuan, *J. Acoust. Soc. Am.* **102**, 3484-3496, 1997) is studied in the nonlinear regime. A suitable numerical method is described which is able to deal with the steep waveforms that develop in the system without inducing spurious oscillations, appreciable numerical damping, or numerical diffusion. The results are compared with some experimental ones available in the literature. Several of the observed phenomena are reproduced by the model. Quantitative agreement is also reasonable when allowance is made for likely temperature non-uniformities across the heat exchangers.

Karpov, S. & Prosperetti, A., Linear Thermoacoustic Instability in the Time Domain. *J. Acoust. Soc. Am.* **103, 3309-3317, 1998**

ABSTRACT: An approximate time-domain analysis of the development of the thermoacoustic instability in gas-filled tubes is developed by exploiting the difference between the instability time scale and the period of standing waves. The perturbation results compare very favorably with the exact frequency-domain theory of Rott. The perturbation results are further simplified by introducing a short-stack approximation which is numerically much simpler and only slightly less accurate. An approximate expression for the critical temperature gradient accounting for viscous effects and other design features is also derived. In addition to the fundamental mode of a tube closed at both ends, the theory includes higher modes as well as open-end boundary conditions.

Karpov, S. & Prosperetti, A., Nonlinear Saturation of the Thermoacoustic Instability. *J. Acoust. Soc. Am.* **107, 3130-3147, 2000**

ABSTRACT: A weakly nonlinear theory of the thermoacoustic instability in gas-filled tubes is developed in the timer domain by exploiting the difference between the instability time scale and the period of standing waves. By carrying the expansion to fourth order in the perturbation parameter, explicit results for the initial growth, nonlinear evolution, and final saturation are obtained. The dependence of the saturation amplitude upon the temperature difference in the stack, the tube geometry, stack plate spacing, Prandtl number, and other parameters is illustrated.

Karpov, S. & Prosperetti, A., A Nonlinear Model of Thermoacoustic Devices. *J. Acoust. Soc. Am.*, accepted

ABSTRACT: This paper presents a nonlinear, time-domain model of thermoacoustic devices based on cross-sectional averaged equations. Heat transfer perpendicular to the device axis – which lies at the core of thermoacoustic effects – is modelled in a novel and more realistic way. Heat conduction in the solid surfaces surrounding the fluid medium is included. Contrary to the previous versions of this model (Watanabe et al., *J. Acoust. Soc. Am.* **102**, 3484, 1997), the present version does not require artificial damping and is numerically robust. The model performance is illustrated on several examples: a prime mover, an externally driven thermoacoustic refrigerator, and a combined prime mover/refrigerator system.

Karpov, S., Prosperetti, A., & Ostrovsky, L., Nonlinear oscillations of bubble layers. *J. Acoust. Soc. Am.*, accepted

ABSTRACT: Due to the large compressibility of gas bubbles, layers of a bubbly liquid surrounded by pure liquid exhibit many resonances that can give rise to a strongly non-linear behavior even for relatively low-level excitation. In an earlier paper (Druzhinin et al., *J. Acoust. Soc. Am.* **100**, 3570, 1996) it was

pointed out that, by exciting the bubbly layer in correspondence of two resonant modes, so chosen that the difference frequency also corresponds to a resonant mode, it might be possible to achieve an efficient parametric generation of a low-frequency signal. The earlier work made use of a simplified model for the bubbly liquid that ignored the dissipation and dispersion introduced by the bubbles. Here a more realistic description of the bubble behavior is used to study the nonlinear oscillations of a bubble layer under both single- and dual-frequency excitation. It is found that a difference-frequency power of the order of 1% can be generated with incident pressure amplitudes of the order of 50 kPa or so. It appears that similar phenomena would occur in other systems, such as porous water-like or rubber-like media.

Karpov, S., Nonlinear Phenomena in Thermoacoustics and Bubbly Liquids
Doctoral dissertation, The Johns Hopkins University, May 2000.

1.2 Personnel

The work described here is the result of a collaboration among the following people:

1. A. Prosperetti, PI
2. L. Ostrovsky, Zel Technology/NOAA ETL, Boulder, CO
3. M. Watanabe, doctoral student (currently associate professor at Fukuoka University, Japan)
4. H. Yuan, post-doctoral fellow
5. S. Karpov, doctoral student (currently with PTC, Needham, MA)

Chapter 2

A Simplified Nonlinear Model of Thermoacoustic Devices

2.1 Introduction

In recent years there has been a renewal of interest in thermoacoustic devices, both prime movers and heat pumps (for reviews see The foundations of the linear theory were firmly established in a well-known series of papers by

The linear analytical theory of thermoacoustic devices has reached a high degree of maturity thanks to the work of many authors (Rott 1969, 1976, 1980, 1983, and others; Merkli & Thomann 1975; Yazaki et al. 1980, 1987; Arnott et al. 1991, 1992, 1994, 1995; Atchley 1992, 1994; Atchley & Kuo 1994; Atchley et al. 1990a, 1990b, 1992; Olson & Swift 1994; Raspet et al. 1993; Swift 1992; Swift & Keolian 1993; Wheatley et al. 1983; Karpov & Prosperetti 1998); excellent reviews have been provided by Wheatley (1986) and Swift (1988).

Progress in the direction of nonlinear phenomena has been slower due to the complexity of the phenomena. Only limited analytical results are available (Gaitan & Atchley 1993; Gopinath et al. 1998; Bauwens 1996, 1998; Karpov & Prosperetti 2000). The bulk of the work has been carried out with the aid of the sophisticated numerical techniques necessary to tackle this multi-dimensional, multi-scale problem (Cao et al. 1996; Worlikar & Knio 1996, 1998, 1999; Worlikar et al. 1998; Besnoin & Knio 2001).

The difficulty of the nonlinear problem is unfortunate, because this is the situation presenting the greatest practical interest. For example, the very fact that the thermoacoustic instability in a prime mover ultimately saturates at a finite pressure amplitude is an obvious consequence of nonlinearity.¹ More subtly, as pointed out by Worlikar et al. (1998), some of the differences between linear theory and experiment encountered by Atchley et al. (1990a) are to be attributed to nonlinearity already at drive ratios as low as 2%. Furthermore, it may be argued that the effective exploitation of thermoacoustic systems requires operation in the nonlinear regime. The strongly nonlinear resonators described by Ilinskii et al. (1998) are a particularly interesting possibility.

We have therefore thought it desirable to formulate a simplified nonlinear model of intermediate complexity between the linear, frequency-domain treatments typical of the linear theory, and the full multi-dimensional calculations of direct numerical simulations. For this purpose, we have used a method very common in the study of nonlinear compressible flows and shock waves, namely the integration of the governing equations over the cross section of the device (see e.g. Crocco 1958; Landau and Lifshitz 1959). This procedure has led us to a quasi-one dimensional model that, although approximate, is realistic and appears useful to further an understanding of thermoacoustic devices in the nonlinear regime.

¹Heat flow limitations in the heat exchangers can also affect the saturation level quantitatively; the existence of the saturation phenomenon itself, however, is a nonlinear effect.

The averaging of the equations over the cross section of the device has the effect of removing a detailed information of the exchange processes of momentum and energy between the working fluid and the solid structure in contact with it. These processes – and in particular the second one – lie of course at heart of thermoacoustic phenomena and, therefore, it is essential to reintroduce the lost information into the mathematical model with a sufficient degree of realism. This is a crucial point discussed in detail in section 2.4.

As a result of our work over the past years, we have developed a general time-domain, fully nonlinear model of thermoacoustic devices that is capable of predicting the response of such systems to cross-sectional area variations, stack position, fluid properties, and many other design variables. While the model is not exact due to the averaging over the cross section, in the frequency domain and for small amplitudes it reduces to the standard linear theory. In addition, it is able to describe nonlinear phenomena such as the finite-amplitude saturation of the thermoacoustic instability while, at the same time, remaining substantially simpler than a truly multidimensional model. We thus hope that our model can be useful in filling the current gap in the levels of description available for thermoacoustic systems.

2.2 Mathematical Model

Most thermoacoustic devices consist of an acoustic resonator containing different heat transfer components (stack, heat exchangers, etc.). Typically the dimensions along the direction of the particle displacement – the resonator “axis” – is much longer than the transverse one and this circumstance suggests the basis for our approximation. We recast the governing equations in an integrated form over the cross-section of the device thus reducing the model to one dimension in space (along the tube axis) and time. Effects taking place in the orthogonal directions (friction, heat transfer, etc.) are to be accounted for approximately by the introduction of suitable terms in the equations.

Consider a thermoacoustic device consisting of a duct of variable area $S(x)$. The coordinate x is taken along the axis of the device that is not necessarily straight. Upon integrating the equation of continuity over the volume delimited by two neighboring cross sections $S(x)$ and $S(x + dx)$ we find the well-known relation

$$\frac{\partial \langle \rho \rangle}{\partial t} + \frac{1}{S} \frac{\partial S \langle \rho u \rangle}{\partial x} = 0, \quad (2.1)$$

where ρ is the gas density, u the velocity in the x -direction, and the angle brackets indicate the cross sectional average,

$$\langle \dots \rangle = \frac{1}{S(x)} \int_{S(x)} dS (\dots). \quad (2.2)$$

The vanishing of the exact velocity field on the lateral walls of the duct has been applied to obtain (2.1).

Similarly, the momentum equation in the x -direction becomes

$$\frac{\partial \langle \rho u \rangle}{\partial t} + \frac{1}{S} \frac{\partial}{\partial x} (S \langle \rho u^2 \rangle) + \frac{\partial \langle p \rangle}{\partial x} + \frac{1}{S} (\langle p \rangle - \bar{p}) \frac{dS}{dx} = - \frac{\mathcal{P}}{S} (\boldsymbol{\tau} \cdot \mathbf{n})_x. \quad (2.3)$$

Here p is the gas pressure, $\boldsymbol{\tau}$ the viscous stress tensor, and the overline denotes the average over the “wetted perimeter” \mathcal{L} , i.e. the lines along which the cross-section S is cut by solid boundaries,

$$\bar{p} = \frac{1}{\mathcal{P}} \oint_{\mathcal{L}} p d\ell \quad (2.4)$$

where \mathcal{P} is the length of \mathcal{L} . The unit normal \mathbf{n} is directed *into* the fluid region. The viscous component τ_{xx} has been neglected in deriving (2.3).

Before turning to the energy equation we introduce an assumption widely used in Gas Dynamics (see e.g. Crocco 1958 for a discussion), namely that the fields are approximately uniform over the cross section.². As

²The assumption of uniform pressure over the cross section has already been used in Thermoacoustics e.g. by Tominaga (1995)

a consequence of the cross sectional uniformity, $\langle p \rangle \simeq \bar{p}$ and we may disregard correlation terms writing the average of products as products of averages. This approximation is addressed quantitatively in section 5. The effects of non-uniformities, such as wall drag, is accounted for in an approximate manner. For the wall shear stress we write

$$\frac{\mathcal{P}}{S}(\bar{\tau} \cdot \bar{\mathbf{n}})_x \equiv \mathcal{D}(\rho u); \quad (2.5)$$

the explicit form of $\mathcal{D}(\rho u)$ will be discussed in detail in the next section.

With these assumptions, and the omission henceforth of explicit indication of cross-sectional averages, the continuity (2.1) and momentum (2.3) equations become

$$\frac{\partial \rho}{\partial t} + \frac{1}{S} \frac{\partial}{\partial x} (S \rho u) = 0, \quad (2.6)$$

$$\frac{\partial \rho u}{\partial t} + \frac{1}{S} \frac{\partial}{\partial x} (S \rho u^2) + \frac{\partial p}{\partial x} = -\mathcal{D}(\rho u). \quad (2.7)$$

The cross-sectional averaging procedure applied to the energy equation of a perfect gas gives

$$\frac{\partial}{\partial t} \left[\frac{1}{\gamma-1} p + \frac{1}{2} \rho u^2 \right] + \frac{1}{S} \frac{\partial}{\partial x} \left[u S \left(\frac{\gamma}{\gamma-1} p + \frac{1}{2} \rho u^2 \right) \right] = \frac{\mathcal{P}}{S} \bar{\mathbf{q}} \cdot \bar{\mathbf{n}}, \quad (2.8)$$

where \mathbf{q} is the heat flux and γ is the ratio of specific heats. The most intense heat transfer occurs in the directions normal to x and, accordingly, the effect of axial conduction q_x has been disregarded. This approximation is of course invalid at the ends of the tube. We return on this point in subsection 2.1 below. Similar to (2.5), we introduce two heat transfer operators \mathcal{H}, \mathcal{Q} by writing

$$\frac{\mathcal{P}}{S} \bar{\mathbf{q}} \cdot \bar{\mathbf{n}} \equiv \rho c_p \mathcal{H}(T_w - T) - \frac{\partial T_w}{\partial x} \mathcal{Q}(c_p \rho u), \quad (2.9)$$

where $T_w(x, t)$ is the (possibly time-dependent) temperature of the solid structure (e.g. the stack plates) at x . The second term accounts for the distortion of the temperature distribution due to the flow in the presence of a mean temperature gradient. This ansatz is suggested by the structure of the temperature distribution given by the exact linear theory and will be discussed in detail below in section 2.4.

Now, upon using (2.6) and (2.7) to eliminate the time derivatives of ρ and u , the energy equation (2.8) becomes³

$$\frac{\partial p}{\partial t} + u \frac{\partial p}{\partial x} + \frac{\gamma p}{S} \frac{\partial}{\partial x} (S u) = (\gamma - 1) \left[c_p \rho \mathcal{H}(T_w - T) - \frac{\partial T_w}{\partial x} \mathcal{Q}(\rho u) + u \mathcal{D}(\rho u) \right]. \quad (2.10)$$

The last term in the right-hand side represents the rate of conversion of mechanical to thermal energy by friction.

The mathematical description of the fluid is completed by the specification of an equation of state. We assume that the averaged variables are related by the perfect gas equation

$$p = R \rho T, \quad (2.11)$$

where R is the universal gas constant divided by the gas mass.

Closure of the model requires knowledge of the temperature distribution $T_w(x, t)$ along the axis of the device. We use once more a cross-sectional average over the solid material that constitutes the stack. Although it is not necessary to specify the geometrical structure of the stack, for ease of exposition we will think of it as constituted by a set of parallel plates. Area averaging is justified by the fact that the plates are usually thin; a similar remark would apply to pin stacks or other geometrical arrangements. In this way one finds

$$\rho_s c_s \frac{\partial T_w}{\partial t} = \frac{1}{S_s} \frac{\partial}{\partial x} \left(k_s S_s \frac{\partial T_w}{\partial x} \right) - c_p \left[\rho \mathcal{H}(T_w - T) - \frac{\partial T_w}{\partial x} \mathcal{Q}(\rho u) \right], \quad (2.12)$$

³We assume that c_p is a constant, in agreement with our treatment of the gas as perfect.

where ρ_s , c_s , k_s , and S_s are the density, specific heat, thermal conductivity, and cross sectional area of the plates. The heat exchangers are modelled in a similar way, except that their thermal conductivity is taken to be infinite so that their temperature is spatially uniform.⁴ For the sake of simplicity, in the examples that follow we assume that the stack plates are in perfect thermal contact with the cold and hot heat exchangers.

Away from the stack region, one could use a similar formulation for the resonator tube walls, or one could couple the model equations with the conduction equations in the walls. For simplicity, we have chosen to assume that the tube wall temperature is prescribed.

2.3 Boundary conditions

A variety of boundary conditions can be associated with the mathematical model described in the previous section depending on the situation that it is desired to model. For example, for the prime mover case with standing waves, it might be reasonable to assume that the end walls of the tube are rigid, so that the velocity vanishes:

$$u = 0 \quad \text{at } x = 0, \quad x = L. \quad (2.13)$$

The momentum equation (2.7) then implies that

$$\frac{\partial p}{\partial x} = 0 \quad \text{at } x = 0, \quad x = L. \quad (2.14)$$

Equations (2.6) and (2.10) written at the endpoints ($x = 0, L$) give then

$$\frac{\partial \rho}{\partial t} + \rho \frac{\partial u}{\partial x} = 0, \quad (2.15)$$

$$\frac{\partial p}{\partial t} + \gamma p \frac{\partial u}{\partial x} = (\gamma - 1) \rho c_p \mathcal{H}(T_w - T). \quad (2.16)$$

Upon eliminating $\partial u / \partial x$ one finds

$$\frac{\partial T}{\partial t} = \frac{\gamma - 1}{\gamma} \frac{T}{p} \frac{\partial p}{\partial t} + \mathcal{H}(T_w - T). \quad (2.17)$$

This relation shows that a knowledge of p at the boundary completely specifies T . No additional boundary conditions on this quantity are therefore necessary. Since the heat transfer term \mathcal{H} is very small outside the stack region, this relation then essentially implies the adiabatic pressure-temperature relation of perfect gases.

In general, the relation (2.17) will result in a temperature jump from the T given by this relation to the end-wall temperature. This is a consequence of the neglect of axial conduction in the derivation of the energy equation (2.10). Axial conduction would introduce a term $\partial^2 T / \partial x^2$, important only near the end walls, the role of which would be to re-establish continuity of temperature by means of a thin boundary layer. The temperature in this layer would adjust itself so as to match the value given by (2.17). This is an essentially passive process with negligible effects on the temperature distribution elsewhere in the device and can therefore be disregarded. If desired, however, the expression for \mathcal{H} can be adjusted to give a heat transfer coefficient at the tube ends.

For the case of standing waves forced by a piston, as in a refrigerator arrangement, one might consider two limit cases. The piston may be located at a velocity antinode, corresponding to a pressure node. In this case one may assume a vanishing pressure disturbance and an imposed fluid velocity at this location. Conversely, for a piston located at a pressure antinode, one may use an imposed pressure condition and a zero velocity condition.

⁴It appears possible to modify this equation to account for possible heat flow limitations of the heat exchangers (e.g., by adding a term mimicking, by means of a heat transfer coefficient, the coupling with external thermal reservoirs), although have not pursued this possibility.

These models can of course be refined. For example, more complicated end-wall impedances may be accounted for by prescribing, in place of (2.13), (2.14), a relation coupling pressure and velocity at $x = 0, L$. The use of periodicity conditions at the tube ends would permit to model a toroidal travelling wave system, and so on.

2.4 Exchange Terms

The value of the present simplified model consists in its ability to give information on nonlinear, time-domain processes for which no exact theory is available short of direct multi-dimensional numerical simulations. In order to accomplish this goal, it is necessary to develop a suitable time-domain formulation for the cross-axis exchange terms of momentum, $\mathcal{D}(u)$, and energy, $\mathcal{H}(T_w - T)$ and $\mathcal{Q} \partial T_w / \partial x$. For this purpose we turn to the exact frequency-domain theory of the linear regime.

Swift (1988, Eq. A4) gives the following expression for the velocity field in a plane channel of width ℓ :

$$u_1 = \frac{i}{\omega \rho_0} \frac{dp'}{dx} \left(1 - \frac{\cosh(1+i)y/\delta_V}{\cosh(1+i)\ell/2\delta_V} \right), \quad (2.18)$$

where y is measured from the center plane of the channel and the diffusion length δ_V is given by

$$\delta_V = \sqrt{\frac{2\nu}{\omega}}, \quad (2.19)$$

where ν is the kinematic viscosity. From this equation we have

$$\boldsymbol{\tau} \cdot \mathbf{n}_x = -\mu \frac{\partial u_1}{\partial y} \Big|_{y=\ell/2} = -\frac{i(1+i)\mu}{\omega \rho_0 \delta_V} \frac{dp'}{dx} \tanh \frac{(1+i)\ell}{2\delta_V}. \quad (2.20)$$

The mean velocity in the channel (to be identified with our u) is

$$u = \frac{1}{\ell} \int_{-\ell/2}^{\ell/2} u_1 dy = \frac{i}{\omega \rho_0} (1 - f_V) \frac{dp'}{dx}, \quad (2.21)$$

where

$$f_V = \frac{\tanh(1+i)\ell/2\delta_V}{(1+i)\ell/2\delta_V}. \quad (2.22)$$

From these two expressions we find

$$\frac{\mathcal{P}}{S} (\boldsymbol{\tau} \cdot \mathbf{n})_x = -i\omega \rho_0 \frac{f_V}{1 - f_V} u. \quad (2.23)$$

To proceed in the same way in the case of energy exchange, we use the expression for the temperature perturbation in the channel given in Eq. (A10) of Swift (1988):

$$\begin{aligned} T_1 &= \frac{p'}{\rho_0 c_p} \left[1 - \frac{\cosh(1+i)y/\delta_K}{\cosh(1+i)\ell/2\delta_K} \right] \\ &\quad + \frac{1}{\omega^2 \rho_0} \frac{dp'}{dx} \frac{dT_w}{dx} \left[\frac{\sigma}{\sigma - 1} \frac{\cosh(1+i)y/\delta_V}{\cosh(1+i)\ell/2\delta_V} - \frac{1}{\sigma - 1} \frac{\cosh(1+i)y/\delta_K}{\cosh(1+i)\ell/2\delta_K} - 1 \right], \end{aligned} \quad (2.24)$$

where the thermal diffusion length δ_K is defined similarly to δ_V by

$$\delta_K = \sqrt{\frac{2\alpha}{\omega}} = \frac{1}{\sqrt{\sigma}} \delta_V, \quad (2.25)$$

in which α is the thermal diffusivity and σ the Prandtl number. The structure of this result, with dependence on both δ_V and δ_K , shows that the temperature disturbance is determined by both convection and conduction processes. This is the reason for our ansatz (2.9) to express the mean energy transport.

Using (2.24), we can calculate the mean of T_1 over the channel width, to be identified with the temperature disturbance $T - T_w$ of our theory:

$$T - T_w = (1 - f_K) \frac{p'}{\rho_0 c_p} + \frac{1}{\omega^2 \rho_0 (1 - \sigma)} [\sigma(1 - f_V) - (1 - f_K)] \frac{dT_w}{dx} \frac{dp'}{dx}, \quad (2.26)$$

where, as in (2.22),

$$f_K = \frac{\tanh((1+i)\ell/2\delta_K)}{(1+i)\ell/2\delta_K}. \quad (2.27)$$

Again from (2.24), one can calculate the heat flux into the boundaries:

$$-\bar{\mathbf{q}} \cdot \bar{\mathbf{n}} = \frac{k\ell}{\delta_K^2} \left[i f_K \frac{p'}{\rho_0 c_p} + \frac{f_V - f_K}{(1 - f_V)(1 - \sigma)} \frac{\partial T_w}{\partial x} u \right]. \quad (2.28)$$

Upon using (2.21) and (2.26), we then find

$$-\frac{\mathcal{P}}{S} \bar{\mathbf{q}} \cdot \bar{\mathbf{n}} = \frac{i\omega k}{\alpha} \frac{f_K}{1 - f_K} (T - T_w) + \frac{k}{\alpha(1 - \sigma)} \frac{\partial T_w}{\partial x} \left(\sigma - 1 + \frac{1}{1 - f_V} - \frac{\sigma}{1 - f_K} \right) u. \quad (2.29)$$

The functions f_V , f_K defined in (2.22), (2.27) are appropriate for a plane channel geometry. As shown by Rott (1969), for a circular tube with radius r_0 , one has

$$f_V = 2 \frac{J_1((i-1)(r_0/\delta_V))}{(i-1)(r_0/\delta_V) J_0((i-1)(r_0/\delta_V))}, \quad (2.30)$$

with a corresponding expression for f_K .

The expression (2.28) for the heat transfer term may appear somewhat unconventional and it is therefore appropriate to discuss its physical significance. It is easy to show that the coefficient of $T_w - T$ in the first term is just a generalization of the standard heat transfer coefficient. Indeed, if we consider the limit of steady flow, in which $\omega \rightarrow 0$, one readily finds

$$\bar{\mathbf{q}} \cdot \bar{\mathbf{n}} \simeq 8 \frac{k}{\ell} (T_w - T), \quad (2.31)$$

which coincides with the standard result for steady fully developed flow in a channel (see e.g. Incropera and DeWitt 1996, p. 430). The complex, ω -dependent form that appears in (2.28) accounts for the phase relation that is crucial in an oscillatory flow. The same parametrization of this term as for the momentum transfer coefficient is justified by the similarity between the two transfer processes, which is also apparent by the similar functional form of the two terms (cf. Eqns. 2.22 and 2.27).

Of greater interest is the second term in (2.28) which does not arise in conventional heat transfer, in which wall temperature gradients are usually not accounted for explicitly. The physics behind this term may be better understood if it is noted that linearization of the energy equation (2.10), use of the equation of state (2.11), and of the continuity equation (2.6) permit us to write

$$\rho c_p \left[i\omega T' + (1 + \mathcal{Q}) u \frac{dT_w}{dx} \right] - i\omega p' = -\mathcal{H} T', \quad (2.32)$$

where $T' = T - T_w$, $p' = p - P_0$. This relation shows that \mathcal{Q} represents a correction to the convective transport term the origin of which lies in the non-uniformity of the velocity distribution over the channel. Consider the enthalpy convected by the fluid during a time dt across a cross section located at x : the particles very near the wall will carry an enthalpy close to $c_p T_w(x)$, because they will have moved very little due to

the no-slip condition. However, particles further way from the wall will come from further upstream, where the temperature is significantly different from $T_w(x)$. Thus, the enthalpy convected by the average velocity u should not be $c_p T_w(x)$, but should be modified: the factor $1 + Q$ has precisely the role to effect this modification. This analysis is supported by the fact that, in the absence of viscosity ($\sigma = 0$) the velocity distribution is uniform and one finds indeed $Q = 0$ because, then, all the fluid particles transport the same enthalpy.

Returning now to the modelling of the exchange terms \mathcal{D} , \mathcal{H} , and \mathcal{Q} , we note that, upon setting

$$\mathcal{D}(\rho u) = \hat{\mathcal{D}}(\omega) \rho_0 u, \quad \mathcal{H}(T_w - T) = \hat{\mathcal{H}}(\omega) (T_w - T), \quad \mathcal{Q}(\rho u) = \hat{\mathcal{Q}}(\omega) \rho_0 u, \quad (2.33)$$

our formulation will match the exact linear theory expressions (2.23) and (2.29) provided that

$$\hat{\mathcal{D}}(\omega) = i\omega \frac{f_V}{1 - f_V}, \quad (2.34)$$

$$\hat{\mathcal{H}}(\omega) = i\omega \frac{f_K}{1 - f_K}, \quad \hat{\mathcal{Q}}(\omega) = \frac{1}{1 - \sigma} \left(\frac{f_V}{1 - f_V} - \frac{\sigma f_K}{1 - f_K} \right). \quad (2.35)$$

While these definitions reproduce the linear results, they are unsuitable for the present purposes of developing a time-domain formulation. In our earlier work (Yuan et al. 1997), our first attempt was to simply take

$$\mathcal{D}(\rho u) = D \left(1 + \theta_D \frac{\partial}{\partial t} \right) \rho u, \quad (2.36)$$

with D, θ_D constants determined in such a way that

$$D(1 + i\omega_1 \theta_D) = \hat{\mathcal{D}}(\omega_1), \quad (2.37)$$

where ω_1 is the real part of the frequency of the fundamental mode of the system; similar forms were postulated for the other exchange terms. This choice was based on the fact that the fundamental mode at frequency ω_1 is, usually, the most important one and it was therefore felt desirable to simulate it as precisely as possible. This simple choice proved however inadequate as it caused many high-order modes of the system to become unphysically unstable, which caused difficulties in numerical work.

We have therefore decided to improve on this approach by following a suggestion of Achard & Lespinard (1981), who were interested in finding a quasi-one dimensional formulation for the time-dependent viscous flow of a fluid in a duct. While, with the assumption of fully developed flow, the problem is linear and can be solved by Laplace transform methods, they realized that no form for the drag term short of a time convolution can capture exactly the physics of the process. For this reason, they proposed an approximation in which the momentum transfer term was not given by a single constant, but was found by solving an ordinary differential equation in time. The simplest possibility beyond (2.36) is to write

$$a_D \frac{\partial \mathcal{D}}{\partial t} + \mathcal{D} = b_D \left(1 + c_D \frac{\partial}{\partial t} \right) \rho u, \quad (2.38)$$

with a_D, b_D, c_D three suitable real constants. If $a_D = 0$, this relation reduces to the earlier choice (2.36) but, in general, it contains one additional parameter that can be chosen so as to improve the representation of the fluid-solid momentum transfer. We proceed in a similar fashion for the other exchange terms as well:

$$a_H \frac{\partial \mathcal{H}}{\partial t} + \mathcal{H} = b_H \left(1 + c_H \frac{\partial}{\partial t} \right) (T_w - T), \quad (2.39)$$

$$a_Q \frac{\partial \mathcal{Q}u}{\partial t} + \mathcal{Q}u = b_Q \left(1 + c_Q \frac{\partial}{\partial t} \right) \rho u. \quad (2.40)$$

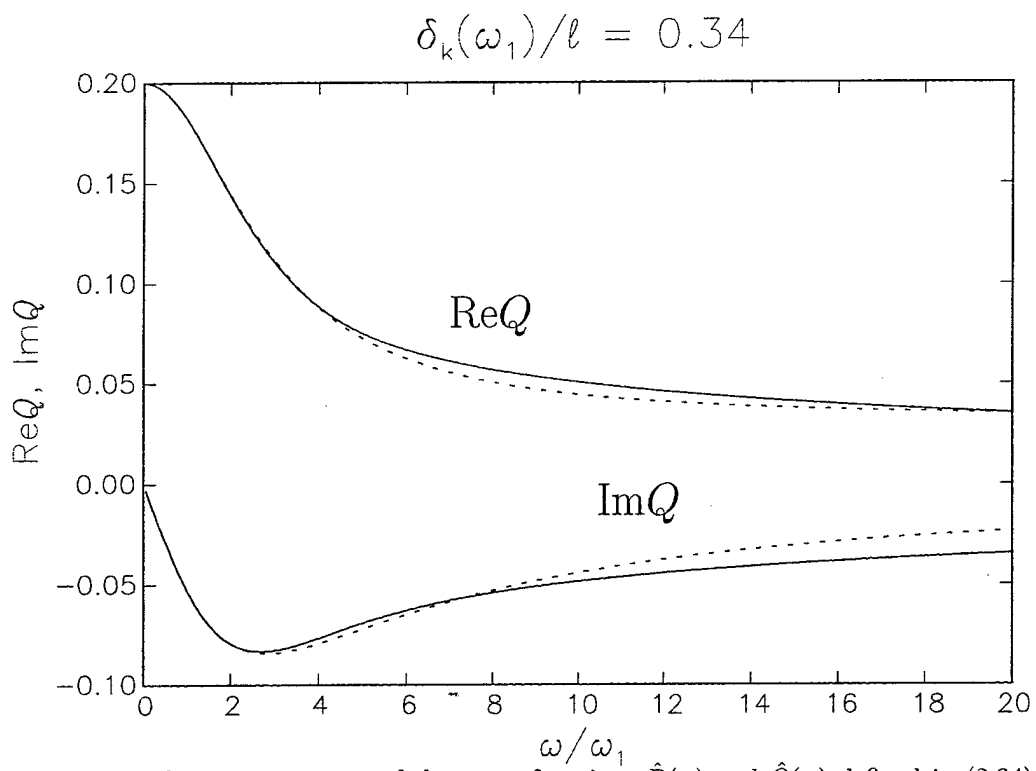
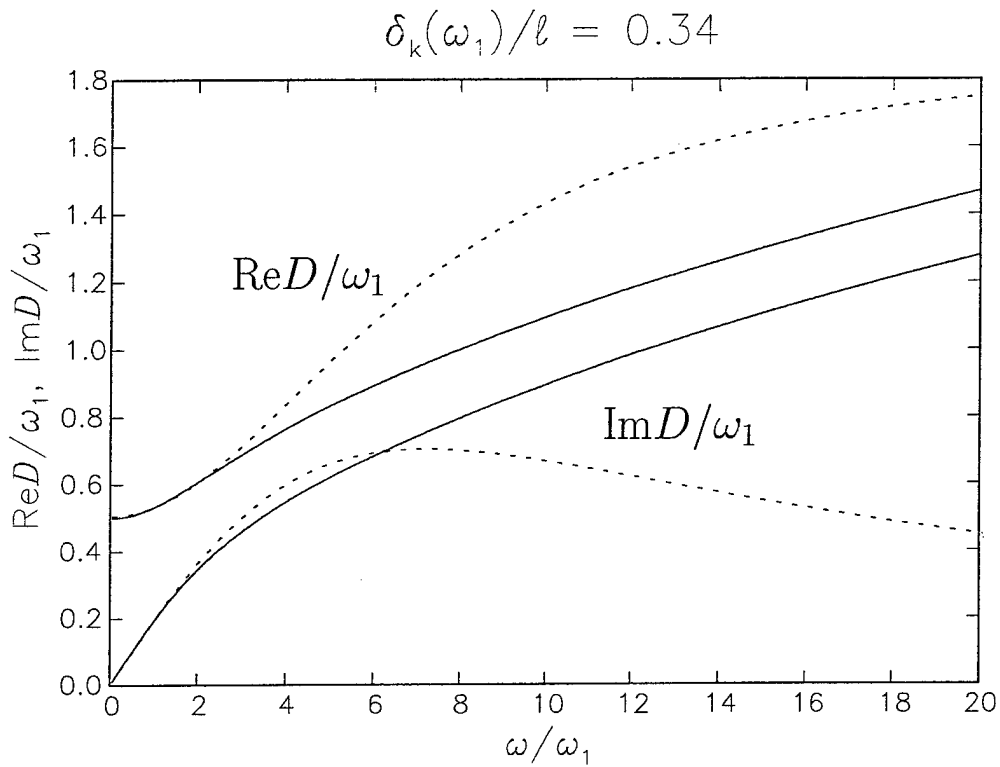


Figure 2.1: Real and imaginary parts of the exact functions $\hat{D}(\omega)$ and $\hat{Q}(\omega)$ defined in (2.34) and (2.35) (solid lines) compared with real and imaginary parts of the approximations for $\tilde{D}(\omega)$ and $\tilde{Q}(\omega)$ of the form (2.41) (dotted lines) for the ratio $\delta_K(\omega_1)/\ell = 0.34$ and Prandtl number $\sigma = 0.71$.

In the frequency domain all these prescriptions reduce to (2.33) with \hat{D} , \hat{H} , \hat{Q} replaced by

$$\tilde{D}(\omega) = b_D \frac{1 + i\omega c_D}{1 + i\omega a_D}, \quad (2.41)$$

etc. We are now at liberty to impose three conditions in order to determine the model parameters a, b, c . As before, in view of the importance of the fundamental mode at frequency ω_1 , we impose that

$$\tilde{D}(\omega_1) = b_D \frac{1 + i\omega_1 c_D}{1 + i\omega_1 a_D} = \hat{D}(\omega_1), \quad (2.42)$$

with $\hat{D}(\omega)$ given by (2.34); here, as before, ω_1 is the real part of the complex eigenfrequency $\hat{\omega}_1$ of the first mode. Upon separating real and imaginary parts, this relation gives two equations.

For the remaining condition there is a considerable latitude. Physically, since the transverse dimensions of the flow passages in the stack are usually much smaller than the stack length, one can make the approximation of fully developed flow in the stack which has the effect of rendering the left-hand side of the exact conservation equations linear. The nonlinear mode-mode coupling is essentially confined to the region outside the stack, and is therefore described by the left-hand sides of the exact conservation equations, which are well approximated by the left-hand sides of (2.6) to (2.10). The process that the exchange terms must model, therefore, is essentially a linear process, which suggests to try to proceed on a mode-by-mode basis. Ideally, therefore, the best approach would be to choose the remaining constant so as to minimize the difference between the exact and approximate linear spectra. This objective can be achieved, but once more at the cost of solving the eigenvalue problem exactly.

Hence, we propose a simpler alternative. In a thermoacoustic prime mover, it is usually the first mode that is unstable. As its amplitude grows, it loses energy to the second and higher modes by non-linear couplings. The second mode is excited the most and, since it is stable, it will represent the greatest energy sink for the system. The situation is similar in a thermoacoustic refrigerator where the forcing typically energizes the fundamental mode the most with, again, the second mode providing the greatest energy loss (after the fundamental). These considerations suggest that an effective second condition for the determination of the last free constant in the exchange terms is to impose that the damping of the second mode be correctly described. We cannot use condition (2.42) for the second mode since the real and imaginary parts of the relation (2.42) give two equations, but only one free constant remains available. To choose the right condition we use as a guide an earlier result (Karpov and Prosperetti 1998 Eqs. 33, 34; Karpov and Prosperetti 2000 Eq. 5.4) according to which the linear growth (or damping) rate of the generic n -th mode can be approximated by

$$\begin{aligned} \text{Im } \hat{\omega}_n &= \frac{1}{2Vp_0^2\omega_n} \int_0^L dx S \left[\frac{c_A^2}{\omega_n} \text{Re} \hat{D}(\omega_n) \left(\frac{dP_n}{dx} \right)^2 \right. \\ &\quad \left. + \gamma \omega_n \text{Re} \hat{H}(\omega_n) P_n (P_n - \mathcal{R} R_n T_w) + (\gamma - 1) \text{Im} \hat{Q}(\omega_n) c_p \frac{dT_w}{dx} P_n \frac{dP_n}{dx} \right]. \end{aligned} \quad (2.43)$$

This result shows that $\text{Im } \hat{\omega}_n$ depends on $\text{Re} \hat{D}(\omega_n)$, $\text{Re} \hat{H}(\omega_n)$, and $\text{Im} \hat{Q}(\omega_n)$, which suggests the following conditions:

$$\text{Re} \hat{D}(\omega_2) = b_D \text{Re} \frac{1 + i\omega_2 c_D}{1 + i\omega_2 a_D}, \quad (2.44)$$

$$\text{Re} \hat{H}(\omega_2) = b_H \text{Re} \frac{1 + i\omega_2 c_H}{1 + i\omega_2 a_H}, \quad \text{Im} \hat{Q}(\omega_2) = b_Q \text{Im} \frac{1 + i\omega_2 c_Q}{1 + i\omega_2 a_Q}. \quad (2.45)$$

Here ω_2 is the real part of the complex eigenfrequency of the second mode $\hat{\omega}_2$.⁵ In order to demonstrate the quality of the approximations thus obtained, in Figs. 2.1 we compare the ω -dependence of the functions \tilde{D}

⁵It is seen from (2.35) that Q is a combination of D and H . However, the presence of the factor $i\omega$ in these two quantities shows that the physical effect accounted for by D and H is in phase with the particle displacement, rather than the velocity, as the effect of Q . For this reason, in the time domain, it is not desirable to derive the expression of Q from those of D and H , but to proceed directly as in (2.35).

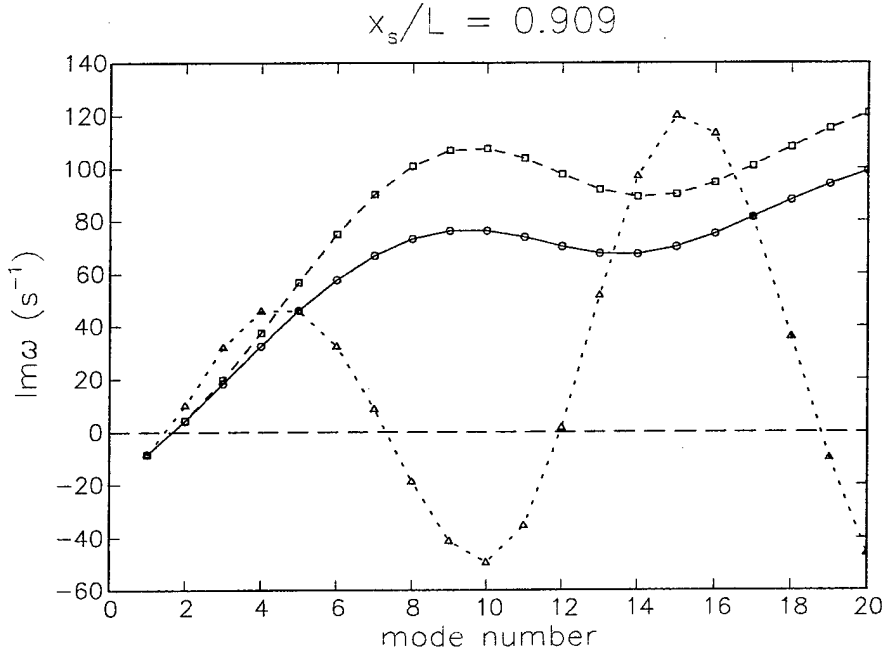


Figure 2.2: Damping constant of the first 20 eigenmodes for the system and conditions described in the text; the stack is located at $x_s/L = 0.909$. The circles are the exact results of the linear theory. The squares and triangles correspond to the differential equation approximation (2.38) to (2.40) to the momentum and energy exchange terms and to the simple explicit form (2.37) respectively. The lines are only meant as guides to the eye.

and \tilde{Q} given by (2.38), (2.40) with the exact expressions \hat{D} , \hat{Q} given in (2.34), (2.35). The Prandtl number is $\sigma = 0.71$ and, at the frequency ω_1 , $\delta_K/\ell = 0.34$. Since the functional dependence of \mathcal{H} on ω is the same as that of \mathcal{D} , we do not show results for this quantity.

In a nonlinear setting, the partial time derivative in (2.38), (2.39), and (2.40) could be replaced by the convective derivative $\partial/\partial t + u\partial/\partial x$. We have taken this approach in Yuan et al. (1997), but found that the difference is minimal, probably because the flow in the most of the stack is essentially fully developed. Hence, we retain the form (2.38), (2.39), and (2.40) in the nonlinear version of the model as well.

As formulated, it would seem that the determination of the model requires the solution of the exact linear eigenvalue problem, at least for the determination of $\hat{\omega}_1$ and $\hat{\omega}_2$. Actually this task can be considerably simplified on the basis of the following observation. In principle, the linear eigenfrequencies of the system are to be found by solving the linearized version of the model, which can be shown to reduce to (Watanabe et al. 1997):

$$\begin{aligned} \frac{1}{S} \frac{d}{dx} \left[\frac{Sc_A^2}{1 + \hat{D}/(i\omega)} \frac{dp}{dx} \right] + \omega^2 p + \frac{\hat{H}}{i\omega} \left\{ \frac{c_A^2}{S} \frac{d}{dx} \left[\frac{S}{1 + \hat{D}/(i\omega)} \frac{dp}{dx} \right] + \gamma \omega^2 p \right\} \\ + \frac{(\gamma - 1)c_p}{1 + \hat{D}/(i\omega)} \frac{dT_w}{dx} \hat{Q} \frac{dp}{dx} = 0, \end{aligned} \quad (2.46)$$

where $c_A^2 = \gamma RT_w$ is the local adiabatic sound speed and proportionality to $\exp(i\omega t)$ has been assumed. It is found numerically that the real part of the eigenfrequencies is very well approximated by neglecting the exchange terms in the eigenvalue equation (2.46) to find

$$\frac{1}{S} \frac{d}{dx} \left(Sc_A^2 \frac{dp'}{dx} \right) + \omega_1^2 p' = 0. \quad (2.47)$$

A further simplification is obtained by using, for c_A , a value based on the average temperature of the resonator:

$$T_e = \frac{1}{L} \int_0^L T_w \, dx. \quad (2.48)$$

In particular, for a cylindrical tube closed at the two ends, one may take

$$\omega_1 \simeq \frac{\pi}{L} \sqrt{\gamma R T_e}, \quad \omega_2 \simeq 2\omega_1. \quad (2.49)$$

Approximations are also available for tubes of non-uniform cross section (see e.g. Rayleigh 1896), although (2.49) may give an adequate approximation in many of these cases as well.

As examples of the effect of the previous approximations on the linear spectrum of the problem, Figs. 2.2, 2.3, and 2.4 show the damping constant of the first 20 eigenmodes as a function of the mode number for three different positions of the stack midpoint, $x_s/L=0.91, 0.77, 0.68$; instability corresponds to a negative value of the quantity shown. The circles connected by the solid line are the exact result of the standard linear theory (2.46). Note that in all the examples only the first mode is unstable. The results shown by the squares and the dashed line correspond to the differential equation formulation (2.38) to (2.40), while the triangles connected by the dotted line correspond to the simple formulation (2.34) and (2.35) for the exchange operators. Although both models give good results for the first few modes, the simple formulation (2.34) to (2.35) makes some higher modes negatively damped, i.e., unstable; this circumstance was at the root of the numerical difficulties encountered in our previous work (Yuan et al. 1997). On the other hand, the differential equation approximation (2.38) to (2.40) gives a good agreement with the exact results for the first few modes and reasonable estimates for the higher modes. Since the fraction of energy contained in these higher modes is usually very small, the associated error is likely to be acceptable.

These numerical results are for a system consisting of a 1 m-long cylindrical tube filled with helium ($\gamma=5/3$, $\sigma=0.71$, $c_p=5.2$ kJ/kg K). The stack has a length of 30 mm and consists of parallel plates of negligible thickness spaced by 0.77 mm. The radius of the tube is assumed to be large so that drag and heat transfer effects are small outside the stack region. The mean pressure is 307 kPa. The tube wall temperature at the left of the stack is $T_C = 293$ K, and at the right $T_H = 415$ K so that $T_H - T_C = 122$ K. In the stack region the wall temperature is independent of time and a linear function of position. Over the temperature range of interest the thermal conductivity data was fitted by a linear function of temperature as $k = 0.151 + 3.228 \times 10^{-4}(T - 300)$, with k in W/m K and T in K. We have included this effect in the calculations as the value of k determines the thermal penetration thickness, and has therefore a significant impact on the heat transfer parameters. The frequencies ω_1 and ω_2 were evaluated using the approximation (2.49).

The present model can accommodate tubes with a non-uniform cross section. To illustrate this effect, we show in Fig. 2.5 results similar to Fig. 2.4 but including the blockage caused by a finite stack plate thickness with $S_{stack}/S_{tube} = 0.75$. As another example, in Figs. 2.6 and 2.7 we consider a tube with a cross-sectional area given by

$$\frac{S(x)}{S(0)} = \begin{cases} 1 & 0 \leq \frac{2}{5}L \\ [1 + Z \cos^2\{5\pi/2(2x/L - 1)\}]^2 & \frac{2}{5}L \leq x \leq \frac{3}{5}L \\ 1 & \frac{3}{5}L \leq x \leq L \end{cases}, \quad (2.50)$$

for Z equal to 0.4 and -0.4 respectively; the stack position is $x_s/L=0.684$ and the thickness of the stack plates is neglected. In all these examples the frequencies ω_1 and ω_2 were evaluated using the simple approximation (2.49), which remains fairly accurate in spite of the cross section variation. For example, for the case of (2.50) with $Z = 0.4$, the error for the fundamental mode is less than 3% and for the second mode about 10%.

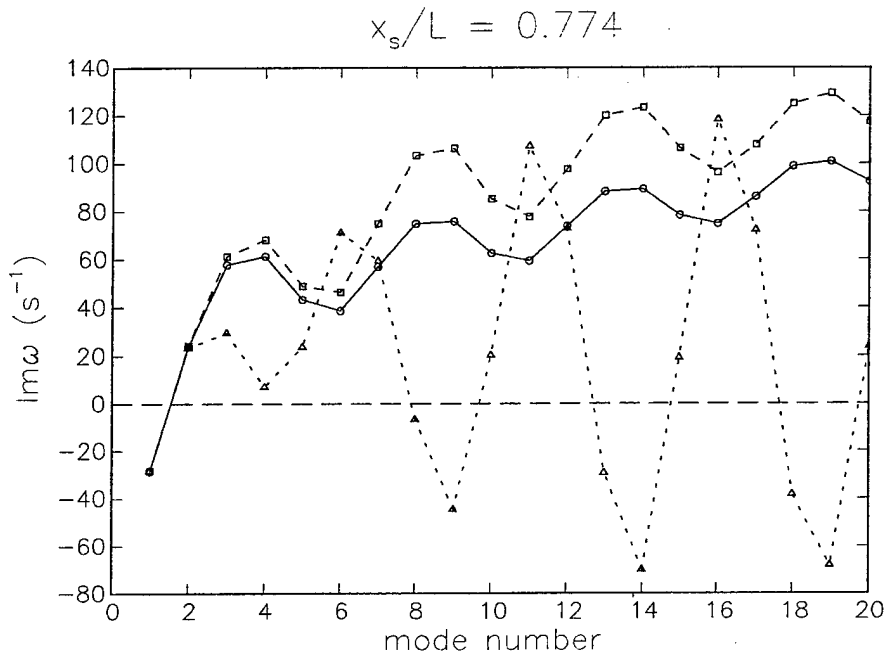


Figure 2.3: Damping constant of the first 20 eigenmodes for the system and conditions described in the text; the stack is located at $x_s/L = 0.774$. The circles are the exact results of the linear theory. The squares and triangles correspond to the differential equation approximation (2.38) to (2.40) to the momentum and energy exchange terms and to the simple explicit form (2.37) respectively. The lines are only meant as guides to the eye.

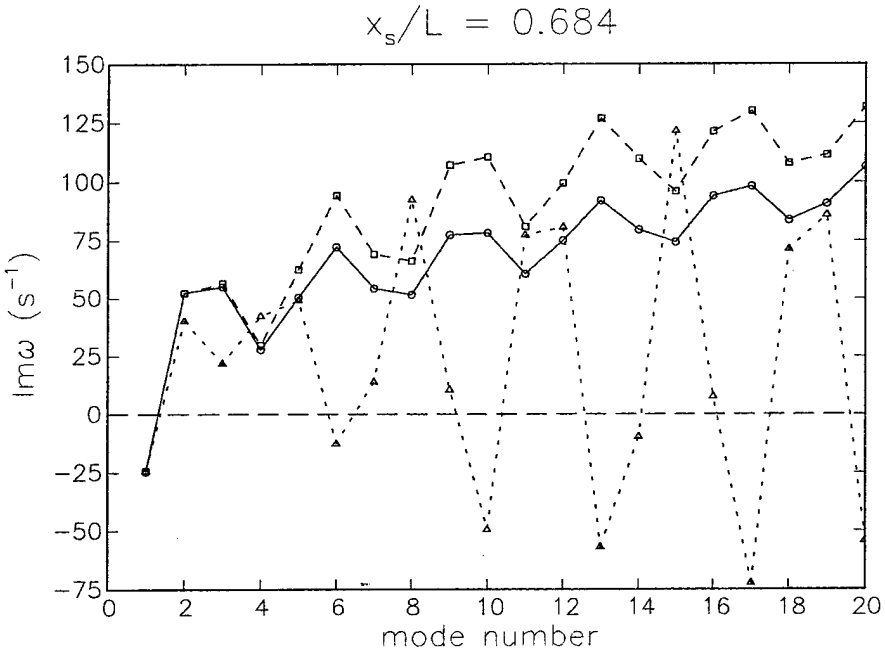


Figure 2.4: Damping constant of the first 20 eigenmodes for the system and conditions described in the text; the stack is located at $x_s/L = 0.684$. The circles are the exact results of the linear theory. The squares and triangles correspond to the differential equation approximation (2.38) to (2.40) to the momentum and energy exchange terms and to the simple explicit form (2.37) respectively. The lines are only meant as guides to the eye.

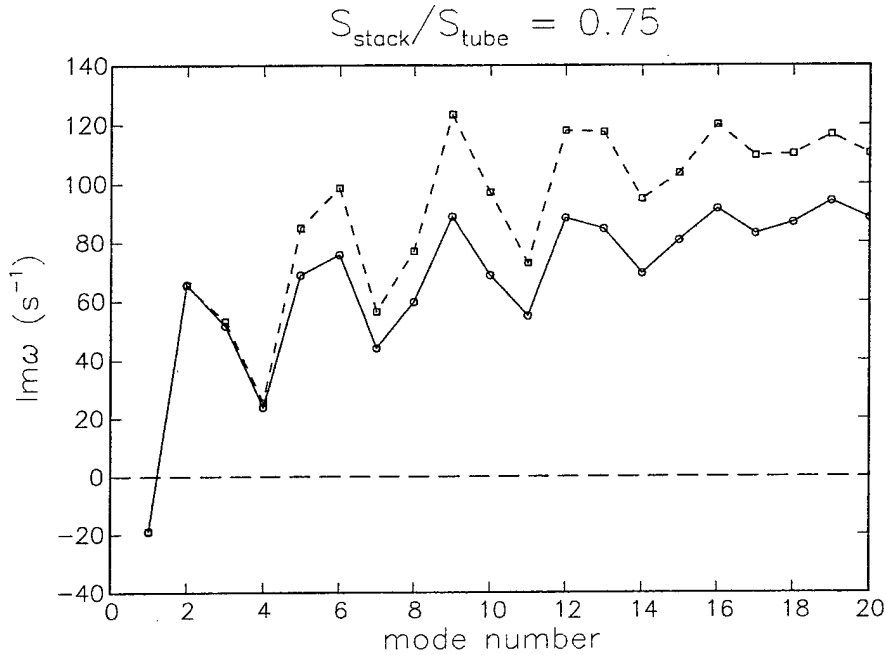


Figure 2.5: Damping constant of the first 20 eigenmodes for the same case as in the previous figure, but including the 25% blockage (75% porosity) of finite-thickness plates.

2.5 Numerical Method

With the expressions (2.36), (2.39), and (2.40), and the definitions

$$m = \rho u, \quad e = \frac{1}{\gamma - 1} p + \frac{1}{2} \rho u^2, \quad (2.51)$$

for the momentum flux m and total energy e , it is easy to verify that the continuity, momentum, and energy equations (2.6), (2.7), and (2.10) may equivalently be written as

$$\frac{\partial \rho}{\partial t} + \frac{\partial m}{\partial x} + \frac{m}{S} \frac{\partial S}{\partial x} = 0, \quad (2.52)$$

$$\frac{\partial m}{\partial t} + \frac{\partial}{\partial x} (mu + p) + \frac{mu}{S} \frac{\partial S}{\partial x} = 0 = -\mathcal{D}(m), \quad (2.53)$$

$$\frac{\partial e}{\partial t} + \frac{\partial}{\partial x} [u(e + p)] + \frac{u}{S} (e + p) \frac{\partial S}{\partial x} = \rho c_p \mathcal{H}(T_w - T) - c_p \frac{\partial T_w}{\partial x} \mathcal{Q}(m). \quad (2.54)$$

We rewrite this system of equations in vector form as

$$\frac{\partial \mathbf{w}}{\partial t} + \frac{\partial \mathbf{F}}{\partial x} + \mathbf{s} = \mathbf{b}, \quad (2.55)$$

where \mathbf{w} and the flux vector \mathbf{F} are given by

$$\mathbf{w} = \begin{vmatrix} \rho \\ m \\ e \end{vmatrix}, \quad \mathbf{F} = \begin{vmatrix} m \\ mu + p \\ (e + p)u \end{vmatrix}, \quad (2.56)$$

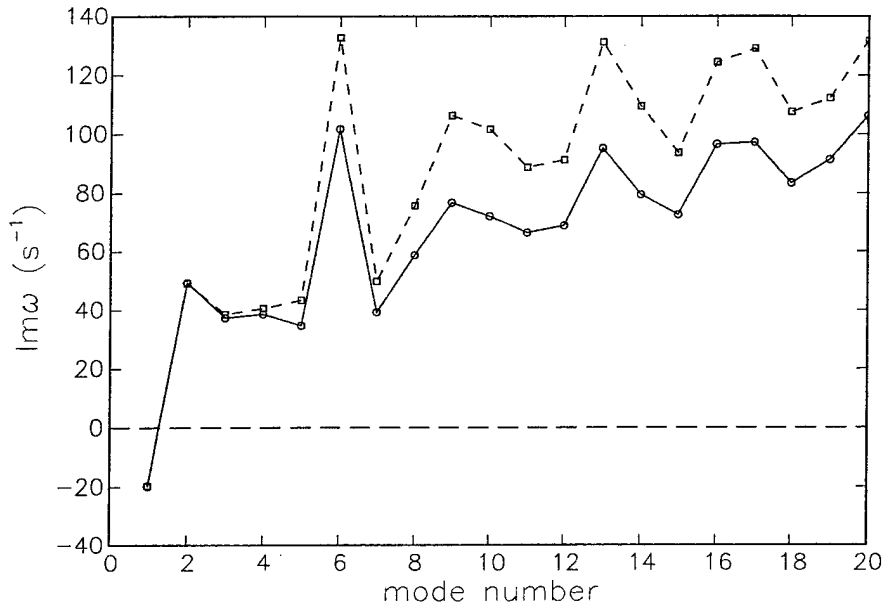


Figure 2.6: Damping constant of the first 20 eigenmodes for a resonator with a wider midsection according to (2.50) with $Z = 0.4$; see text for a description of the system modelled. The stack is located at $x_s/L = 0.684$ as in the previous two figures. The circles are the exact results of the linear theory. The squares and triangles correspond to the differential equation approximation (2.38) to (2.40) to the momentum and energy exchange terms and to the simple explicit form (2.37) respectively. The lines are only meant as guides to the eye.

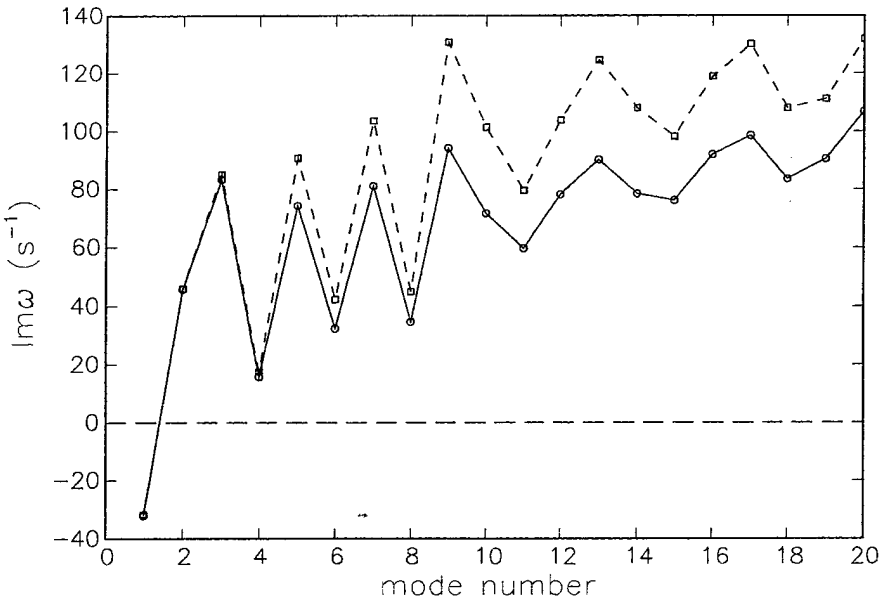


Figure 2.7: As in the preceding figure, but with $Z = -0.4$.

while the vector \mathbf{s} accounting for the effect of changes in the cross-sectional area and the forcing \mathbf{b} are given by

$$\mathbf{s} = \begin{vmatrix} m \\ mu \\ (e+p)u \end{vmatrix}, \quad \mathbf{b} = \begin{vmatrix} 0 \\ -\mathcal{D}(m) \\ \rho c_p \mathcal{H}(T_w - T) - c_p (\partial T_w / \partial x) \mathcal{Q}(m) \end{vmatrix}. \quad (2.57)$$

Our first attempt at solving Eq. (2.55) was based on a straightforward centered-difference spatial discretization with a predictor-corrector time stepping procedure (Prosperetti & Watanabe 1994). We found that, whenever conditions were such that quasi-shocks developed, a series of spurious grid-dependent oscillations also appeared. Such oscillations are a well-known numerical artifact affecting computations in the presence of steep gradients (see e.g. Roe 1986; Fletcher 1988), and their elimination has motivated a large amount of research. While a complete bibliography would be out of place here, it may be useful to cite the review by Roe (1986) and a few other papers (Sod 1978; Harten 1983; Osher 1984; Osher and Chakravarthy 1984; Sweby 1984; Harten et al. 1986; Harten and Osher 1987). This effort has led to a new family of schemes for hyperbolic equations known as Total Variation Diminishing (TVD) schemes. The name is a consequence of the definition of the *total variation* $\text{TV}(u^n)$ of a grid function $\{u_i^n\}$, $i = 1, 2, \dots, N+1$ at time t^n :

$$\text{TV}(u^n) = \sum_{i=1}^N |u_{i+1}^n - u_i^n|, \quad (2.58)$$

and of the fact that these schemes have the property that $\text{TV}(u^n)$ is a non-increasing function of time:

$$\text{TV}(u^n) = \text{TV}(u^{n+1}). \quad (2.59)$$

Evidently, a TVD scheme cannot produce an oscillatory solution starting from monotonic initial data. We have found that the scheme proposed by Harten (1983) proved suitable for our problem.

The system (2.55) is first discretized explicitly in time as

$$\frac{\mathbf{w}_i^{n+1} - \mathbf{w}_i^n}{\Delta t} + \frac{\hat{\mathbf{F}}_{i+1/2}^n - \hat{\mathbf{F}}_{i-1/2}^n}{\Delta x} + \mathbf{s}_i^n = \mathbf{b}_i^n, \quad (2.60)$$

where superscripts indicate time levels and subscripts spatial nodes. The essential aspect of the method is the manner in which the modified fluxes $\hat{\mathbf{F}}$ are specified in terms of the auxiliary quantities

$$\mathbf{R}^{(1)} = \begin{vmatrix} 1 \\ u - c \\ (e+p)/\rho - uc \end{vmatrix}, \quad \mathbf{R}^{(2)} = \begin{vmatrix} 1 \\ u \\ \frac{1}{2}u^2 \end{vmatrix}, \quad \mathbf{R}^{(3)} = \begin{vmatrix} 1 \\ u + c \\ (e+p)/\rho + uc \end{vmatrix}. \quad (2.61)$$

where $c = \sqrt{\gamma RT}$, and

$$a^{(1)} = u - c, \quad a^{(2)} = u, \quad a^{(3)} = u + c. \quad (2.62)$$

Let

$$2c_{i+1/2}^2 \alpha_{i+1/2}^{(1)} = p_{i+1} - p_i - \rho_{i+1/2} c_{i+1/2} (u_{i+1} - u_i) + \frac{\rho_{i+1/2} c_{i+1/2}^2 u_{i+1/2}}{u_{i+1/2} - c_{i+1/2}} \frac{S_{i+1} - S_i}{S_{i+1/2}}, \quad (2.63)$$

$$c_{i+1/2}^2 \alpha_{i+1/2}^{(2)} = c_{i+1/2}^2 (\rho_{i+1} - \rho_i) - (p_{i+1} - p_i), \quad (2.64)$$

$$2c_{i+1/2}^2 \alpha_i^{(3)} = p_{i+1} - p_i + \rho_{i+1/2} c_{i+1/2} (u_{i+1} - u_i) + \frac{\rho_{i+1/2} u_{i+1/2} c_{i+1/2}^2}{u_{i+1/2} + c_{i+1/2}} \frac{S_{i+1} - S_i}{S_{i+1/2}}, \quad (2.65)$$

where the quantities carrying a half-integer subscript are calculated as arithmetic averages, e.g. $\bar{u} = \frac{1}{2}(u_{i+1} + u_i)$. Then

$$\hat{\mathbf{F}}_{i+1/2} = \frac{1}{2}(\mathbf{F}_{i+1} + \mathbf{F}_i) + \frac{\Delta t}{2\Delta x} \sum_{\ell=1}^3 \left[g_i^{(\ell)} + g_{i+1}^{(\ell)} - Q(\nu_{i+1/2}^{(\ell)} + \gamma_i^{(\ell)}) \alpha_i^{(\ell)} \right] \mathbf{R}_{i+1/2}^{(\ell)}, \quad (2.66)$$

where

$$\nu^{(\ell)} = \frac{\Delta t}{\Delta x} a^{(\ell)}, \quad \gamma_i^{(\ell)} = \frac{g_{i+1}^{(\ell)} - g_i^{(\ell)}}{\alpha_i^{(\ell)}}. \quad (2.67)$$

The quantities $g_i^{(\ell)}$ appearing in these definitions are a correction to the components of the flux \mathbf{F} along the characteristic directions and are the smaller one in modulus between

$$\left[Q(\nu_{i+1/2}^{(\ell)}) - \nu_{i+1/2}^{(\ell)} \right] \alpha_{i+1/2}^{(\ell)}, \quad \text{and} \quad \left[Q(\nu_{i-1/2}^{(\ell)}) - \nu_{i-1/2}^{(\ell)} \right] \alpha_{i-1/2}^{(\ell)}. \quad (2.68)$$

This flux correction is introduced to account for the discretization error and guarantees second-order accuracy in space.

The last quantity to be defined is the function $Q(x)$ that may be considered as a modified $|x|$. Specifically, following Harten (1983), we take

$$Q(x) = \begin{cases} x^2/(4\epsilon) + \epsilon & \text{for } |x| < 2\epsilon \\ |x| & \text{for } |x| \geq 2\epsilon \end{cases}, \quad (2.69)$$

with $\epsilon = 0.1$. This quantity plays the role of an artificial viscosity.

The other terms in (2.60) are treated in a more conventional way. The components of \mathbf{b} are written as

$$b_i^{n+1}(2) = -\frac{a_D}{\Delta t + a_D} \mathcal{D}_i^n - \frac{b_D}{1 + a_D/\Delta t} \left(m^{n+1} + c_D \frac{m^{n+1} - m^n}{\Delta t} \right)_i \quad (2.70)$$

$$\begin{aligned} b_i^{n+1}(3) = & \frac{a_H}{\Delta t + a_H} c_p \rho_i^n \mathcal{H}_i^n + \frac{c_p \rho_i^n b_H}{1 + a_H/\Delta t} \left(T_w^n - T^n + c_H \frac{T_w^n - T_w^{n-1}}{\Delta t} \right)_i \\ & - \frac{\gamma b_H c_H}{\Delta t + a_H} \left[e^{n+1} - e^n - u^n(m^{n+1} - m^n) + \left(\frac{1}{2}(u^n)^2 - \frac{c_p}{\gamma} T^n \right) (\rho^{n+1} - \rho^n) \right]_i \\ & - \frac{a_Q}{\Delta t + a_Q} \mathcal{Q}^n - \frac{c_p b_Q}{1 + a_Q/\Delta t} \frac{T_{w,i+1}^n - T_{w,i-1}^n}{2\Delta x} \left(m^{n+1} + c_Q \frac{m^{n+1} - m^n}{\Delta t} \right)_i \end{aligned} \quad (2.71)$$

The spatial derivatives appearing \mathbf{s} are discretized by central differences.

After the quantities ρ, m , and e at time step $(n+1)$ are calculated, the gas temperature is obtained from the equation of state (2.11) and the wall temperature T_w^{n+1} is found from a discretization of the heat conduction equation (2.12):

$$\begin{aligned} \frac{T_{w,i}^{n+1} - T_{w,i}^n}{\Delta t} = & \frac{k_s}{\rho_s c_s} \frac{T_{w,i+1}^n - 2T_{w,i}^n + T_{w,i-1}^n}{\Delta x^2} \\ & - c_p \rho_s c_s S_{s,i} \left[\rho_i^n \mathcal{H}(T_w^n - T^n)_i - \frac{T_{w,i+1}^n - T_{w,i-1}^n}{2\Delta x} \mathcal{Q}(m_i^n) \right]. \end{aligned} \quad (2.72)$$

The last step is to update the exchange terms:

$$\mathcal{D}_i^{n+1} = \frac{a_D}{\Delta t + a_D} \mathcal{D}_i^n + \frac{b_D}{1 + a_D/\Delta t} \left(m^{n+1} + c_D \frac{m^{n+1} - m^n}{\Delta t} \right)_i, \quad (2.73)$$

$$\mathcal{H}_i^{n+1} = \frac{a_H}{\Delta t + a_H} \mathcal{H}_i^n + \frac{c_p \rho_i^{n+1} b_H}{1 + a_H/\Delta t} \left(T_w^{n+1} - T^{n+1} + c_H \frac{T_w^{n+1} - T_w^n - (T^{n+1} - T^n)}{\Delta t} \right)_i , \quad (2.74)$$

$$\mathcal{Q}_i^{n+1} = \frac{a_Q}{\Delta t + a_Q} \mathcal{Q}_i^n + \frac{b_Q}{1 + a_Q/\Delta t} \frac{T_{w,i+1}^{n+1} - T_{w,i-1}^{n+1}}{\Delta x} \left(m^{n+1} + c_Q \frac{m^{n+1} - m^n}{\Delta t} \right)_i . \quad (2.75)$$

The values of viscosity and thermal diffusivity are evaluated at the local instantaneous prevailing conditions.

Since the integration is explicit in time, the preceding formulae are sufficient to construct the solution at all the interior nodes at time level t^{n+1} starting from the known values at t^n . The solution at the two boundary nodes is calculated from the boundary conditions appropriate for each particular problem.

The time step Δt is adjusted so that the maximum Courant number $\Delta t |a^{(l)}| / \Delta x$ (with the $a^{(l)}$'s defined in 2.62) remains below 0.4.

It is well known (see e.g. Cao et al. 1996; Worlikar & Knio 1999) that sharp temperature gradients exist near the ends of the stack, while the fields are smooth away from the stack region. For this reason, the use of a variable spatial node spacing improves efficiency.

2.6 Results

In order to illustrate the behavior of the model described before we now consider several examples: a prime mover with a temperature gradient above onset, an externally driven thermoacoustic refrigerator, and a prime mover/refrigerator combination.

2.6.1 A Prime Mover

The first example is a model of the prime mover system studied by Atchley et al. (1990b) and Atchley (1992, 1994). It consists of a 38.2 mm-diameter tube with a length of 99.89 cm, a stack of 35 stainless steel plates located 90.13 cm from the cold end, and two heat exchangers. The plates are 35 mm-long, with a thickness of 0.28 mm and a spacing of 0.77 mm. We take handbook values for the physical properties: $\rho_s = 7,900 \text{ kg/m}^3$, $c_s = 480 \text{ J/(kg K)}$, $k_s = 14.9 \text{ W/(m K)}$. The cold heat exchanger at the left end of the stack consists of two identical structures separated by 1.5 mm, each with 25 nickel plates 0.45 mm thick, spaced by 1.04 mm and 10.2 mm long. The hot heat exchanger is attached to the right of the stack and is built as the cold one except that it consists of only one 7.62 mm-long structure. The area blockage is about 30% (70% porosity) in the heat exchangers and 27% (73% porosity) in the stack.

A feature to be noted in this system is the difference between the number of stack and heat exchanger plates. For the conditions of the experiment the thermal penetration length at the temperature of the cold heat exchanger is approximately 0.19 mm, which is about 25% of the stack plate spacing but only 18% of the heat exchanger plate spacing. At the hot heat exchanger temperature, $\delta_K \simeq 0.38 \text{ mm}$ and the corresponding ratios are 49% and 37%. Since a gas particle only exchanges heat if it is within 1-2 thermal penetration lengths from the plates, as sketched in Fig. 2.8 it may be expected that some of the stack plates are effectively not contributing as the gas particles that move along them make only an imperfect thermal contact with the heat exchangers, particularly at the cold end where δ_K is smaller.

To account in a rough way for this effect one may say that only as many stack plates as there are heat exchanger plates take part in the heat transfer. Alternatively, the effect of each stack flow passage, as represented by the heat exchange terms \mathcal{H} and \mathcal{Q} , should be reduced by a factor $K_h = 25/35 \simeq 0.71$.

In order to show that this is a reasonable estimate we first consider the linear case. With the correction factor K_h , upon linearization and in the frequency domain, in place of (2.46) the system (2.6) to (2.10) leads to the following eigenvalue equation for the pressure perturbation p' :

$$\frac{1}{S} \frac{d}{dx} \left[\frac{Sc_A^2}{1 + \hat{D}(\omega)/(i\omega)} \frac{dp'}{dx} \right] + K_h \frac{\hat{H}(\omega)}{i\omega} \frac{c_A^2}{S} \frac{d}{dx} \left[\frac{S}{1 + \hat{D}(\omega)/(i\omega)} \frac{dp'}{dx} \right]$$

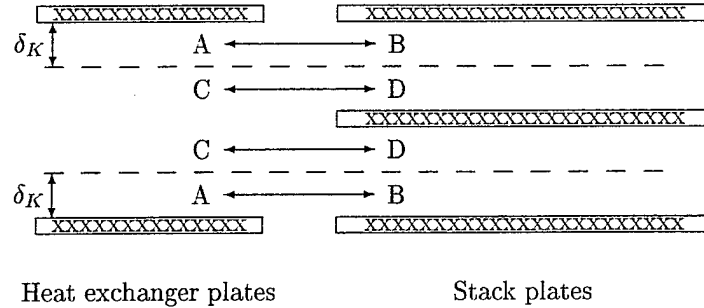


Figure 2.8: Schematic representation of a case in which the gap between stack plates is half that between heat exchanger plates. The gas particles moving between points A and B exchange heat with the heat exchanger plates since the point A is within a thermal penetration depth δ_K . In contrast, the gas particles moving between points C and D do not exchange heat with the heat exchanger plates. Therefore, the middle stack plate does not participate in the heat transport along the stack.

$$+ \left(1 + K_h \gamma \frac{\hat{H}(\omega)}{i\omega} \right) \omega^2 p' + K_h \hat{Q}(\omega) \frac{(\gamma - 1)c_p}{1 + \hat{D}(\omega)/(i\omega)} \frac{dT_w}{dx} \frac{dp'}{dx} = 0, \quad (2.76)$$

where, as before, c_A is the local adiabatic sound speed and $\hat{D}(\omega)$, $\hat{H}(\omega)$, and $\hat{Q}(\omega)$ are defined in (2.34) and (2.35).

In the experiments of Atchley et al. (1990b) the temperature difference of 325 K was slightly above onset. A solution of equation (2.76) gives an onset temperature difference of 279.6 K for $K_h = 1$ and 319.1 K for $K_h = 0.71$. From the data reported in Atchley 1994, difference along the stack of 379 K, the linear temporal growth rate of the perturbation is 5.0 s^{-1} . The solution of Eq. (2.76) gives a linear growth rate of 11.87 s^{-1} for $K_h = 1$ and 5.64 for $K_h = 0.71$. Obviously the correction embodied in K_h gives a much better agreement of the linear theory with the experimental results and, for this reason, we feel justified in using the same correction factor K_h for the nonlinear problem as well.

Figures 2.9 and 2.10 show the transient and steady-state temporal waveforms of the pressure at the cold end of the tube for the case with a temperature difference $T_H - T_C = 368$ K described by Atchley et al. (1990b). The calculation is started with a linear temperature distribution in the stack and a small amplitude of the first system normal mode. The helium mean pressure is 307 kPa. Figure 2.11 shows the temperature deviation from the initial value as a function of time at the center of the stack and 1 mm away from its cold and hot ends. The temperature near the cold end increases and that near the hot end decreases rapidly during the first second, after which they slowly reach the steady state values. The difference between the initial and steady state temperatures is approximately 5 K and 6 K for the cold and hot ends of the stack, respectively. In contrast, the temperature in the middle of the stack decreases slowly to its steady state value (not yet achieved in this figure). The final stack temperature distribution averaged over one cycle is shown in Fig. 2.12. The solid line is the mean wall temperature and the dotted line the mean gas temperature. One can see that there are near-jumps in the temperature of the solid structure at the ends of the stack. The correctness (at least qualitative) of this result is confirmed by the experiments and analysis of Brewster et al. 1997 and the calculations of Worlikar (1997) and Worlikar et al. (1998). These near-jumps effectively reduce the available temperature difference in the stack thus reducing the steady state oscillation amplitude in comparison with what would be obtained by assuming a time-independent linear stack temperature distribution equal to $T_H - T_C$. This effect is shown in Fig. 2.10 by the dotted line which represents the results with the assumption that the wall temperature in the stack region is a time-independent linear function of position. For this particular case the difference between the two results is however small.

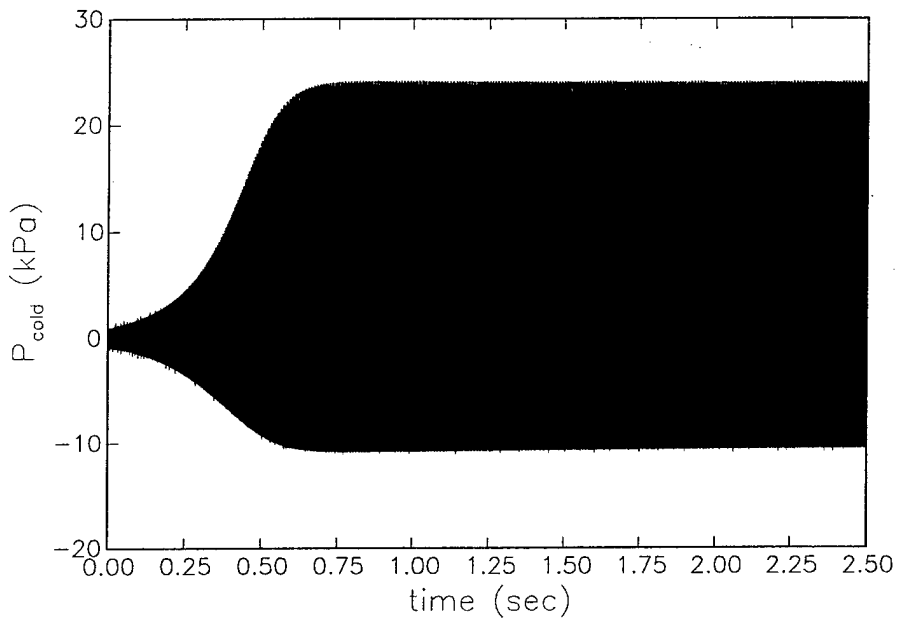


Figure 2.9: Transient behavior of the pressure at the cold end of the tube for a prime mover with a temperature difference $T_H - T_C = 368$ K described by Atchley et al. (1990b).

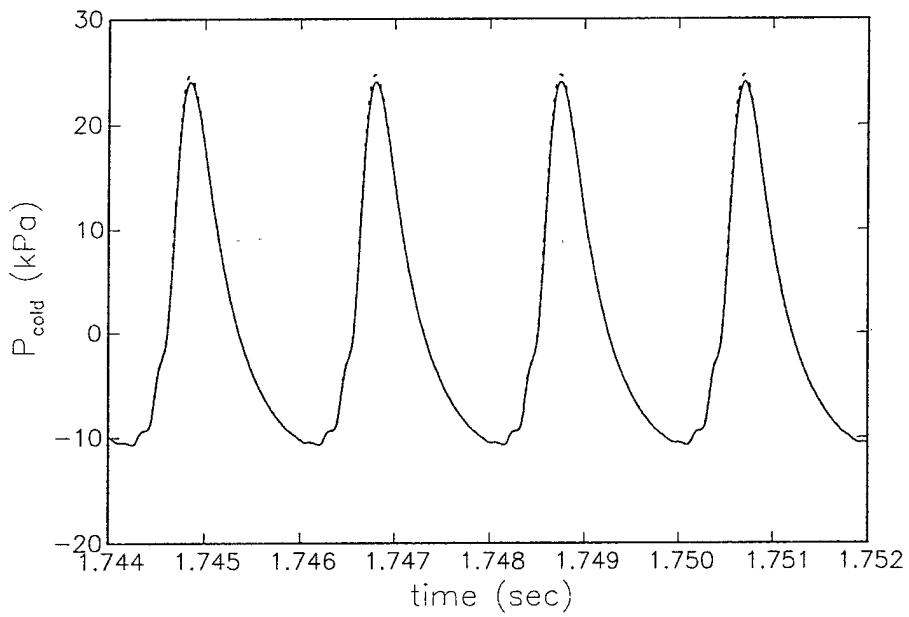


Figure 2.10: Steady-state temporal waveform of the pressure at the cold end of the tube for the prime mover of the previous figure. The dotted line corresponds to a fixed linear temperature distribution in the stack; the solid line is calculated with the numerically determined steady-state temperature distribution at the end of the transient.

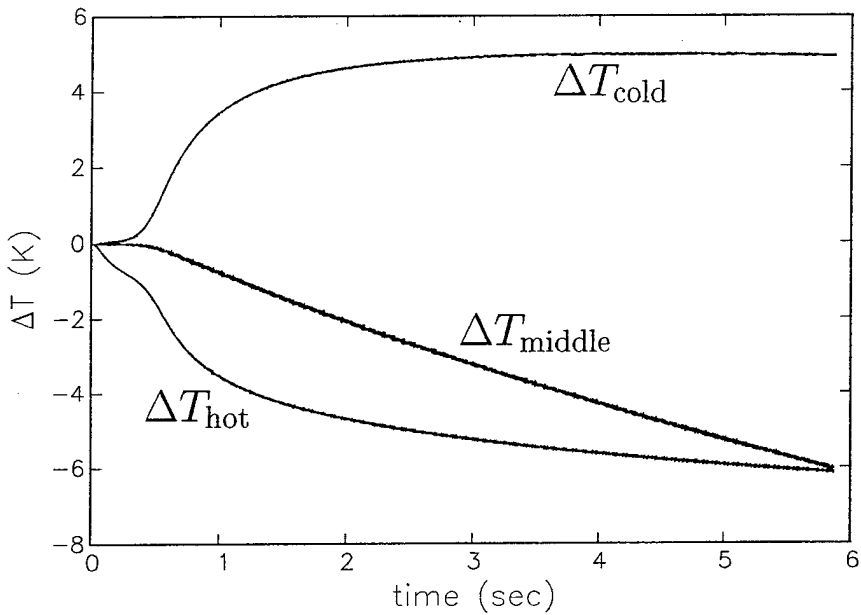


Figure 2.11: Temperature deviation from the initial value as a function of time at the center of the stack and 1 mm away from the cold and hot ends for the prime mover of the previous two figures. Initially the temperature near the cold end increases and that near the hot end decreases very rapidly. The difference between the initial and steady state temperature is approximately 5 K and 6 K for the cold and hot ends of the stack, respectively. In contrast, the temperature in the middle of the stack decreases slowly to its steady state value (not shown in this figure). The final stack temperature distribution is shown in the next figure.

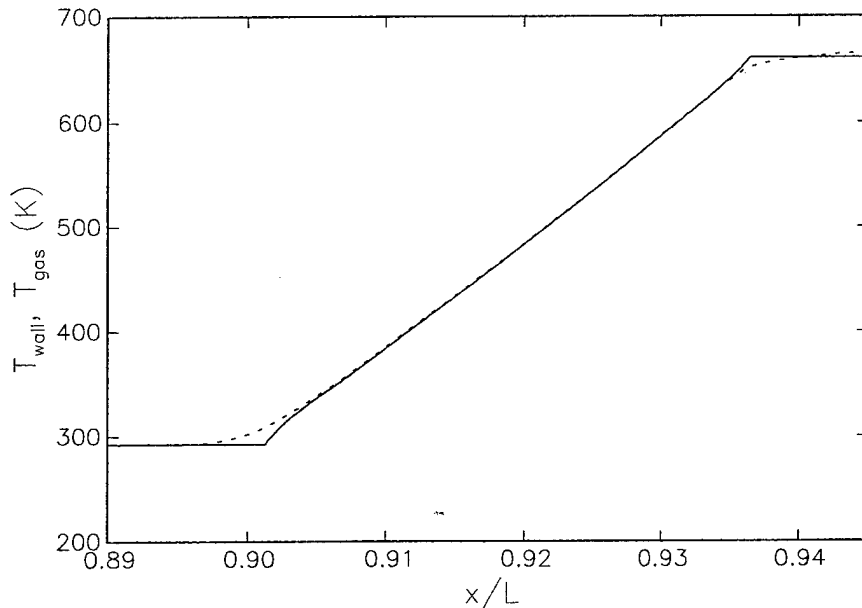


Figure 2.12: The final mean temperature distribution in the stack (solid line) and in the gas (dotted line) for the prime mover of the previous three figures. Note the jumps in the solid structure temperature at the ends of the stack.

Figure 2.10 should be compared with Fig. 4 of Atchley et al. (1990b). Qualitatively, the numerical results are close to the experimental ones. The period, 1.95 ms, is identical within the precision with which it can be read from the figure. The waveform exhibits a strong asymmetry, with the negative amplitude much smaller than the positive one. The major difference between calculations and experiment is the amplitude, which is about 24.0 kPa in Fig. 2.10, but 13.5 kPa in the data. In order to match to measured wave amplitude the temperature difference $T_H - T_C$ should be decreased by about 25 K. A possible explanation for this difference may be the following. First of all, the temperature values reported in Atchley et al. were measured at the surface of the tube, rather than in the middle of the heat exchanger plates. For the conditions of the experiment it is not unreasonable to expect a temperature difference of the order of 10-20 K between these two points. In addition, the experimental setup most likely includes several loss mechanisms (e.g. form drag of the plates, acoustic streaming, natural convection) not included in our model.

2.6.2 Piston-Driven Refrigerator

Now we consider a simple model of a thermoacoustic refrigerator in which a piston at the left end of the tube sets up a standing wave; the right end is modelled as rigid.

The driving frequency is equal to the natural frequency of the tube open at one end, namely $\omega = 2\pi\sqrt{\gamma RT_i}/(4L)$, where $L = 0.5$ m is the tube length and $T_i = 293$ K the initial uniform temperature of the gas and solid structures. An oscillating velocity $u(t) = U_A \sin \omega t$ is prescribed at $x = 0$ and $p' = \rho' = T' = 0$ there as discussed at the end of section 2.2. The gas is helium at a mean pressure $P_0 = 307$ kPa. The stack consists of 0.28 mm-thick, 30 mm-long plates spaced by 0.77 mm with a thermal conductivity of $k_s = 0.48$ W/(K m) characteristic of fiberglass. It is well known from linear theory (see e.g. Swift 1988; Karpov and Prosperetti 1998) that the thermoacoustic heat flux is strongest when the stack is positioned midway between a velocity node and antinode. Since in this case the tube length is one quarter of the acoustic wavelength, we position the stack at $x_s/L = 0.5$.

The hot heat exchanger is modelled by assuming a spatially and temporally constant temperature. The cold heat exchanger is assumed to be unloaded and to only exchange heat with the gas and the stack. It is therefore modelled assuming a spatially uniform, time-dependent temperature the mean value of which will decrease with time under the action of the sound waves. Since the thermal conductivity is assumed to be very large, this cold heat exchanger is simply characterized by the product $\rho_s c_s$. The duration of the transient of the system increases with the value of this quantity and therefore, in order to limit the computational time, we choose $\rho_s c_s = 480$ kW/(K m³) which is about one order of magnitude smaller than the appropriate value for realistic materials. In spite of this limitation, the results that follow are useful to demonstrate the performance of the model. For simplicity, we disregard blockage effects and take both f_V and f_K to vanish outside the stack and heat exchanger region thus neglecting momentum and energy exchange with the resonator tube walls.

Figure 2.13 shows the temperature T_w as a function of time at the cold heat exchanger (lowest line), at the stack midpoint (middle line), and 1 mm away from the end of the hot heat exchanger. Here the imposed velocity amplitude U_A is 24.2 m/s which, when converted to pressure according to the standard acoustic relation $U_A = P_A/\rho c_A$, corresponds to a drive ratio $P_A/P_0 = 0.04$. The temperature of the cold heat exchanger initially decreases with time and finally stabilizes at about 18.5 K less than the initial temperature. At steady state, on average, the heat extracted from the heat exchanger by the gas must exactly balance the heat gained by conduction from the stack plates. Thus, the acoustic power supplied to the system by the piston is spent only to maintain this steady state by removing during each cycle the same amount of heat from the cold heat exchanger that it receives from the stack by conduction. Figure 2.14 shows the final mean temperature distribution in the region of the stack and the heat exchangers. The mean temperature of the solids is shown by the solid line, and that of the gas by the dotted line. There are near-jumps in the temperature of the solid structure at the ends of the stack similar to those found in Fig. 2.12. Note that a significant difference between the gas and solid structure temperatures occurs only in the heat exchanger regions, whereas the temperature of the gas and the plates is almost the same over most of the stack. The mean temperature of the gas is higher than that of the solid structure over one part of the heat exchanger

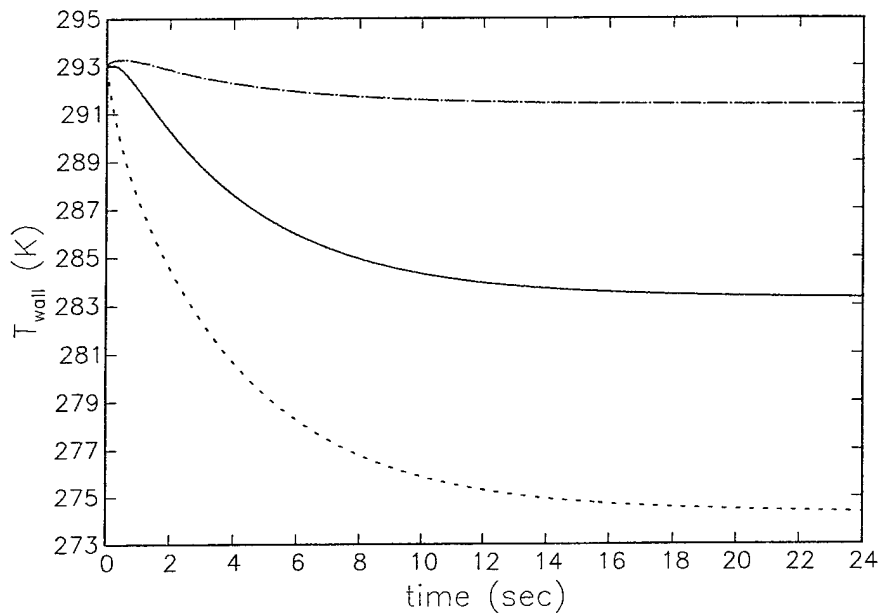


Figure 2.13: Mean wall temperature as a function of time at the cold heat exchanger (dotted line), at the stack midpoint (solid line), and 1 mm away from the hot heat exchanger (dot-dash line) for a driven tube with a drive ratio of 4%. The final temperature difference between the heat exchangers is 18.5 K.

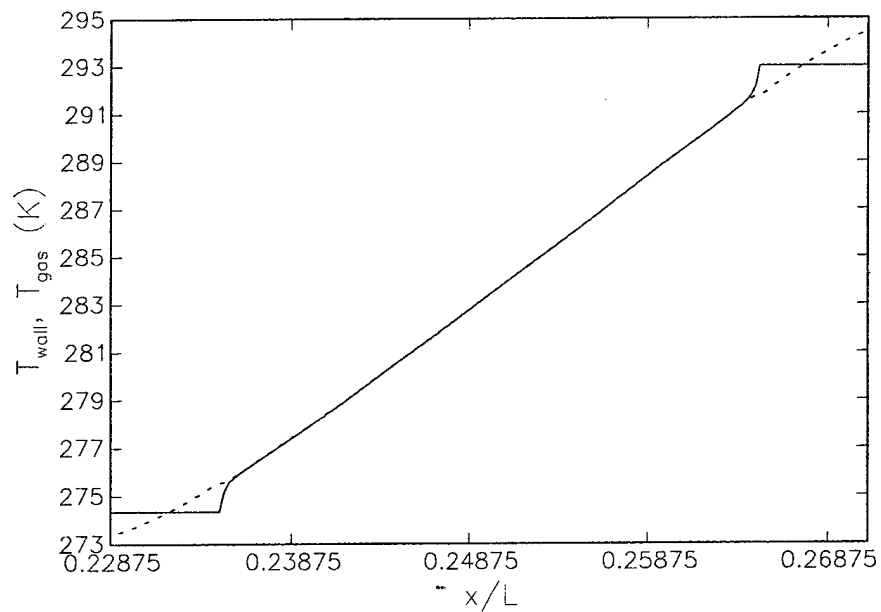


Figure 2.14: Mean steady-state temperature distribution in the region of the stack and the heat exchangers for the solid surfaces (solid line) and the gas (dotted line) for the driven tube of the previous figure.

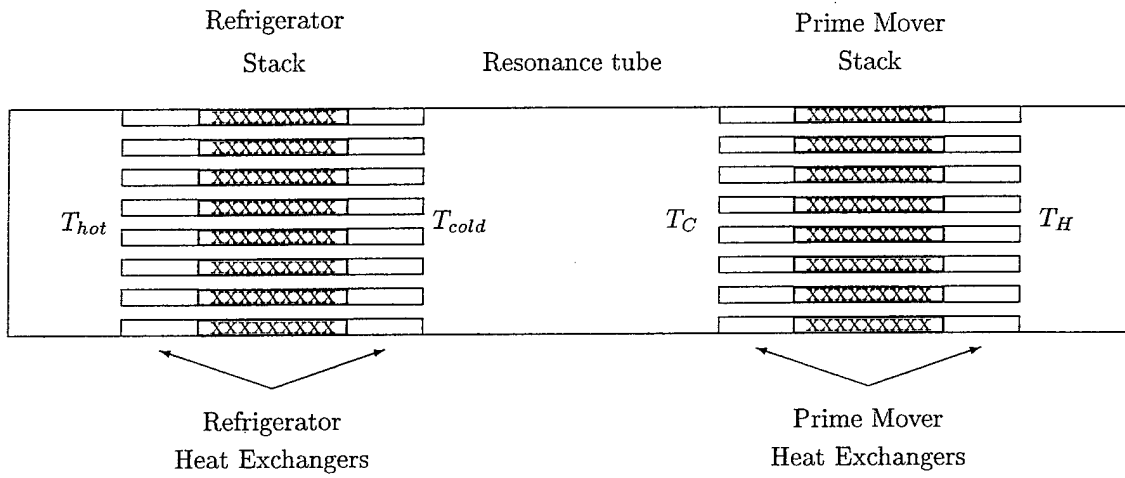


Figure 2.15: Schematic representation of a thermoacoustic prime mover/thermoacoustic refrigerator combination. A temperature difference $T_H - T_C$ is maintained across the prime mover stack by its heat exchangers. The standing wave generated by the prime mover stack causes a temperature difference across the refrigerator stack.

and it is lower over the other part. The same result was found in the two-dimensional calculation of Worlikar (1997), Worlikar and Knio (1999), and Mozurkevich (1998b).

2.6.3 Thermoacoustic Refrigerator Coupled with Prime Mover

As a final example we consider the combination of a thermoacoustic prime mover and a thermoacoustic refrigerator sketched in Fig. 2.15 housed in a 1 m-long rigidly terminated tube. The prime mover stack is located in the right part of the tube at $x_s/L = 0.26$ and the standing wave that it generates induces a temperature difference across the refrigerator stack positioned in the left part of the tube at $x_s/L = 0.73$.

As before we neglect blockage effects and gas-solid momentum and energy exchanges away from the stack/heat exchangers region. The gas is helium at a mean pressure of 307 kPa. The stacks and heat exchangers consist of 0.28 mm-thick parallel plates spaced by 0.77 mm with a length of 30 mm and 1.5 mm respectively. For the same reasons mentioned above we set the product $\rho_s c_s$ to 480 kW/(K m³). The thermal conductivity of the stack plates is $k_s = 0.48$ W/(K m) as before, whereas the plates of the refrigerator heat exchangers are assumed to have infinite thermal conductivity. The temperature of the prime-mover heat exchangers is prescribed to be $T_C = 293$ K, $T_H = 493$ K and held fixed. The temperatures of the refrigerator heat exchangers are allowed to change in a manner similar to the cold heat exchanger of the previous example. Initially the temperature is a uniform 293 K along the refrigerator stack, while it is a linear function along the prime mover stack.

Figure 2.16 shows the pressure at the cold end of the tube as a function of time. There is an initial fairly rapid rise up to a maximum amplitude reached at about 0.15 s, followed by a decline to the steady state regime which is essentially attained at 0.4 s. In order to understand this non-monotonic behavior we show in Fig. 2.17 the temperature at three positions in the prime mover stack, the midpoint and 1 mm away from each end. We see here that the temperatures near the two ends of the stack move in opposite directions approaching each other so much so that the initial temperature gradient of 6.67 K/mm prevailing along most of the stack is reduced at steady state to only 4 K/mm (except for the 1 mm-long segments adjacent the heat exchangers). The amplitude decrease of Fig. 2.16 clearly occurs as a consequence of this trend. While the pressure reaches steady state at about 0.4 s, the stack temperatures continue to slowly adjust after this time but without a significant change in the temperature gradient.

Turning now to the refrigerator section, we show in Fig. 2.18 the temperatures of the two heat exchangers

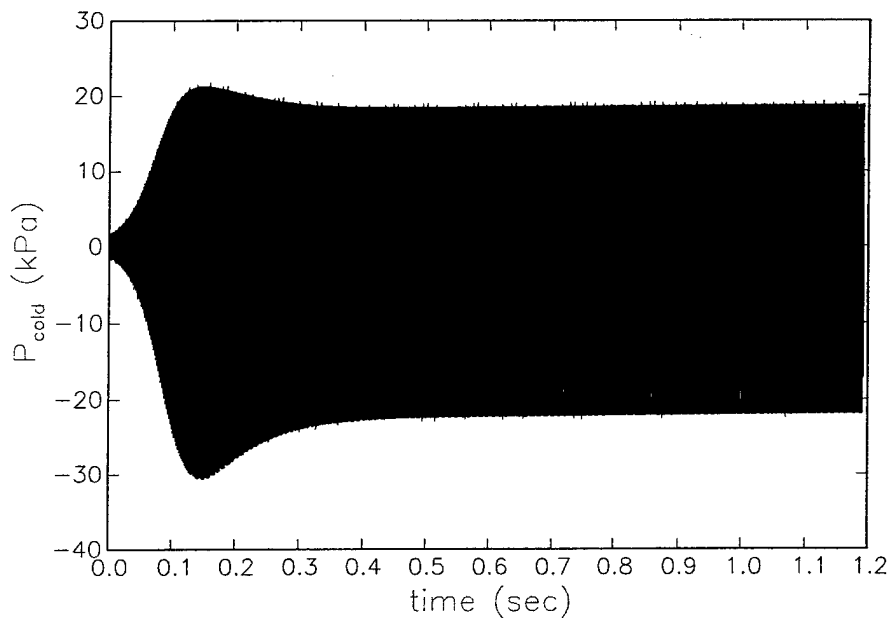


Figure 2.16: Transient behavior of the pressure at the cold end of the tube for the thermoacoustic prime mover/refrigerator combination sketched in the previous figure. Note the non-monotonic behavior of the pressure amplitude.

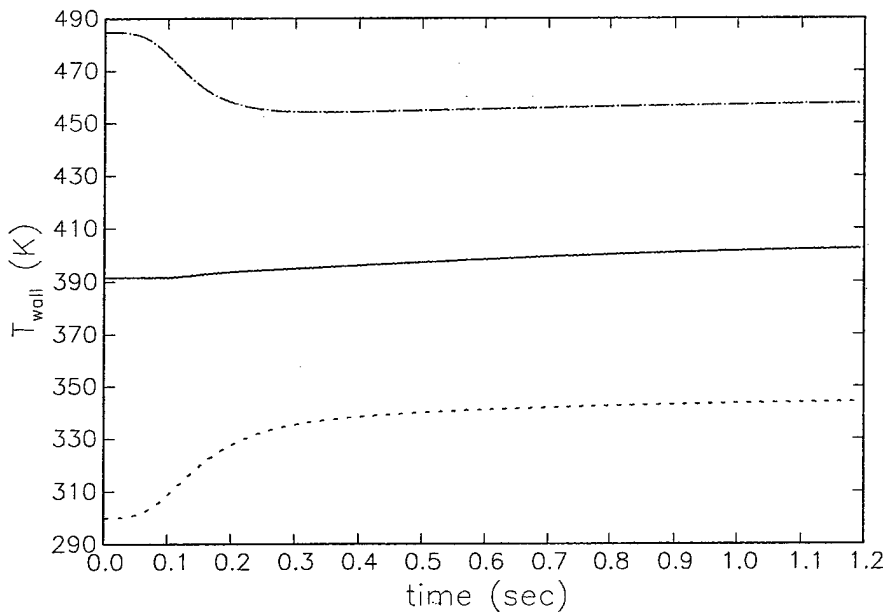


Figure 2.17: Temperature vs. time at three positions in the prime mover stack for the thermoacoustic prime mover/refrigerator combination of the previous two figures. The dot-dash and dotted lines lines are for points 1 mm away from the hot and cold heat exchangers, respectively; the solid line is for the stack midpoint. The initial temperature gradient of 6.67 K/mm is reduced to only 4 K/mm at steady state.

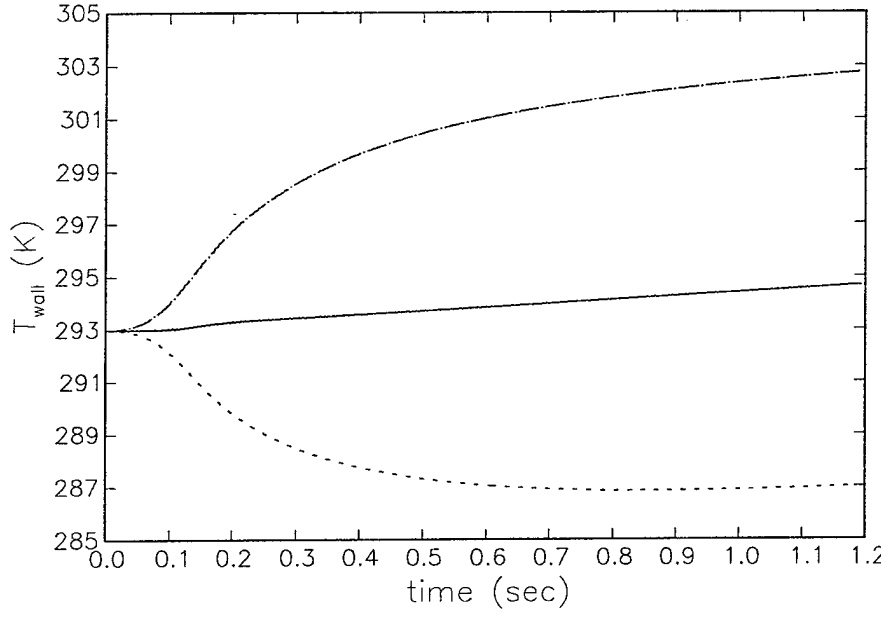


Figure 2.18: Temperature vs. time of the cold (dotted line) and hot (dot-dash line) heat exchangers and the stack midpoint (solid line) in the refrigerator unit of the thermoacoustic prime mover/refrigerator combination of the previous three figures.

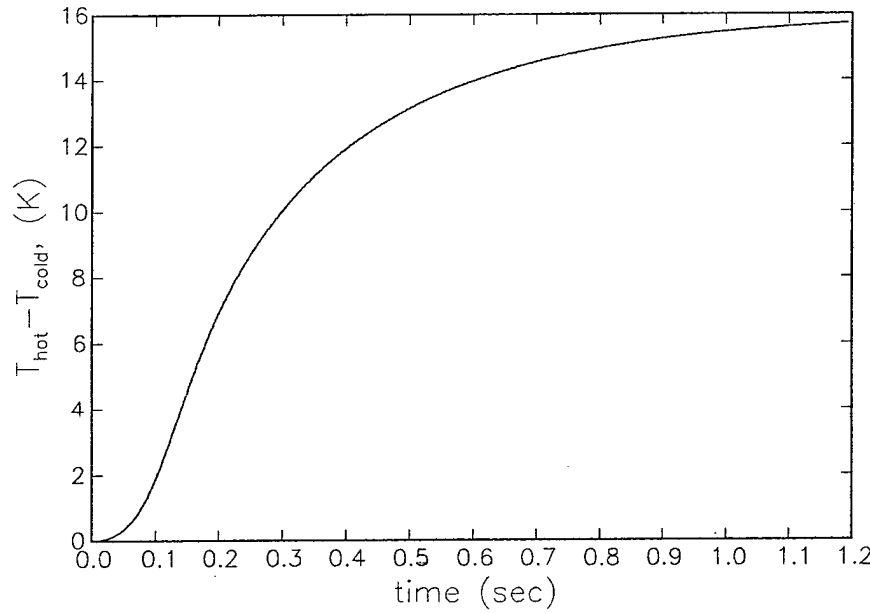


Figure 2.19: Temperature difference between the two heat exchangers vs. time in the refrigerator unit of the thermoacoustic prime mover/refrigerator combination of the previous figures.

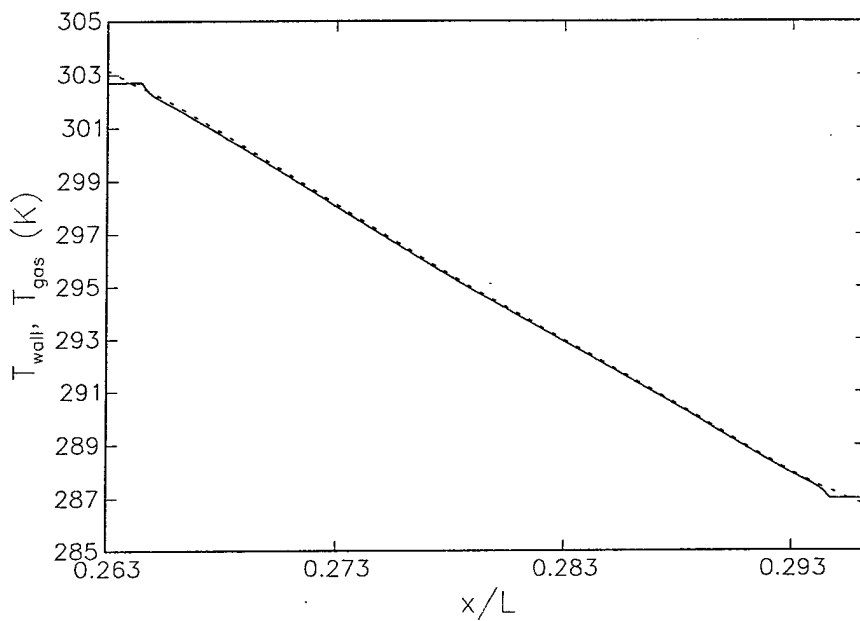


Figure 2.20: Mean steady-state temperature distributions in the the refrigerator stack and connected heat exchangers for the solid surfaces (solid line) and the gas (dotted line) for the thermoacoustic prime mover/refrigerator combination sketched in Fig. 2.15.

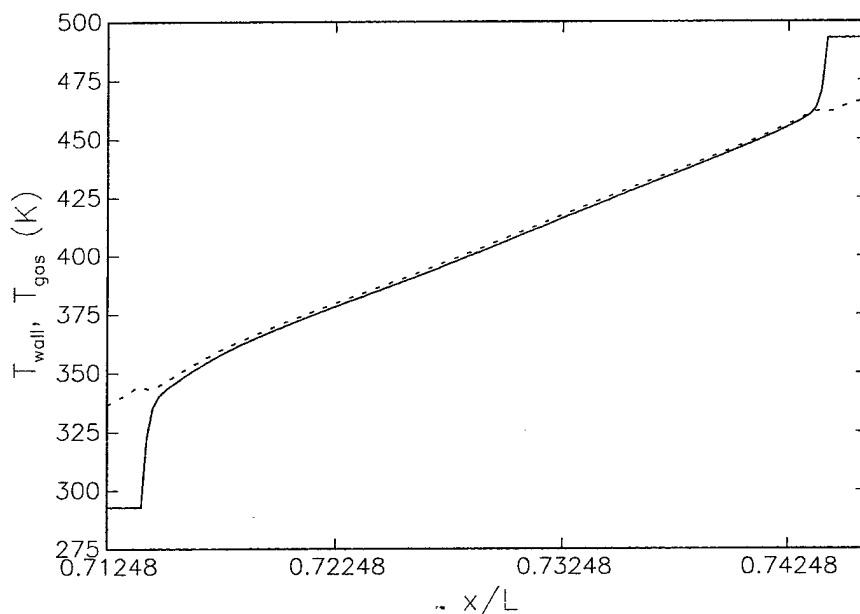


Figure 2.21: Mean steady-state temperature distributions in the the prime mover stack and connected heat exchangers for the solid surfaces (solid line) and the gas (dotted line) for the thermoacoustic prime mover/refrigerator combination sketched in Fig. 2.15.

and of the stack midpoint, all as functions of time. The temperatures of the cold and hot heat exchangers initially move in opposite directions, as expected. However, after about 1.0 s, the temperature of the cold heat exchanger starts increasing due to viscous and thermal heating of the refrigerator stack and its heat exchangers. For the refrigerator stack the temperature changes much more slowly than for the prime mover stack reaching its steady state only after 1.2 s. Figure 2.19 shows the temperature difference between the two refrigerator section heat exchangers as a function of time.

Figures 2.20 and 2.21 show the final mean temperature distributions for the refrigerator and prime mover stacks and connected heat exchangers. Significant temperature differences between the plates (solid lines) and the gas occur only near the heat exchangers. For the refrigerator stack the gas temperature is higher than the solid temperature over one part of the heat exchanger and lower over another part as found before.

2.7 Conclusions

We have described a simplified, quasi-one-dimensional, time-domain mathematical model of thermoacoustic prime movers and heat pumps. The model is quite flexible as demonstrated by the examples that we have presented: a prime mover, a combined prime mover/refrigerator system, and a piston-driven refrigerator. We have been able to follow in the time domain the evolution of these systems and, for the first two, we have presented results that trace the evolution of the initial linear instability to the nonlinear regime, and finally to steady state where the instability saturates to a finite amplitude. This is a specifically nonlinear effect that cannot possibly be captured by models based on a linear approximation. We have also tested the model successfully for the prime mover/refrigerator combination assuming periodicity boundary conditions; we have not shown these results as, for the conditions tested, the system turned out to be stable.

It is apparent from the equations presented in sections 2.2 to 2.4 that the model includes several nonlinear mechanisms. In the first place, it accounts for mode-mode coupling. Even though in actual thermoacoustic engines the resonator is built so as to detune the harmonics, at sufficiently large amplitudes a coupling still exists and represents a significant mechanism for energy loss: in a thermoacoustic engine, typically it is only the fundamental mode that is unstable, while all higher modes are damped. Hence, energy leaking out of the fundamental mode into higher ones is dissipated; a weakly nonlinear analysis of this phenomenon is presented in Karpov & Prosperetti (2000). Similarly, in a refrigerator, the stack is badly positioned with respect to the spatial distribution of pressure and velocity for modes other than the fundamental, which leads to a loss of efficiency. Secondly, the model does not contain any limitation on the displacement s of the fluid particles and, therefore, it dispenses with the standard assumption of linear theory in which $s dT_w/dx \ll T_w$. On the other hand, it must be recognized that other nonlinearities are not accounted for. For example, the effects of acoustic streaming or those of vortex shedding from geometric discontinuities are not included. While the latter could possibly be accounted for by lumped resistances in a finite-difference implementation, inclusion of the former appears to be more difficult. It may also be noted that the cross-stream momentum and heat exchange terms are modelled linearly, which is however justified by the fact that, typically, the stack is many hydraulic diameters long, so that a fully developed, parallel-flow approximation is warranted.

While these and other mechanisms and other details of a real thermoacoustic system may not be easily incorporated in the model, a great variety of design parameters can be accounted for such as geometry (and in particular a non-constant cross section), physical properties, temperature conditions, standing and travelling waves, and others. Thus we believe that – at the very least – the present model can be used in a relative sense to compare the effect of proposed design modifications and to gain insight into the performance of new systems.

References

- Arnott, W.P., Bass, H.E., & Raspert, R., 1991, General formulation of thermoacoustics for stacks having arbitrarily shaped pore cross sections, *J. Acoust. Soc. Am.*, **90**, 3228–3237.
- Arnott, W.P., Bass, H.E., & Raspert, R., 1992, Specific acoustic impedance measurements of an air-filled thermoacoustic prime mover, *J. Acoust. Soc. Am.*, **92**, 3432–3434.
- Atchley, A.A., 1994, Analysis of the initial build-up of oscillations in a thermoacoustic prime mover, *J. Acoust. Soc. Am.*, **95**, 1661–1664.
- Atchley, A.A., Bass, H.E., & Hofler, T.J., 1990, Development of nonlinear waves in a thermoacoustic prime mover, in *Frontiers in Nonlinear Acoustics*, Hamilton, M.F. & Blackstock, D.T., eds., Elsevier, 603–608.
- Atchley, A.A., Bass, H.E., Hofler, T.J., & Lin, H.-T., 1992, Study of a thermoacoustic prime mover below onset of self-oscillation, *J. Acoust. Soc. Am.*, **91**, 734–743.
- Atchley, A.A., Hofler, T.J., Muzzellall, M.L., Kite, M.D., & Ao, C., 1990, Acoustically generated temperature gradients in short plates, *J. Acoust. Soc. Am.*, **88**, 251–263.
- Atchley, A.A. & Kuo, F.M., 1994, Stability curves for a thermoacoustic prime mover, *J. Acoust. Soc. Am.*, **95**, 1401–1404.
- Bauwens, L., 1996, Oscillating flow of a heat-conducting fluid in a narrow tube, *J. Fluid Mech.*, **324**, 135–161.
- Bauwens, L., 1998, Thermoacoustics: Transient regimes and singular temperature profiles, *Phys. Fluids*, **10**, 807–818.
- Besnoin, E. & Knio, O., 2001, Numerical study of thermoacoustic heat exchangers in the thin plate limit, *Numer. Heat Transfer* **45**, 445–471.
- Cao, N., Olson, J.R., Swift, G.W., & Chen, S., 1996, Energy flux density in a thermoacoustic couple, *J. Acoust. Soc. Am.*, **99**, 3456–3464.
- Crocce, L., One-dimensional treatment of steady gas dynamics, in *Fundamentals of Gas Dynamics*, Emmons, H.W., ed., Princeton U.P., 1958, 64–349.
- Fletcher, C.A.J., 1988, *Computational Techniques for Fluid Dynamics*, Springer, Berlin.
- Gaitan, D.F. & Atchley, A.A., 1993, Finite amplitude standing waves in harmonic and anharmonic tubes, *J. Acoust. Soc. Am.*, **93**, 2489–2495.
- Gopinath, A., Tait, N.L., & Garrett, S.L., 1998, Thermoacoustic streaming in a resonant channel: The time-averaged temperature distribution, *J. Acoust. Soc. Am.*, **103**, 1388–1405.
- Harten, A., 1983, High resolution schemes for hyperbolic conservation laws, *J. Comp. Phys.*, **49**, 357–393.
- Harten, A. & Osher, S., 1987, Uniformly high-order accurate nonoscillatory schemes. i., *SIAM J. Numer. Anal.*, **24**, 279–309.
- Harten, A., Osher, S., Engquist, B., & Chakravarthy, R., 1986, Some results on uniformly high-order accurate essentially nonoscillatory schemes, *Appl. Numer. Math.*, **2**, 347–377.
- Hinch, E.J., 1991, *Perturbation Methods*, Cambridge U.P., Cambridge.

- Ilinskii, Y.A., Lipkens, B., Lucas, T.S., Van Doren, T.W., & Zabolotskaya, E.A., 1998, Nonlinear standing waves in an acoustical resonator, *J. Acoust. Soc. Am.*, **104**, 2664–2674.
- Incropera, F.P. & DeWitt, D.P., 1996, *Fundamentals of Heat and Mass Transfer*, Wiley, New York, 4th ed.
- Kamath, V., Prosperetti, A., & Egolfopoulos, F., 1993, A theoretical study of sonoluminescence, *J. Acoust. Soc. Am.*, **94**, 248–260.
- Karpov, S. & Prosperetti, A., 1998, Linear thermoacoustic instability in the time domain, *J. Acoust. Soc. Am.*, **103**, 3309–3317.
- Karpov, S. & Prosperetti, A., 2000, Nonlinear saturation of the thermoacoustic instability, *J. Acoust. Soc. Am.*, **107**, 3130–3147.
- Kevorkian, J. & Cole, J.D., 1996, *Perturbation Methods in Applied Mathematics*, Springer, New York, 2nd ed.
- Landau, L.D. & Lifshitz, E.M., 1959, *Fluid Mechanics*, Pergamon.
- Merkli, P. & Thomann, H., 1975, Thermoacoustic effects in a resonance tube, *J. Fluid Mech.*, **70**, 161–177.
- Morse, P.M. & Feshbach, H., 1953, *Methods of Theoretical Physics*, McGraw-Hill, New York.
- Mozurkevich, G., 1998, A model for transverse heat transfer in thermoacoustics, *J. Acoust. Soc. Am.*, **103**, 3318–3326.
- Murdock, J.A., 1991, *Perturbations*, Wiley, New York.
- Naugolnykh, K. & Ostrovsky, L., 1998, *Nonlinear Wave Processes in Acoustics*, Cambridge U.P., Cambridge U.K.
- Naylor, A.W. & Sell, G.R., 1982, *Linear Operator Theory in Engineering and Science*, Springer, New York, 2nd ed.
- Nigmatulin, R.I., 1991, *Dynamics of Multiphase Media*, Hemisphere, Washington.
- Olson, J.R. & Swift, G.W., 1994, Similitude in thermoacoustics, *J. Acoust. Soc. Am.*, **95**, 1405–1412.
- Osher, S., 1984, Riemann solvers, the entropy condition, and difference approximation, *SIAM J. Numer. Anal.*, **21**, 217–235.
- Osher, S. & Chakravarthy, R., 1984, High resolution schemes and the entropy condition, *SIAM J. Numer. Anal.*, **21**, 955–984.
- Plesset, M.S. & Prosperetti, A., 1977, Bubble dynamics and cavitation, *Ann. Rev. Fluid Mech.*, **9**, 145–185.
- Prosperetti, A., 1991, The thermal behaviour of oscillating gas bubbles, *J. Fluid Mech.*, **222**, 587–616.
- Prosperetti, A., Fundamental acoustic properties of bubbly liquids, in *Handbook of Elastic Properties of Solids, Liquids, and Gases*, Levy, Bass, & Stern, eds., vol. 4, Academic Press, New York, 2001, 183–205.
- Prosperetti, A. & Watanabe, M., 1994, Simplified model for the study of nonlinear processes in thermoacoustic engines, *J. Acoust. Soc. Am.*, **96**, 3220.

- Raspet, R., Bass, H.E., & Kordomenos, J., 1993, Thermoacoustics of traveling waves: Theoretical analysis for an inviscid ideal gas, *J. Acoust. Soc. Am.*, **94**, 2232–2239.
- Rayleigh, Lord, 1896, *The Theory of Sound*, Macmillan, London. Reprinted by Dover, 1945.
- Roe, P.L., 1986, Characteristic-based schemes for the Euler equations, *Annu. Rev. Fluid Mech.*, **18**, 337–365.
- Rott, N., 1969, Damped and thermally driven acoustic oscillations in wide and narrow tubes, *Z. Angew. Math. Phys.*, **20**, 230–243.
- Rott, N., 1976, Thermally driven acoustic oscillations, Part IV: Tubes with variable cross section, *Z. Angew. Math. Phys.*, **27**, 197–224.
- Rott, N., 1980, Thermoacoustics, *Adv. Appl. Mech.*, **20**, 135–175.
- Rott, N., 1983, Thermally driven acoustic oscillations, Part VI: Excitation and power, *Z. Angew. Math. Phys.*, **34**, 609–626.
- Sod, G.A., 1978, A survey of several finite difference methods for systems of nonlinear hyperbolic conservation laws, *J. Comput. Phys.*, **27**, 1–31.
- Sweby, P.K., 1984, High resolution schemes using flux limiters for hyperbolic conservation laws, *SIAM J. Numer. Anal.*, **21**, 995–1011.
- Swift, G.W., 1988, Thermoacoustic engines, *J. Acoust. Soc. Am.*, **84**, 1145–1180.
- Swift, G.W., 1992, Analysis and performance of a large thermoacoustic engine, *J. Acoust. Soc. Am.*, **92**, 1551–1563.
- Swift, G.W. & Keolian, R., 1993, Thermoacoustics in pin-array stacks, *J. Acoust. Soc. Am.*, **93**, 1–9.
- Tominaga, A., 1995, Thermodynamic aspects of thermoacoustic theory, *Cryogenics*, **35**, 427–440.
- Watanabe, M. & Prosperetti, A., 1994, Shock waves in dilute bubbly liquids, *J. Fluid Mech.*, **274**, 349–381.
- Wheatley, J., Intrinsically irreversible or natural heat engines, in *Frontiers in Physical Acoustics*, Sette, D., ed., North-Holland, 1986, 35–475.
- Wheatley, J., Hofler, T., Swift, G.W., & Migliori, A., 1983, An intrinsically irreversible thermoacoustic engine, *J. Acoust. Soc. Am.*, **74**, 153–170.
- Worlikar, A.S., *Numerical simulation of a thermoacoustic refrigerator*, PhD thesis, Johns Hopkins University, 1997.
- Worlikar, A.S. & Knio, O.M., 1996, Numerical simulation of a thermoacoustic refrigerator. Part I: Unsteady adiabatic flow around the stack, *J. Comput. Phys.*, **127**, 424–451.
- Worlikar, A.S. & Knio, O.M., 1998, Numerical simulation of a thermoacoustic refrigerator. Part II: Stratified flow around the stack, *J. Comput. Phys.*, **144**, 299–324.
- Worlikar, A.S. & Knio, O.M., 1999, Numerical study of oscillatory flow and heat transfer in a loaded thermoacoustic stack, *Numer. Heat Transfer*, **A35**, 49–65.
- Worlikar, A.S., Knio, O.M., & Klein, R., 1998, Numerical simulation of a thermoacoustic refrigerator. II Stratified flow around the stack, *J. Comput. Phys.*, **144**, 299–324.

Yazaki, T., Takashima, S., & Mizutani, S., 1987, Complex quasiperiodic and chaotic states observed in thermally induced oscillations of gas columns, *Phys. Rev. Lett.*, **58**, 1108–1111.

Yazaki, T., Tominaga, A., & Narahara, Y., 1980, Experiments on thermally driven acoustic oscillations of gaseous helium, *J. Low Temp. Phys.*, **41**, 45–60.

Zhang, D.Z. & Prosperetti, A., 1994, Ensemble phase-averaged equations for bubbly flows, *Phys. Fluids*, **6**, 2956–2970.

Chapter 3

Linear and Weakly Nonlinear Theory of Thermoacoustic Devices

The nonlinear model described in the preceding chapter and its numerical treatment are, we believe, the most significant piece of work in Thermoacoustics completed in the course of this project. In parallel, we have also conducted analytical work aimed at finding a time-domain description of the phenomena, both in the linear and in the nonlinear regime. This work has been based on the same approximate formulation described in the previous chapter but, since the different normal modes are here treated individually, the terms responsible for the cross-axis exchange of momentum and energy can be treated more accurately.

Here we only present a brief description of this work; full details are given in the two publications resulting from these studies: Karpov & Prosperetti (1998) and Karpov & Prosperetti 2000.

3.1 Introduction

This work is based on a perturbative treatment of the problem, which is motivated by the observation that both experiment (see e.g. Wheatley 1986; Atchley 1994) and the calculations described in the previous chapter show that the initial build-up of the thermoacoustic instability has the character of a modulated standing wave the frequency of which is essentially dictated by the resonator, while the amplitude is slowly varying in time. Similarly, if the thermoacoustic device is driven externally by a loudspeaker or a piston, the steady state temperature distribution evolves slowly over the time scale of the acoustic period. These observations suggests the possibility of setting up a perturbation scheme based on the smallness of the ratio of the characteristic period of oscillation to the characteristic time for the evolution of the thermoacoustic effect.

We start from the same mathematical model of the previous chapter, which is here repeated for the reader's convenience:

$$\frac{\partial \rho}{\partial \hat{t}} + \frac{1}{S} \frac{\partial}{\partial x} (S \rho u) = 0, \quad (3.1)$$

$$\frac{\partial \rho u}{\partial \hat{t}} + \frac{1}{S} \frac{\partial}{\partial x} (S \rho u^2) + \frac{\partial p}{\partial x} = -\mathcal{D}(\rho u), \quad (3.2)$$

$$\frac{\partial p}{\partial \hat{t}} + u \frac{\partial p}{\partial x} + \frac{\gamma p}{S} \frac{\partial}{\partial x} (S u) = (\gamma - 1) \left[\rho c_p \mathcal{H}(T_w - T) - c_p \frac{\partial T_w}{\partial x} \mathcal{Q}(\rho u) + u \mathcal{D}(\rho u) \right]. \quad (3.3)$$

All the terms are described in detail in section 2 of the previous chapter; time is denoted by \hat{t} for reasons that will become soon apparent. For simplicity, and in view of the large thermal capacity of typical stack plates, we assume in this chapter that $T_w = T_w(x)$ is a prescribed function of x . With relatively straightforward

adjustments, however, the present method can be extended to deal with a T_w dependent on time over the fast time scale of the acoustic oscillations as well as over the slower time scale of the developing instability.

For the exchange terms \mathcal{D} , \mathcal{H} , and \mathcal{Q} we use the exact form of the linear theory as described in the previous chapter, namely

$$\mathcal{D}(\rho u) = i\hat{\omega} \frac{f_V}{1-f_V} \rho_0 u, \quad (3.4)$$

$$\mathcal{H}(T_w - T) = i\hat{\omega} \frac{f_K}{1-f_K} (T_w - T), \quad (3.5)$$

$$\mathcal{Q}(\rho u) = \frac{1}{1-\sigma} \left(\frac{f_V}{1-f_V} - \frac{\sigma f_K}{1-f_K} \right) \rho_0 u, \quad (3.6)$$

where the functions $f_{V,K}$ depend on the viscous and thermal penetration length at the frequency $\hat{\omega}$ and are given in (2.22) for the plane geometry and in (2.30) for the cylindrical geometry. It will be noted that we have replaced the density ρ in the right-hand side by the unperturbed equilibrium density ρ_0 . This we do for simplicity on the basis of numerical results obtained by the method of the previous chapter which show that this simplification has a negligible effect.

In the model (3.1) to (3.3), the terms in the left-hand sides describe non-linear oscillations in a gas column with variable cross sectional area and temperature stratification and are therefore responsible for the “carrier” frequency of the wave. The heart of the thermoacoustic effect is in the terms in the right-hand sides. The observed slowness of the modulation implies that the effect of these terms over a single period of oscillation is small. As will be seen in the following, this effect arises through integrals over the tube length. Therefore, the effect will be small not only when the terms themselves are small but – as usually happens in practice – when they are large only over a small fraction of the tube length. This statement can be formally justified as shown in Appendix A of Karpov & Prosperetti (2000).

In order to set up a perturbation scheme, we introduce a small parameter ϵ and set

$$F_K = \frac{f_K}{\epsilon}, \quad F_Q = \frac{1}{\epsilon} \frac{f_V - f_K}{(1-f_V)(1-\sigma)}, \quad F_D = \frac{1}{\epsilon} \frac{f_V}{1-f_V}, \quad (3.7)$$

with $F_{K,Q}$ formally treated as $O(1)$ quantities. As shown in Karpov & Prosperetti (2000), this does not necessarily imply that the f ’s are of order ϵ , but only that

$$\frac{L_S}{L} f_{V,K} \sim \epsilon, \quad (3.8)$$

where L_S is the length of the stack region, i.e., the region where the f ’s are not small. An explicit definition of ϵ is not necessary as the final results do not explicitly depend on this parameter, but one may think of it as the ratio of the standing wave period to the modulation time scale. We use the method of multiple time scales (see e.g. Kevorkian and Cole 1996; Murdock 1991; Hinch 1991) and introduce the new time variables

$$t = \hat{t}, \quad \tau = \epsilon \hat{t}, \quad \theta = \epsilon^2 \hat{t}, \quad \eta = \epsilon^3 \hat{t}. \quad (3.9)$$

As a consequence of these definition we have

$$\frac{\partial}{\partial \hat{t}} = \frac{\partial}{\partial t} + \epsilon \frac{\partial}{\partial \tau} + \epsilon^2 \frac{\partial}{\partial \theta} + \epsilon^3 \frac{\partial}{\partial \eta} + \dots \quad (3.10)$$

The field variables are also expanded in a power series in ϵ ; for example

$$p(x, \hat{t}) = p_0 + \epsilon p_1(x, \hat{t}) + \epsilon^2 p_2(x, \hat{t}) + \epsilon^3 p_3(x, \hat{t}) + \epsilon^4 p_4(x, \hat{t}) + \dots, \quad (3.11)$$

with analogous expressions for u' etc. These expansions imply that the nonlinearity is taken to be of the same order as the amplitude modulation, which is the interesting case. Indeed, if the modulation were much stronger than the nonlinearity, we would essentially be dealing with the linear problem (see Karpov &

Prosperetti 1998 for an analysis of it). On the other hand, since the wave exists only due to the thermoacoustic instability, one cannot have a strong nonlinearity coupled with weak thermoacoustic effects. As a consequence of an expansion analogous to (3.11) for u , we may write

$$\mathcal{D}(\rho u) = \epsilon^2 \mathcal{D}_1 + \epsilon^3 \mathcal{D}_2 + \epsilon^4 \mathcal{D}_3 + \dots ; \quad (3.12)$$

the expansion begins with a term of order ϵ^2 since \mathcal{D} is itself of order ϵ as implied by (3.4) and (3.7).

For clarity, it is important to stress two important aspects in which the work described in this paper differs from most other non-linear stability studies. In the first place, while the deviation from marginal stability conditions is usually measured by a single control variable, here it is a whole function – the wall temperature distribution T_w – that determines the stability properties of the linear system. The situation might be reduced to the more usual one by assuming that the temperature distribution in the stack has a certain functional form dependent upon one parameter which would then play the role of control variable. For example, a linear temperature distribution would be characterized by the temperature gradient. Such an assumption is however unnecessarily restrictive and it is preferable to keep the framework general.

Secondly, perturbation expansions are usually carried out in the neighborhood of linear marginal stability conditions that are known exactly. In order to proceed in this way, we would have to solve the linear problem including the exchange terms $f_{V,K}$, find the marginal stability conditions, and then allow for a perturbation. Here such a procedure would not lead to very transparent results given the complexity of the linear problem, compounded by the fact that, with non-zero f 's, the linear operator is not self-adjoint. Hence, we prefer to take a different approach choosing as our base state the situation in which there is no coupling between the gas and the solid structure even though, in general, this situation is not marginally stable. The marginal stability condition will be determined as part of the perturbation procedure itself much as in our earlier paper (Karpov and Prosperetti 1998) of which the first few steps of the present perturbation procedure constitute a refinement.

Here, therefore, as the parameter ϵ is increased from zero, two effects appear: the coupling with the solid structure dampens or amplifies the oscillations, and nonlinear effects influence their development. It will be seen that the first effect sets in at a lower order in ϵ than the second one. The first few steps of the perturbation procedure, therefore, furnish successively closer approximations to the linear stability threshold, from which the nonlinear effects eventually take off.

In order to deal with this situation we must clarify the role played by the wall temperature distribution $T_w(x)$. In the usual perturbation procedures, the small parameter is the difference between the given value of the control variable and the critical value. Here we deal with the function T_w , and the critical conditions are not known exactly. Thus we represent the given function T_w as

$$T_w(x) = T_{w0}(x) + \epsilon T_{w1}(x) + \epsilon^2 T_{w2}(x) + \dots . \quad (3.13)$$

The terms T_{w0} , T_{w1} will be determined so as to satisfy the marginal stability conditions, after which the difference $T_w(x) - [T_{w0}(x) + \epsilon T_{w1}(x)]$ will be the driving force for the development of the instability to the order considered.¹ In principle, the same procedure can be applied to higher orders in ϵ . Since the appearance of the instability depends on integral conditions on the T_{wj} 's, in principle, there is a degree of non-uniqueness here since the T_{wj} 's can be taken arbitrarily, provided only the integral conditions are satisfied. In spite of this seeming level of arbitrariness, one would expect the results to be insensitive to any specific choice, and indeed we have verified this numerically as will be described below.

From (3.13), we also have

$$\frac{dT_w}{dx} = G_0 + \epsilon G_1 + \epsilon^2 G_2 + \dots . \quad (3.14)$$

where

$$G_j = \frac{dT_{wj}}{dx}, \quad j = 0, 1, 2, \dots . \quad (3.15)$$

¹More precisely, one could determine a value of T_{w2}^* corresponding to marginal stability, after which the difference $T_w(x) - [T_{w0}(x) + \epsilon T_{w1}(x) + \epsilon^2 T_{w2}^*]$ would be the driving force for the instability.

Furthermore, since the equilibrium density is connected to p_0 and T_w by the equation of state, when we write

$$\rho(x, \hat{t}) = \rho_0 + \epsilon \rho_1(x, \hat{t}) + \epsilon^2 \rho_2(x, \hat{t}) + \epsilon^3 \rho_3(x, \hat{t}) + \epsilon^4 \rho_4(x, \hat{t}) + \dots, \quad (3.16)$$

the corrections ρ_1 etc. will contain time-independent components related to T_{w1} etc. It is also convenient to introduce a term

$$\mathcal{T}(p, u) \equiv \rho \mathcal{H} (T_w - T) - \frac{dT_w}{dx} Q(\rho u) = -i\omega f_K(p - p_0) - \rho c_p \frac{f_V - f_K}{(1 - f_V)(1 - \sigma)} \frac{dT_w}{dx} u, \quad (3.17)$$

where the last step is justified by relations valid in the linear approximation.² Upon substituting the previous ϵ -expansions, we find

$$\mathcal{T}(p, u) = \epsilon^2 \mathcal{T}_1 + \epsilon^3 \mathcal{T}_2 + \epsilon^4 \mathcal{T}_3 + \dots, \quad (3.18)$$

where

$$\mathcal{T}_1 = -i\omega F_K p_1 - \rho_0 c_p F_Q G_0 u_1, \quad \mathcal{D}_1 = i\rho_0 \omega F_V u_1, \quad (3.19)$$

etc.

All the expansions, together with (3.10), are now substituted into the equations (2.1) to (2.11) and the various orders in ϵ are separated giving rise to a sequence of problems. At order zero the solution is simply

$$u_0 = 0, \quad (3.20)$$

with p_0 and $T_0 = T_{w0}(x)$ arbitrary but regarded as given.

3.2 The First-Order Problem

At order ϵ the equations are

$$\frac{\partial \rho_1}{\partial t} + \frac{1}{S} \frac{\partial}{\partial x} (S \rho_0 u_1) = 0, \quad (3.21)$$

$$\rho_0 \frac{\partial u_1}{\partial t} + \frac{\partial p_1}{\partial x} = 0, \quad (3.22)$$

$$\frac{\partial p_1}{\partial t} + \frac{\gamma p_0}{S} \frac{\partial (S u_1)}{\partial x} = 0, \quad (3.23)$$

from which the pressure field is found to be

$$p_1 = A(\tau, \theta, \eta) P_1(x) \exp(i\omega t) + \text{c.c.}, \quad (3.24)$$

where A is the slowly-varying amplitude, c.c. denotes the complex conjugate, and P_1 is the solution of

$$\frac{1}{S} \frac{d}{dx} \left(c_0^2(x) S \frac{dP_1}{dx} \right) + \omega^2 P_1 = 0, \quad (3.25)$$

where

$$c_0^2(x) = \gamma \mathcal{R} T_{w0}(x), \quad (3.26)$$

is the local adiabatic sound speed. We take the tube to be rigidly terminated at the ends and therefore impose that

$$\frac{dP_1}{dx} = 0 \quad \text{at } x = 0, \quad x = L, \quad (3.27)$$

²We have verified numerically that the use of this relation in the nonlinear regime leads to a better agreement with the complete nonlinear theory.

which ensure that the eigenvalue ω^2 is real and positive (see e.g. Morse and Feshbach 1953, p. 728; Naylor and Sell 1982, p. 502). The eigenfunction P_1 can therefore also be taken real and, for later convenience, we normalize it so that

$$\int_0^L S(x) P_1^2(x) dx = V p_0^2, \quad (3.28)$$

where V is the volume of the device.

The way in which T_{w0} is to be understood needs some clarifications, that amplify the comments made before Eq. (3.13). Let us consider first the case in which a certain temperature distribution $T_w(x)$ is prescribed. If one plans to study only the linear problem, T_{w0} can be taken as the given T_w . On the other hand, if the plan is to carry the expansion to include nonlinear effects, as will be discussed below, T_{w0} must be determined (or, at least, constrained) using the results of the next step in the perturbation procedure. Finally, if the objective is the determination of the onset temperature distribution, $T_w(x)$ is unknown at the outset, and the T_{w0} appearing in (3.25) is its first approximation that will be determined at the next step. Actually, the last two possibilities are one and the same as, if one plans to carry the expansion to include nonlinear effects, one needs to determine the onset temperature distribution first. A consequence of the indeterminacy of T_{w0} at this stage is an indeterminacy of ρ_0 , which will be determined from the equation of state $\mathcal{R}\rho_0 T_{w0} = p_0$ once T_{w0} is found.

In deriving an expression for the gas density to this order, we anticipate the fact that, at the next order, we will encounter a contribution T_{w1} that will affect the undisturbed value of ρ . Hence we write

$$\rho_1 = \rho_{10} + \rho_{11}, \quad (3.29)$$

where ρ_{10} will be determined at the third step from the equation of state

$$\mathcal{R}(\rho_0 + \epsilon\rho_{10})(T_{w0} + \epsilon T_{w1}) = p_0. \quad (3.30)$$

The term ρ_{11} is instead associated to p_1 and can be found from (3.21) to (3.23), together with u_1 . The dependence of both quantities on the time variables and the perturbation amplitude A is the same as (3.24), and the spatial dependence is given by

$$R_1(x) = -\frac{1}{\omega^2 S} \frac{d}{dx} \left(S \frac{dP_1}{dx} \right), \quad (3.31)$$

$$U_1(x) = \frac{i}{\omega\rho_0} \frac{dP_1}{dx}. \quad (3.32)$$

3.3 Second-Order Problem

At order ϵ^2 , one finds the following equation for p_2 :

$$\frac{\partial^2 p_2}{\partial t^2} - \frac{1}{S} \frac{\partial}{\partial x} \left(c_0^2 S \frac{\partial p_2}{\partial x} \right) = (RHS)_2, \quad (3.33)$$

where c_0^2 is defined in (3.26) and

$$\begin{aligned} (RHS)_2 &= (\gamma - 1) \frac{\partial T_1}{\partial t} - 2 \frac{\partial^2 p_1}{\partial t \partial \tau} - \frac{\partial}{\partial t} \left[u_1 \frac{\partial p_1}{\partial x} + \frac{\gamma p_1}{S} \frac{\partial}{\partial x} (S u_1) \right] \\ &\quad + \frac{\gamma p_0}{S} \frac{\partial}{\partial x} S \left[\frac{1}{\rho_0} \mathcal{D}_1 + u_1 \frac{\partial u_1}{\partial x} + \frac{\rho_1}{\rho_0} \frac{\partial u_1}{\partial t} \right] \\ &= - \left\{ 2i\omega \frac{\partial A}{\partial \tau} - \frac{A}{\epsilon} \left[\frac{1}{S} \frac{\partial}{\partial x} \left(\frac{if_V}{1-f_V} \omega \rho_0 S c_0^2 U_1 \right) + (\gamma - 1) \omega^2 f_K P_1 \right. \right. \\ &\quad \left. \left. - i \frac{f_V - f_K}{(1-\sigma)(1-f_V)} \gamma \frac{\omega p_0 U_1}{T_{w0}} \frac{dT_{w0}}{dx} \right] \right\} \exp i\omega t + c.c.. \end{aligned} \quad (3.34)$$

The forcing at frequencies $\pm\omega$ in the right-hand side will generate resonant terms proportional to $t \exp(\pm i\omega t)$ in the solution for p_2 which would lead to a breakdown of the approximation over times of order $(\epsilon\omega)^{-1}$. To avoid this resonance, as in the standard procedure (Kevorkian and Cole 1996; Murdock 1991; Hinch 1991), we impose the solvability condition that the right-hand side of the equation be orthogonal to the solutions of the (adjoint) homogeneous equation, namely $\exp(\pm i\omega t) P_1$:

$$\int_0^{2\pi/\omega} dt \int_0^L S [\exp(\mp i\omega t) P_1] (RHS)_2 dx = 0. \quad (3.35)$$

Multiplication by $S(x)$ before integration is necessary so that the x -operator in the left-hand side of (3.33) be self-adjoint with the boundary conditions (3.27). The two conditions (3.35) give

$$\frac{\partial A}{\partial \tau} - i\Omega_1 A = 0, \quad (3.36)$$

plus its complex conjugate, where

$$\begin{aligned} \Omega_1 = & -\frac{1}{2Vp_0^2\omega} \int_0^L S \left[c_0^2 \left(F_D + \frac{\rho_{10}}{\rho_0} \right) \left(\frac{dP_1}{dx} \right)^2 \right. \\ & \left. + (\gamma - 1)\omega^2 F_K P_1^2 + (\gamma - 1)c_p F_Q G_0 P_1 \frac{dP_1}{dx} \right] dx. \end{aligned} \quad (3.37)$$

The solution of (3.36) is

$$A(\tau, \theta, \eta) = B(\theta, \eta) \exp(i\Omega_1 \tau), \quad (3.38)$$

which increases exponentially if $\text{Im } \Omega_1 < 0$. It will be noted that $\text{Im } \Omega_1$ exists only due to the F -terms that account for momentum and energy exchange with the solid structure and is therefore not affected by the indeterminacy of ρ_{10} at this stage of the calculation. It will be seen below that, in order to continue the perturbation scheme into the nonlinear domain, for consistency it is necessary to have $\text{Im } \Omega_1 = 0$, which is a constraint on G_0 and, therefore, T_{w0} . This constraint can of course be met in an infinity of ways although one would not expect any particular choice to have consequences for the remainder of the calculation provided the choice is such that $T_w - T_{w0} = O(\epsilon)$ in keeping with (3.13). Indeed, as will be shown below, this is in agreement with our numerical evidence.

Although essentially a linear result, (3.37) is already rather interesting. We have shown (Karpov & Prosperetti 1998) how, assuming a linear temperature gradient, one can deduce from it the onset value G_0 . By means of the short-stack approximation, it was also possible to derive simple formulae that generalize the concept of critical gradient of elementary theory to the presence of viscous effects and narrow gaps.

When (3.35) is satisfied, one can look for the solution of Eq. (3.33) for p_2 in the form of the superposition of terms at frequencies 0, $\pm\omega$, and $\pm 2\omega$ respectively:

$$p_2 = AP_{21}(x) e^{i\omega t} + A^2 P_{22}(x) e^{2i\omega t} + A^* AP_{20}(x) + \text{c.c.} \quad (3.39)$$

Here, the asterisk denotes the complex conjugate. The equations for $P_{21}(x)$, $P_{22}(x)$, and $P_{20}(x)$ are obtained from Eq. (3.33) upon separating the different frequency components in the right-hand side. However P_{20} is more easily determined from the momentum equation (2.53). The explicit form of these equations is given in Eqs. (B7) to (B9) in Appendix B of Karpov & Prosperetti (2000).

3.4 The Landau Equation

The procedure demonstrated in the previous section can be continued to order ϵ^4 to find an evolution equation for the amplitude A of the well-known Landau form. We write this equation in terms of the unscaled amplitude $\tilde{A} = \epsilon A \exp(i\omega t)$:

$$\frac{d\tilde{A}}{dt} = i \left[\left(\omega + \tilde{\Omega}_1 + \tilde{\Omega}_2 + \tilde{\Omega}_3 \right) + \left(\tilde{\Lambda}_2 + \tilde{\Lambda}_3 \right) |\tilde{A}|^2 \right] \tilde{A}, \quad (3.40)$$

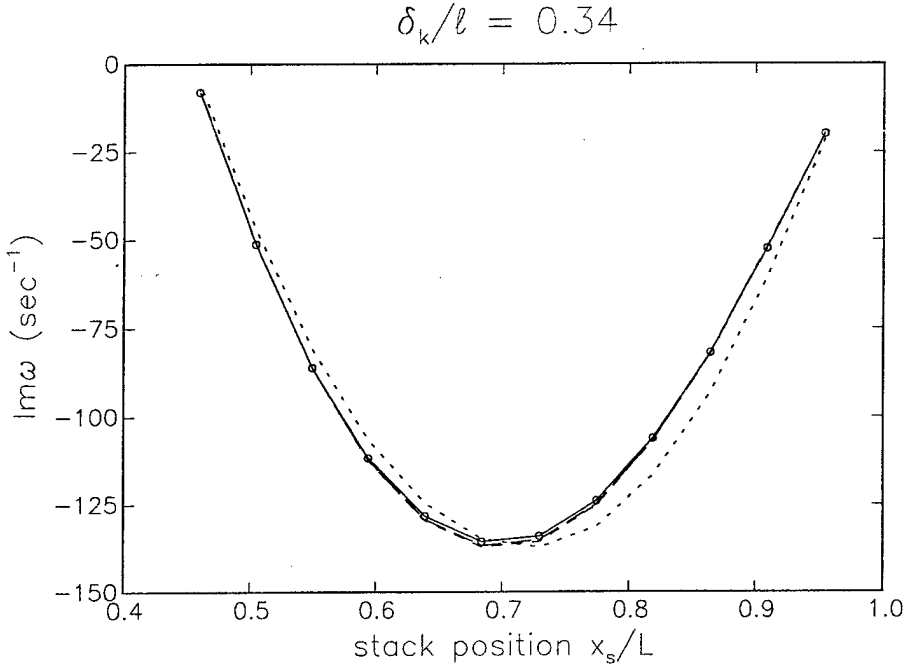


Figure 3.1: Negative of the instability growth rate, i.e. imaginary part of the exact linear eigenfrequency (solid line), compared with the successive approximations $\text{Im}\tilde{\Omega}_1$ (dotted line), $\text{Im}(\tilde{\Omega}_1 + \tilde{\Omega}_2)$ (short dashes), and $\text{Im}(\tilde{\Omega}_1 + \tilde{\Omega}_2 + \tilde{\Omega}_3)$ (long dashes) as functions of the normalized position x_s/L of the stack for the geometry described in the text.

where $\tilde{\Omega}_1$ is obtained by multiplying (3.37) by ϵ ,

$$\begin{aligned} \tilde{\Omega}_1 &= -\frac{1}{2Vp_0^2\omega} \int_0^L dx S \left[c_0^2 \left(\frac{f_V}{1-f_V} + \frac{\rho_{10}}{\rho_0} \right) \left(\frac{dP_1}{dx} \right)^2 \right. \\ &\quad \left. + (\gamma-1)\omega^2 f_K P_1^2 + \frac{(\gamma-1)(f_V-f_K)}{(1-\sigma)(1-f_V)} c_p G_0 P_1 \frac{dP_1}{dx} \right], \end{aligned} \quad (3.41)$$

with similar expressions for $\tilde{\Omega}_k = \epsilon^k \Omega_k$; the A 's are also integrals over the volume of the thermoacoustic device and are given explicitly in Karpov & Prosperetti (2000).

Equation (3.40) contains both linear and nonlinear contributions that it is better to discuss separately. In all the numerical examples that follow we use as reference case the geometry of the experiment of Atchley et al. (1990), the implementation of which in the context of the present mathematical model is described in detail in an earlier paper (Yuan et al. 1997). Briefly, the system consists of a 38.2 mm-diameter tube with a length of 99.89 cm, a 35 mm-long stack of stainless steel plates located 87.95 cm from the cold end, and two heat exchangers. The operating pressure was $p_0 = 307$ kPa.

3.4.1 Linear regime

In the linear approximation, Eq. (3.40) is

$$\frac{d\tilde{A}}{dt} = i(\omega + \tilde{\Omega}_1 + \tilde{\Omega}_2 + \tilde{\Omega}_3) \tilde{A}. \quad (3.42)$$

In addition to giving the growth rate of the perturbation for a given temperature distribution T_w , Eq. (3.42) can be used to determine onset conditions by adjusting the temperature distribution in such a way that $\text{Im}(\tilde{\Omega}_1 + \tilde{\Omega}_2 + \tilde{\Omega}_3) = 0$.

We have shown (Karpov & Prosperetti 1998) that, retaining just the first term $\tilde{\Omega}_1$, the critical temperature gradient found in this way is already in excellent agreement with Rott's exact linear theory prediction. A typical example is shown in Fig. 3.1, where the imaginary part of the exact linear eigenfrequency – i.e. minus the growth rate of the instability – (solid line) is compared with the successive approximations $\text{Im } \tilde{\Omega}_1$ (dotted), $\text{Im } (\tilde{\Omega}_1 + \tilde{\Omega}_2)$ (dashed), and $\text{Im } (\tilde{\Omega}_1 + \tilde{\Omega}_2 + \tilde{\Omega}_3)$ (long dashes). Here the horizontal axis is the normalized position x_S/L of the cold end of the stack. Further results of this type will be found in Karpov & Prosperetti (1998).

Results such as these confirm the correctness of the perturbation technique and the accuracy of the analysis.

We now turn to the more interesting nonlinear case.

3.4.2 Nonlinear regime

Equation (3.40), and its complex conjugate, predict the evolution of the oscillation amplitude in time. These equations can be combined to find

$$\frac{d|\tilde{A}|^2}{dt} = -2 \left[\text{Im } \tilde{\Omega}_3 + \text{Im } \tilde{\Lambda}_3 |\tilde{A}|^2 \right] |\tilde{A}|^2, \quad (3.43)$$

which is readily solved with the result

$$|\tilde{A}|^2 = \frac{|\tilde{A}|_{sat}^2}{1 + \exp(2\tilde{\Omega}_{3i}\hat{t}) \left(|\tilde{A}|_{sat}^2 / |\tilde{A}_0|^2 - 1 \right)}, \quad (3.44)$$

where \tilde{A}_0 denotes the initial value of the amplitude and

$$|\tilde{A}|_{sat}^2 = -\frac{\text{Im } \tilde{\Omega}_3}{\text{Im } \tilde{\Lambda}_3} = -\frac{\tilde{\Omega}_{3i}}{\tilde{\Lambda}_{3i}}. \quad (3.45)$$

Since $\tilde{\Omega}_{3i} < 0$ for an unstable system, this equation shows that, for $\hat{t} \rightarrow \infty$, $|\tilde{A}|^2$ is asymptotic to the saturation value $|\tilde{A}|_{sat}^2$, as also follows directly from the right-hand side of (3.40) since only Ω_3 and Λ_3 have non-zero imaginary parts. In the stable case, $\tilde{\Omega}_{3i}$ is positive and the amplitude decays to zero.

Figure 3.2 shows the time dependence of the cold-end pressure for the middle-temperature case $\Delta T = 346$ K of Atchley et al. (1990) and exhibits the typical saturation of the instability due to non-linear effects.

The result (3.45) for the asymptotic saturation amplitude is of particular interest as it contains the effect of a large number of variables such as the deviation of the temperature distribution from onset conditions, the shape of the resonator, the effect of stack geometry (through the values of the exchange parameters $f_{V,K}$) and stack length, Prandtl number, and others.

We assume a linear temperature variation between a cold temperature T_C and a hot temperature T_H in the stack, and constant temperatures equal to T_C and T_H at the left and right of the stack, respectively.

The solid line in Fig. 2 is the (positive) peak amplitude as a function of the temperature difference along the stack for the experimental situation of Atchley et al. (1990). The dotted line shows $|\tilde{A}_{sat}|$.³ For this case our calculations indicate an onset temperature of 573.5 K which, with $T_C = 293$ K, corresponds to an onset temperature gradient of 8.01 K/mm. One recognizes here the typical structure of a supercritical bifurcation. In this figure the symbols represent the three data points reported by Atchley et al. (1990). In order to reconcile these data with our theoretical prediction, one would have to assume hot-end temperatures 36, 22, and 20 K lower than the reported values. We found a similar effect in our earlier numerical study (Yuan et al. 1997). Two possible concurrent explanations come to mind. The first one is the temperature jump that is established between the ends of the stack and the heat exchangers, which has the effect of reducing the temperature gradient in the stack (Brewster et al. 1997). Secondly, the temperature values reported in

³Since the pressure perturbation is the sum of two complex conjugate quantities, the dotted line actually shows $2 |\text{Re } \tilde{A}_{sat}|$.

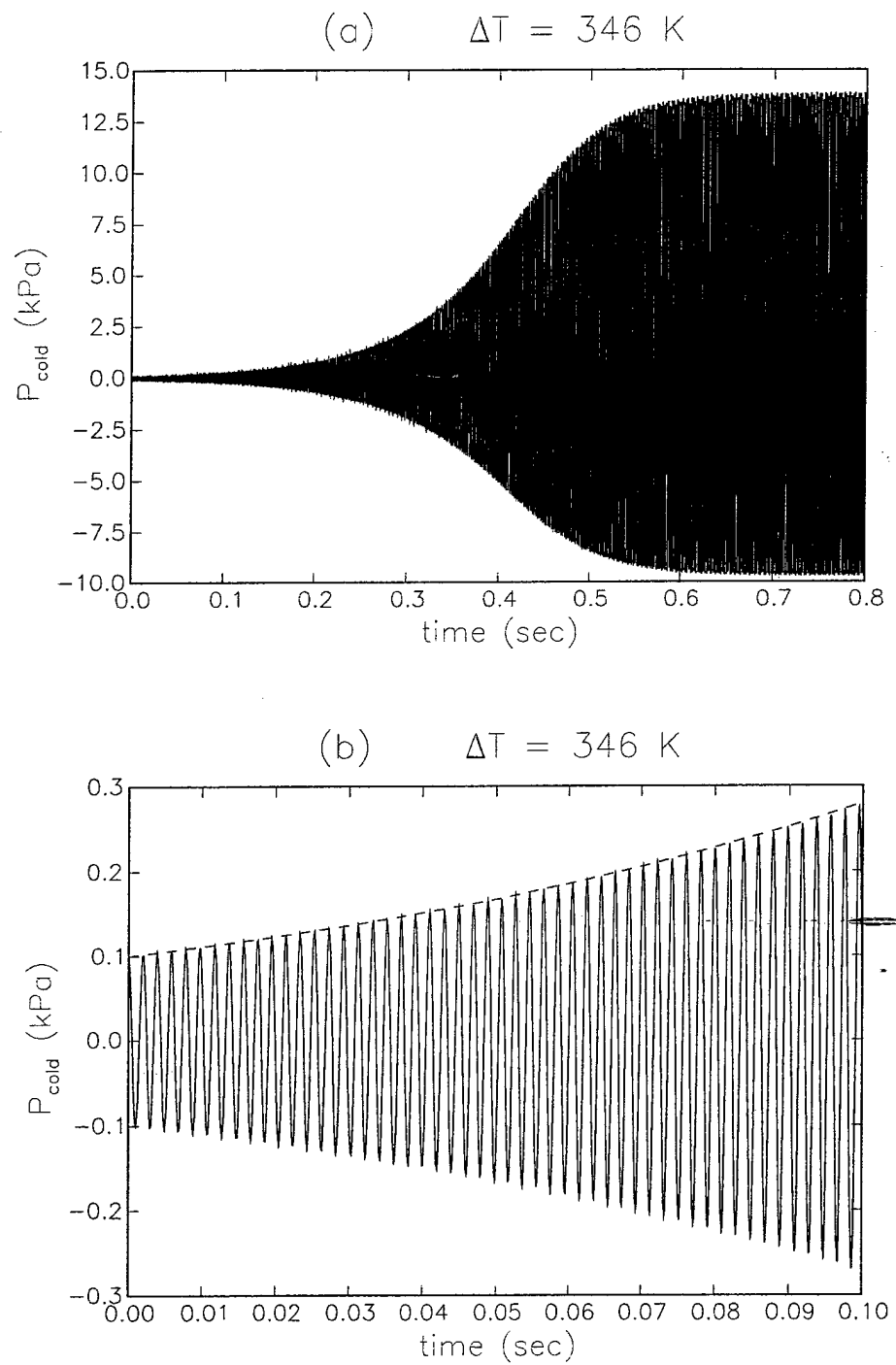


Figure 3.2: Time dependence of the cold-end pressure for the middle-temperature case $\Delta T = 346$ K of Atchley et al. (1990b) as predicted by Eq. (3.11) with each term computed using the A given by (3.40). The lower figure is an enlargement of the initial phase of the upper one; the dashed line is the envelope from (3.44).

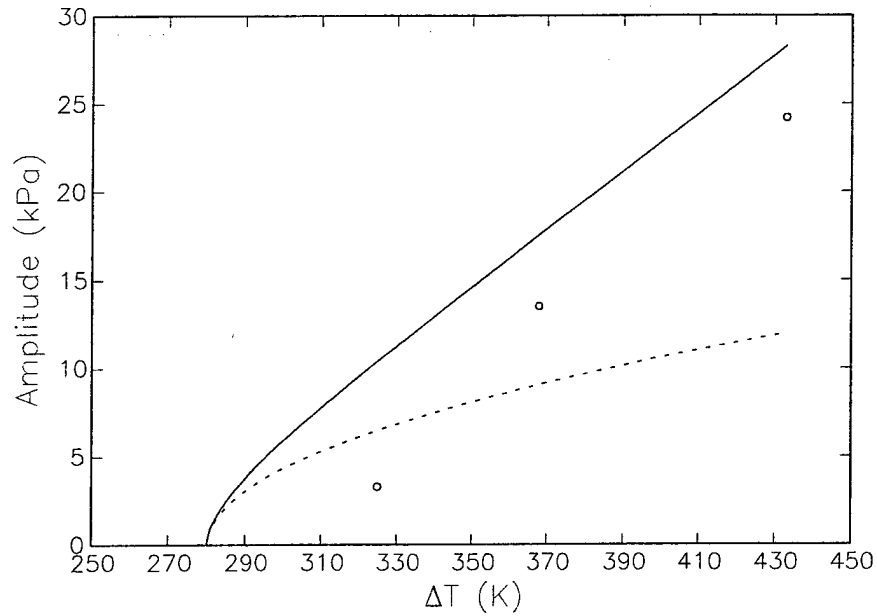


Figure 3.3: The solid line shows the peak amplitude of the pressure perturbation at the cold end of the resonant tube as a function of the temperature difference ΔT along the stack; the dashed line is the saturation amplitude of the fundamental mode $|\tilde{A}|_{sat}$ from Eq. (3.45); the symbols are the data points reported by Atchley et al. (1990b).

Atchley et al. were measured at the surface of the tube, rather than in the stack. As mentioned in Yuan et al. (1997), for the conditions of the experiment one may reasonably expect a temperature difference of this order between these two positions. In addition, the experimental setup will most likely include several losses (e.g. due to the lack of alignment between the heat exchanger and stack plates, which causes an increase of the effective blockage of the tube, heat conduction in the gas, and others) that are not included in our model. Hence the difference with the data is in the expected direction and of a reasonable magnitude. The discrepancy at the lowest temperature difference is somewhat larger but, on the other hand, it is here that the effect of losses would be greatest.

The expressions derived before contain a dependence on many variables the effect of which can also be studied. Several examples are given in Karpov & Prosperetti (2000).

3.5 Conclusions

We have presented a time-dependent weakly nonlinear theory of the build-up of unstable oscillations in a thermoacoustic prime mover. The expressions we have derived simulate the initial growth of the instability as well as its subsequent saturation. The results are in reasonable agreement with the limited number of experimental observations reported in the literature for the configuration that we can model.

For all the examples that we have discussed, a solution of Rott's equation shows that the imaginary part of all the modes higher than the fundamental one is positive, so that they are all stable. Therefore, the second and higher harmonic amplitudes are non-zero only due to non-linear energy transfers from the fundamental. In the present perturbation scheme, energy transfer to the second mode starts occurring at the second order. However, the energy loss of this mode due to the coupling with the solid structure only

arises at the fourth order. Since the amplitude of the fundamental saturates at a level such that the energy transferred to the second mode can be dissipated by the mechanisms affecting this mode, in order to find the saturation amplitude of the fundamental, we had to carry the expansion to this order. The fact that the perturbation method only includes a small number of modes prevents energy transfer from the fundamental to the higher modes. As a consequence, our results tend to overestimate somewhat the saturation amplitude. Nevertheless, the comparison of section 5 shows that there is a parameter region where the error is acceptable.

Even if our results may not be sufficiently precise in absolute terms when the temperature gradient is too far from the onset value, they are still useful for comparative purposes as they indicate trends of the system performance when design parameters or operating conditions are varied. For example, we find a very strong effect of cross-sectional area variations. Since the expressions we have derived contain a great amount of detail on the geometry and other characteristics of the system, similar sensitivity studies with respect to other parameter variations are possible.

In spite of the algebraic complexity of the final form of the results, the present solution is certainly much easier to evaluate than carrying out a full-fledged multi-dimensional *ab initio* numerical calculation. In our earlier paper (Karpov & Prosperetti 1998) it was possible to simplify the form of the solution by using the short stack approximation. Here this approximation is not very useful because the result depends on auxiliary fields such as P_{21} , P_{22} , etc. the determination of which requires the solution of equations which can only be solved in special cases. Nevertheless it might be possible to develop some comparable approximation.

References

- Atchley, A.A., 1994, Analysis of the initial build-up of oscillations in a thermoacoustic prime mover, *J. Acoust. Soc. Am.*, **95**, 1661–1664.
- Atchley, A.A., Bass, H.E., & Hofler, T.J., 1990, Development of nonlinear waves in a thermoacoustic prime mover, in *Frontiers in Nonlinear Acoustics*, Hamilton, M.F. & Blackstock, D.T., eds., Elsevier, 603–608.
- Brewster, J.R., Raspet, R., & Bass, H.E., 1997, Temperature discontinuities between elements of thermoacoustic devices, *J. Acoust. Soc. Am.*, **102**, 3355–3360.
- Hinch, E.J., 1991, *Perturbation Methods*, Cambridge U.P., Cambridge.
- Karpov, S. & Prosperetti, A., 1998, Linear thermoacoustic instability in the time domain, *J. Acoust. Soc. Am.*, **103**, 3309–3317.
- Karpov, S. & Prosperetti, A., 2000, Nonlinear saturation of the thermoacoustic instability, *J. Acoust. Soc. Am.*, **107**, 3130–3147.
- Kevorkian, J. & Cole, J.D., 1996, *Perturbation Methods in Applied Mathematics*, Springer, New York, 2nd ed.
- Morse, P.M. & Feshbach, H., 1953, *Methods of Theoretical Physics*, McGraw-Hill, New York.
- Murdock, J.A., 1991, *Perturbations*, Wiley, New York.
- Naylor, A.W. & Sell, G.R., 1982, *Linear Operator Theory in Engineering and Science*, Springer, New York, 2nd ed.
- Wheatley, J., Intrinsically irreversible or natural heat engines, in *Frontiers in Physical Acoustics*, Sette, D., ed., North-Holland, 1986, 35–475.

Chapter 4

Bubble Screens

During the last few months of the ONR grant, we have also worked on a subject unrelated to thermoacoustics, but, nevertheless of interest to ONR, namely the propagation of pressure waves through layers of bubbly liquid, both with the purpose of attenuating the wave and to generate low-frequency sound by efficient parametric amplification. Since this topic is outside the focus of interest of the rest of this final report, we will only give a concise presentation. Details are available in a paper submitted to *J. Acoust. Soc. Am.*.

A schematic representation of the situation considered here is shown in Fig. 4.1: a one-dimensional layer of liquid containing gas bubbles is located between $x = 0$ and $x = L$ and is excited by a plane wave normally incident from the left. As a result of this excitation, a reflected wave at the left of the layer and a transmitted wave at the right are generated.

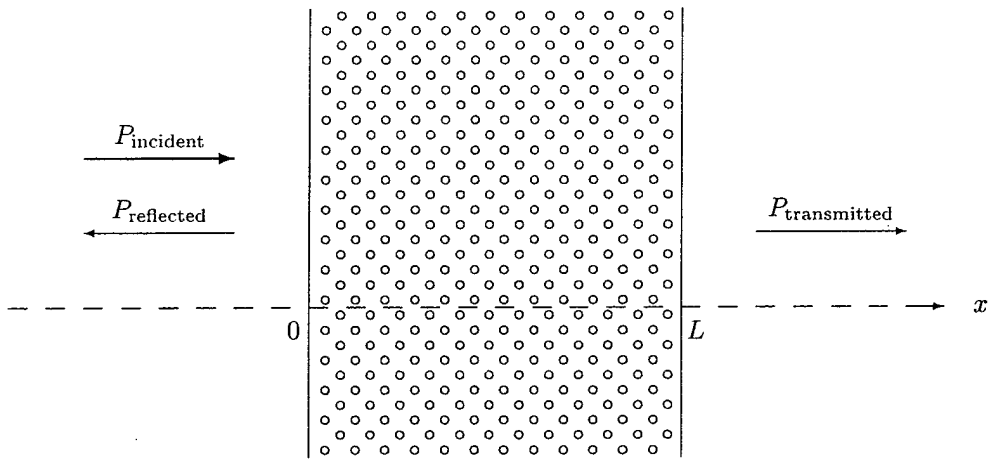


Figure 4.1: Schematic representation of the one-dimensional bubble layer excited by a normally incident plane wave from the left.

4.1 Mathematical model

The mathematical model of the bubbly liquid consists of the continuity equation

$$\frac{1}{\rho_l c_l^2} \frac{\partial P}{\partial t} + \frac{\partial u}{\partial x} = \frac{\partial \beta}{\partial t}, \quad (4.1)$$

in which ρ_l and c_l are the density and sound speed of the pure liquid and P , u the average mixture pressure and velocity, and of the momentum equation

$$\rho_l \frac{\partial u}{\partial t} + \frac{\partial P}{\partial x} = 0. \quad (4.2)$$

This model is essentially that of Kogarko (1964) and van Wijngaarden (1968) except that, as pointed out by Caflisch et al. (1985), the convective term of the material derivative can be omitted due to the assumed smallness of the gas volume fraction β ; additional considerations on this point are given in Watanabe & Prosperetti (1994), and further applications of this and similar models can be found e.g. in Zabolotskaya (1977), Kuznetsov et al. (1978), Gasenko et al. (1979), Nigmatulin (1991), Akhatov et al. (1994), Naugolnykh & Ostrovsky (1998), Colonius et al. (2000), and many others. Buoyancy effects are neglected in (4.2) due to the smallness of the acoustic time scale compared with the time evolution of the bubble layer. The volume fraction is given by

$$\beta(x, t) = \frac{4}{3} \pi R^3(x, t) n \quad (4.3)$$

where $R(x, t)$ is the instantaneous radius of the bubbles contained in a small volume centered around x and n is the bubble number density. In the same assumption $\beta \ll 1$ under which (4.1) and (4.2) hold, the bubble number density n can be taken as independent of time; for simplicity, we further assume it to be spatially uniform and we also assume that, at equilibrium, all the bubbles have the same radius.

In spite of its appearance, the previous model retains a strong nonlinearity in the manner in which R is calculated. Again on the basis of the smallness of β , for this purpose we use the Rayleigh-Plesset equation of bubble dynamics (see e.g. Plesset & Prosperetti 1977; Prosperetti 1991; Feng & Leal 1997)

$$R \frac{\partial^2 R}{\partial t^2} + \frac{3}{2} \left(\frac{\partial R}{\partial t} \right)^2 = \frac{1}{\rho_l} \left(p - P - \frac{2\sigma}{R} - \frac{4\mu}{R} \frac{\partial R}{\partial t} \right). \quad (4.4)$$

Here p is the bubble internal pressure (approximated by the gas pressure, the small vapor contribution being neglected), σ the surface tension coefficient, and μ the liquid viscosity. For an isolated bubble, the ambient pressure P appearing in (4.4) is to be identified with the pressure at the location of the bubble if the bubble were absent. In a dilute mixture the bubbles are subject to the averaged field and P should be taken as the average pressure appearing in the momentum equation (4.2) (see e.g. Caflisch et al. 1985; Zhang & Prosperetti 1994). As before, in (4.4) we omit the convective term of the material derivatives of R .

In order to close the system a relationship between the gas pressure p and bubble radius R is needed. This point has been treated at length in earlier papers (Prosperetti 1991; Watanabe & Prosperetti 1994). Suffice it to say that we approximate the gas pressure inside each bubble as spatially uniform, which leads to

$$\frac{\partial p}{\partial t} = \frac{3}{R} \left[(\gamma - 1) k \frac{\partial T}{\partial r} \Big|_R - \gamma p \frac{\partial R}{\partial t} \right], \quad (4.5)$$

where T is the local gas temperature to be found from

$$\frac{\gamma}{\gamma - 1} \frac{p}{T} \left(\frac{\partial T}{\partial t} + v \frac{\partial T}{\partial r} \right) = \dot{p} + \frac{1}{r^2} \frac{\partial}{\partial r} \left(k r^2 \frac{\partial T}{\partial r} \right), \quad (4.6)$$

with

$$v = \frac{1}{\gamma p} \left[(\gamma - 1) k \frac{\partial T}{\partial r} - \frac{1}{3} r \dot{p} \right]. \quad (4.7)$$

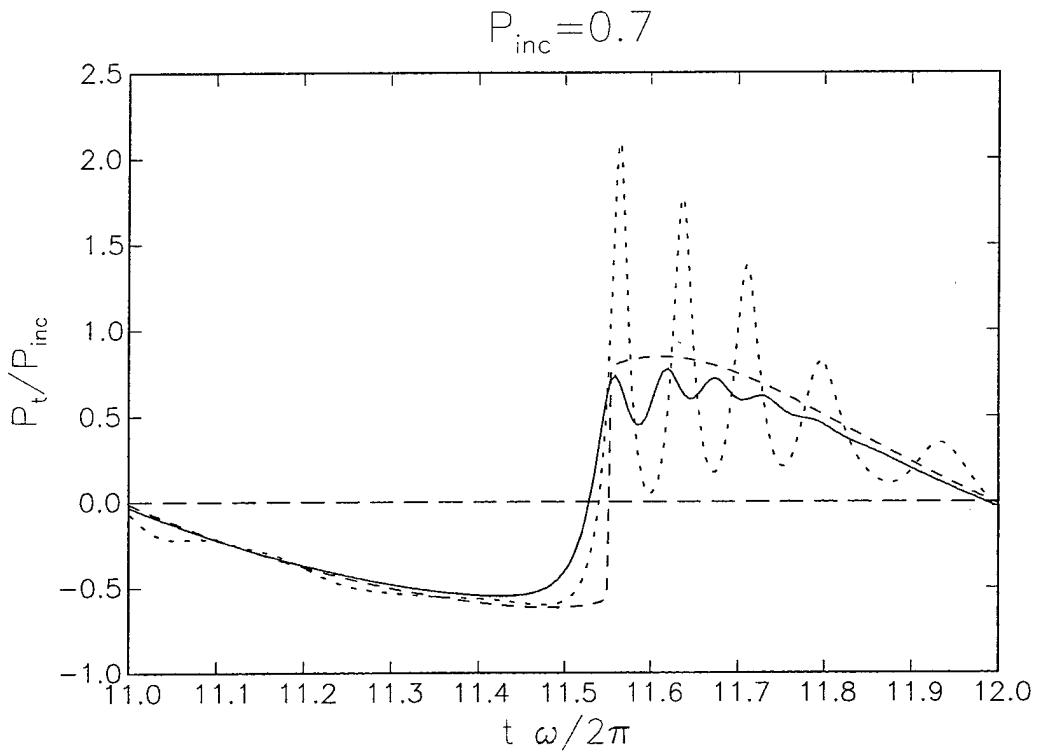
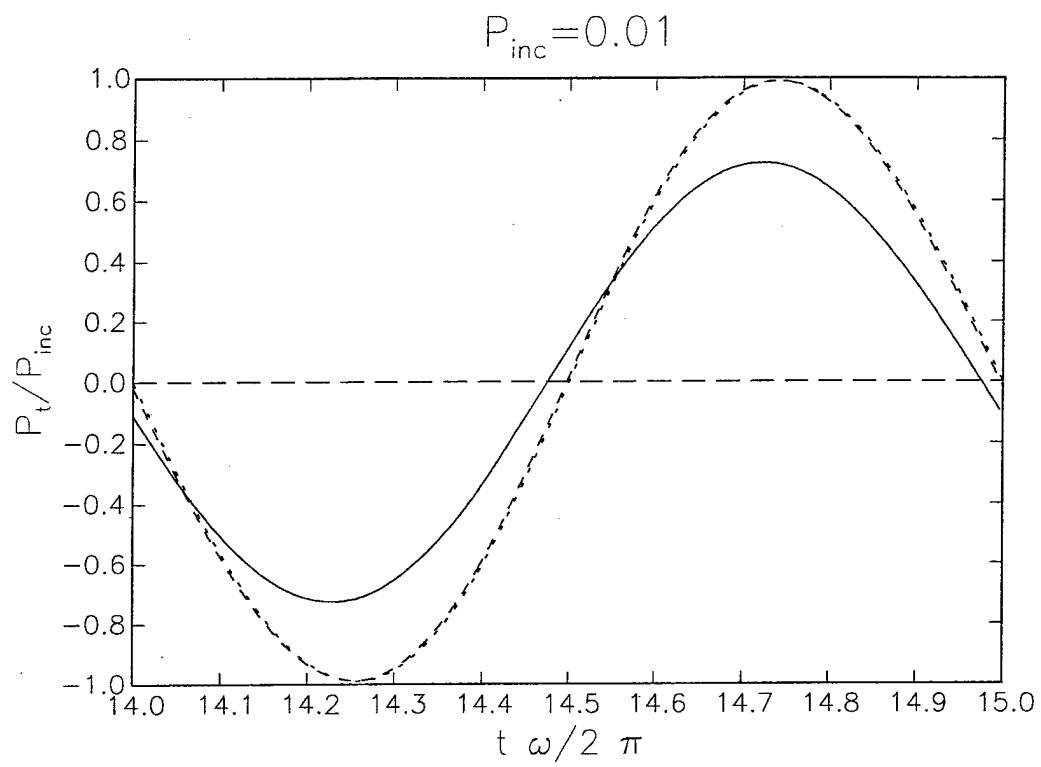


Figure 4.2: Steady state shape of the transmitted wave according to the complete model (solid line), compared with polytropic (dotted line) and quasi-equilibrium (dashed line) models with $\kappa_p = 1$; upper panel $P_{\text{inc}}/P_\infty = 0.01$, lower panel $P_{\text{inc}}/P_\infty = 0.7$; $\omega/2\pi = 1.347$ kHz, $\beta_0 = 0.133\%$, $R_0 = 0.121$ mm.

In these equations γ and $k = k(T)$ are the ratio of specific heats and thermal conductivity of the gas and r is the radial coordinate measured from the center of the bubble. As shown in Kamath et al. (1993), at the surface of the bubble, a suitable boundary condition for (4.6) is

$$T(R, t) = T_\infty, \quad (4.8)$$

where T_∞ is the undisturbed liquid temperature. It should be noted that, inside the bubble centered at x , the temperature field T depends on r as well as t and hence, in principle, the set of equations (4.5) to (4.7) must be solved at all spatial location in the layer.

The model described in this section is supplemented by the conditions of continuity of pressure and velocity across the planes delimiting the bubbly layer.

In addition to the model just described, in this work we consider also two simpler versions, one in which the internal pressure is given by a polytropic relation

$$p = p_0 \left(\frac{R_0}{R} \right)^{3\kappa_p}, \quad (4.9)$$

and one in which the same relation is used, but the left-hand side of the Rayleigh-Plesset equation, describing the effect of the liquid inertia on the radial motion of the bubbles, is set to zero. We refer to these two simplified models as to the *polytropic* and *quasi-equilibrium* model, respectively.

The model equations are solved numerically by a total-variation-diminishing method similar to the one described in Chapter 1.

4.2 Results

Figure 4.2 shows the transmitted wave at steady state normalized by the amplitude of the incident wave as a function of the dimensionless time $t\omega/2\pi$ for two incident amplitudes, $P_{inc}/P_\infty = 0.01$ (upper panel) and $P_{inc}/P_\infty = 0.7$ (lower panel). The solid lines are the results of the complete model outlined in the previous section. The dotted and dashed lines are the results for the polytropic and quasi-equilibrium models with $\kappa_p = 1$, respectively. When the incident amplitude is small (upper panel) the polytropic and quasi-equilibrium models give essentially the same result, which is expected in this case in which the incident frequency is much smaller than the bubble resonance frequency. The complete model predicts a somewhat smaller amplitude and a small phase shift, both due to the inclusion of thermal dissipation in the bubble motion, but behaves otherwise very similarly.

For the larger-amplitude excitation (lower panel of Fig. 4.2) all three models predict shock formation, but the differences among them are more pronounced. The complete model (solid line) shows a transmitted wave with slight oscillations near the maximum, while these oscillations are highly exaggerated by the polytropic model (dotted line). The same qualitative difference is encountered when the two models are applied to shock waves in bubbly liquids (Watanabe & Prosperetti 1994). Since these oscillations are a consequence of bubble inertia, their absence in the quasi-equilibrium model (dashed line) is not surprising. The reason why this feature is encountered at this higher amplitude but not at the lower amplitude of the upper panel of Fig. 4.2 is that the formation of the shock introduces a much shorter characteristic time scale in the wave, which is not too far from the resonant period of the bubbles. Due to the absence of thermal effects, the polytropic model is less dissipative than the complete one, and the shock time scale is accordingly shorter: the smaller damping and the shorter time scale combine to cause the prominent oscillations of this result. If these oscillations are averaged out in the mind's eye, one sees a substantial similarity among the different profiles which is due to the fact that the underlying, relatively slowly-varying, wave structure is only slightly damped in all models. In any event, it may be noted that the high-frequency oscillations of the complete model are so strongly damped that the quasi-equilibrium model ends up being a better approximation to the actual behavior than the polytropic model.

Figure 4.3 shows the components of the transmitted (upper panel) and reflected (lower panel) waves at the incident frequency for $P_{inc}/P_\infty = 0.05$ (circles) and $P_{inc}/P_\infty = 0.7$ (squares) according to the complete

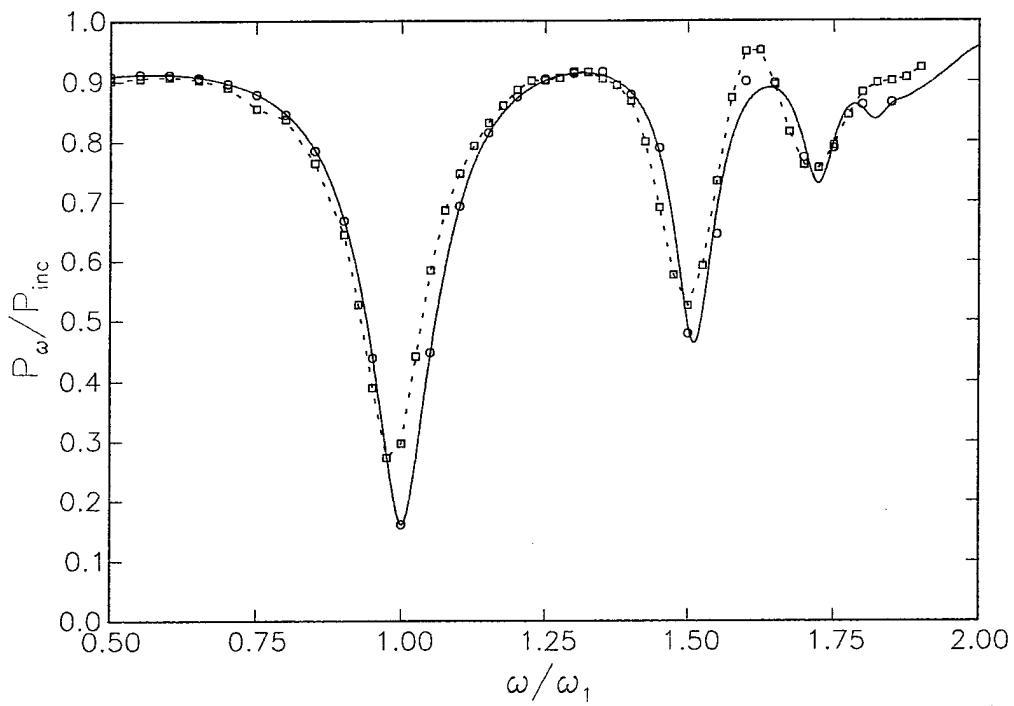
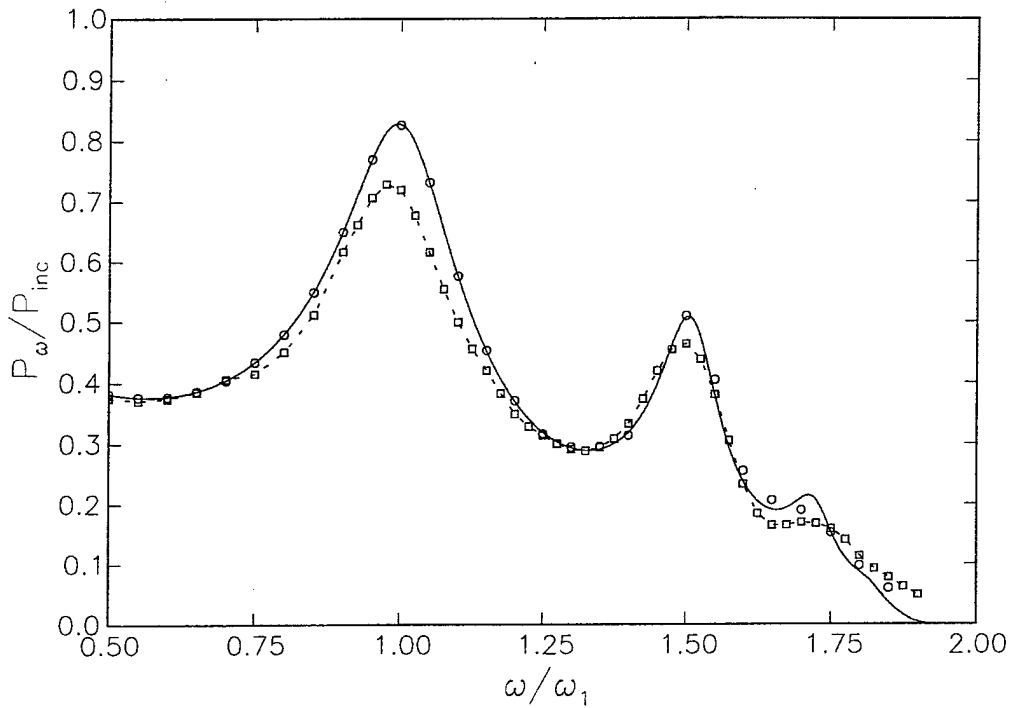


Figure 4.3: Pressure amplitudes of the component at the incident wave frequency ω for the transmitted (upper panel) and reflected (lower panel) waves as functions of the incident frequency ω normalized by the first quasi-equilibrium linear eigenfrequency of the layer, $\omega_1/2\pi = 1.347$ kHz. The circles and squares are the numerical results of the complete model for amplitudes $P_{inc}/P_\infty = 0.05$ and $P_{inc}/P_\infty = 0.7$ respectively. The solid curves are the linear results. The dotted lines connecting squares are only guides to the eye. The bubble radius is 1.21 mm.

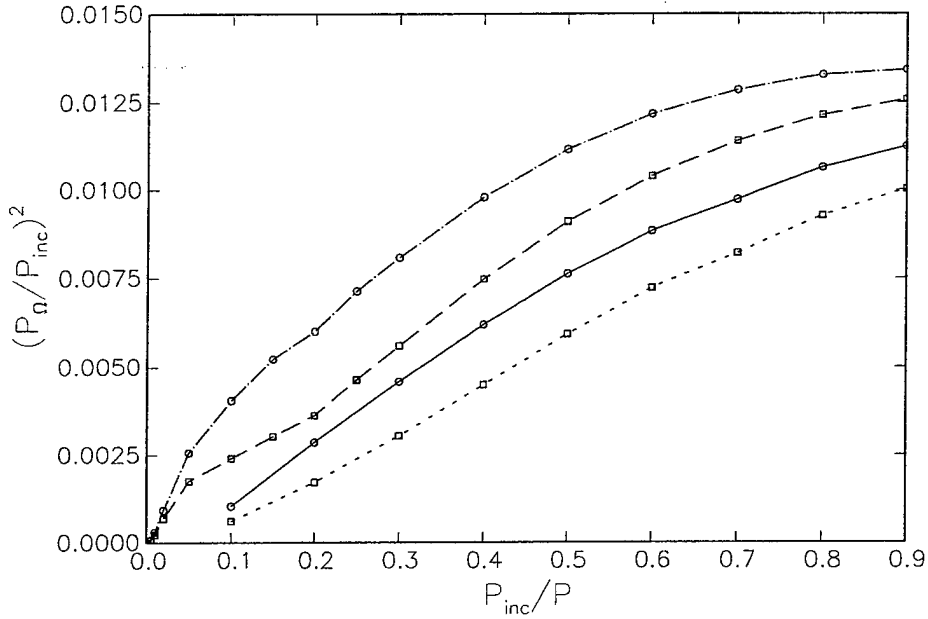


Figure 4.4: Relative power of the low-frequency component in the transmitted (circles) and reflected (squares) waves for dual-frequency excitation as a function of the amplitude P_{inc}/P_∞ of the incident wave components for $\omega^{(1)} = 9\omega_1 = 2\pi \times 3.03$ kHz, $\omega^{(2)} = 10\omega_1 = 2\pi \times 3.37$ kHz (P_∞ is the undisturbed ambient pressure). The lines are only guides to the eye. The solid and dotted lines are for the complete model while the dot-dash and dashed lines are for the quasi-equilibrium model with $\kappa_p = 1$. The bubble radius is $50 \mu\text{m}$.

model as functions of the normalized incident frequency ω/ω_1 , with $\omega_1/2\pi = 1.347$ kHz as before; the dotted lines connect the symbols as an aid to the eye. The solid line shows analytic results obtained from a linearization of the governing equations and is in excellent agreement with the numerical results for the lower-amplitude case. Remarkably, when normalized by the incident pressure as here, the higher-amplitude results are only slightly different, with somewhat less pronounced maxima and minima and a slight shift to lower frequencies.

Another interesting case is that in which the incident wave contains two frequencies:

$$P_{inc} = A [\cos \omega^{(1)}(x/c - t) + \cos \omega^{(2)}(x/c - t)] , \quad (4.10)$$

where c is the speed of sound in the liquid. In particular, since the eigenfrequencies of the normal modes of a layer such as the one considered here are all multiples of the lowest eigenfrequency, one can take $\omega^{(1)}$ and $\omega^{(2)}$ to correspond to eigenmodes and, in addition, their difference $\omega^{(2)} - \omega^{(1)}$ also to coincide with an eigenmode. It may be expected that, in this way, there would be a very efficient parametric effect. In the example that follows we take $\omega^{(1)}$ and $\omega^{(2)}$ equal to the 9th and 10th eigenfrequencies, so that their difference coincides with the fundamental.

Figure 4.4 shows the relative power of the low-frequency signal $(P_\Omega/P_{inc})^2$ of the transmitted (circles) and reflected (squares) waves as a function of the amplitude of the incident wave components P_{inc}/P_∞ when $\omega^{(1)} = 9\omega_1$ and $\omega^{(2)} = 10\omega_1$; the solid and dotted lines are for the complete model while the dot-dash and dashed lines are for the quasi-equilibrium model. Here the bubble radius is $R_0 = 50 \mu\text{m}$, with a linear resonance frequency $\omega_0/2\pi = 55.86$ kHz and $\kappa_p = 1.01$. It can be seen here that the efficiency of conversion is about 1%, which is a very high value.

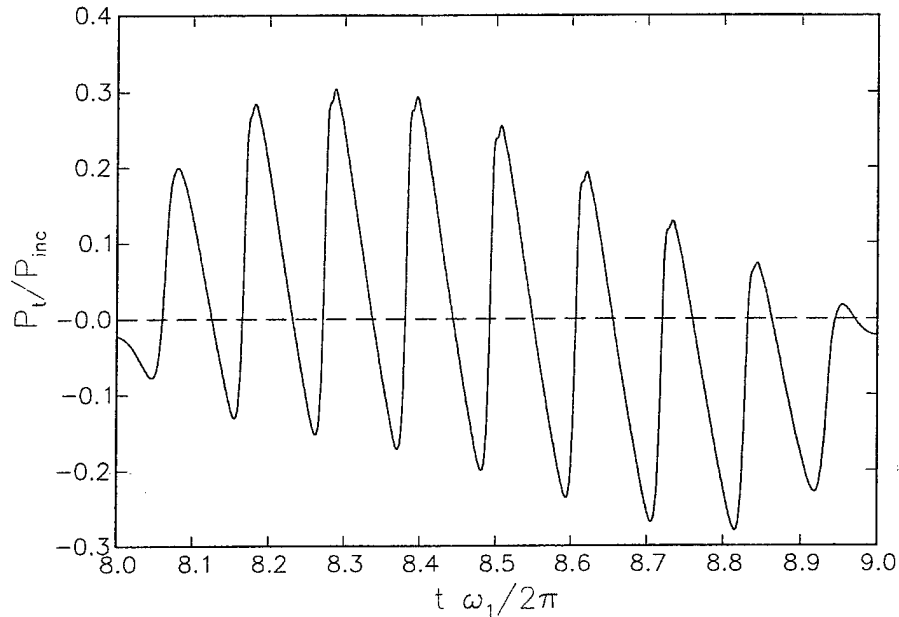


Figure 4.5: Steady state shape of transmitted wave produced by the complete model at time $t = 8 \times 2\pi/\omega_1$ for dual-frequency excitation with $\omega^{(1)} = 9\omega_1 = 2\pi \times 3.03$ kHz, $\omega^{(2)} = 10\omega_1 = 2\pi \times 3.37$ kHz and amplitude $P_{inc}/P_\infty = 0.5$.

Figure 4.5 shows the steady state temporal transmitted waveform at time $t = 8 \times 2\pi/\omega_1$ for $\omega^{(1)} = 9\omega_1$, $\omega^{(2)} = 10\omega_1$, $P_{inc}/P_\infty = 0.5$, for 50 μm -radius bubbles. The transmitted wave has a sawtooth appearance, but the peaks are not very sharp, which is evidence of the stronger damping affecting the higher frequencies. The relative power of the difference-frequency harmonic in the transmitted wave in this example is 7.6×10^{-3} .

4.3 Conclusions

The results summarized here correct and expand the scope of the earlier ones of Druzhinin et al. (1996). In comparison with that work, we have used a more realistic description of the bubble behavior which includes the effects of radial inertia, with the associated dispersion, and of the gas thermal behavior, with the attendant energy losses. As expected, several details of the predictions of the earlier model are modified by these effects, although the basic character remains. Thus, we find a propensity for shock-wave generation in the bubbly layer which gives rise to a transmitted wave with a sawtooth character.

We have also studied the possibility of enhanced low-frequency difference-wave generation through the exploitation of the resonances of the bubbly layer. We have concluded that a difference-wave power of the order of 1% of the incident power can be generated using incident wave amplitudes of less than 100 kPa. Thus, this technique for the parametric generation of low-frequency waves may have practical value.

An important aspect of the phenomenon, confirmed by this study, is that operation near the resonance frequency of the individual bubbles is detrimental to the energy conversion efficiency due to the strong dissipation of the bubble motion in this frequency range.

In order to avoid the practical difficulties connected with the generation and control of suitable bubbles, it might be expedient to apply the principle described in this paper to other systems. For example, one would expect similar phenomena to occur in porous water-like (or rubber-like) media in which the shear modulus is small and plays the role of gas compressibility in bubbles; some experiments of this type are reported in Belyaeva & Timanin (1991). Like bubbles, pores in such media provide very strong nonlinearity

(see, e.g. Naugolnykh & Ostrovsky 1998 section 1.4). At the same time, it is much easier to have small and almost equal-size pores, the system is more stable, and losses are typically smaller.

References

- Akhatov, I., Parlitz, U., & Lauterborn, W., 1994, Pattern formation in acoustic cavitation, *J. Acoust. Soc. Am.*, **96**, 3627–3635.
- Belyaeva, I. & Timanin, E., 1991, Experimental investigation of nonlinear propagation in porous elastic media, *Sov. Phys. Acoust.*, **37**, 1026–1029.
- Caffisch, R.E., Miksis, M.J., Papanicolaou, G., & Ting, L., 1985, Effective equations for wave propagation in bubbly liquids, *J. Fluid Mech.*, **153**, 259–273.
- Colonius, T., d'Auria, F., & Brennen, C.E., 2000, Acoustic saturation in bubbly cavitating flow adjacent to an oscillating wall, *Phys. Fluids*, **12**, 2752–2761.
- Feng, Z.C. & Leal, L.G., 1997, Nonlinear bubble dynamics, *Ann. Rev. Fluid Mech.*, **29**, 201–243.
- Gasenko, V.G., Nakoryakov, V.E., & Shreiber, I.R., 1979, Nonlinear disturbances in a liquid containing gas bubbles, *Sov. Phys. Acoust.*, **25**, 385–388.
- Kamath, V., Prosperetti, A., & Egolfopoulos, F., 1993, A theoretical study of sonoluminescence, *J. Acoust. Soc. Am.*, **94**, 248–260.
- Kogarko, B.S., 1964, One-dimensional unsteady motion of a liquid with an initiation and progression of cavitation, *Dokl. Akad. Nauk SSSR*, **155**, 779–782. (in Russian).
- Kuznetsov, V.V., Nakoryakov, V.E., Pokusaev, G., & Shreiber, I.R., 1978, Propagation of perturbations in a gas-liquid mixture, *J. Fluid Mech.*, **85**, 85–96.
- Naugolnykh, K. & Ostrovsky, L., 1998, *Nonlinear Wave Processes in Acoustics*, Cambridge U.P., Cambridge U.K.
- Nigmatulin, R.I., 1991, *Dynamics of Multiphase Media*, Hemisphere, Washington.
- Plesset, M.S. & Prosperetti, A., 1977, Bubble dynamics and cavitation, *Ann. Rev. Fluid Mech.*, **9**, 145–185.
- Prosperetti, A., 1991, The thermal behaviour of oscillating gas bubbles, *J. Fluid Mech.*, **222**, 587–616.
- Prosperetti, A., Fundamental acoustic properties of bubbly liquids, in *Handbook of Elastic Properties of Solids, Liquids, and Gases*, Levy, Bass, & Stern, eds., vol. 4, Academic Press, New York, 2001, 183–205.
- Watanabe, M. & Prosperetti, A., 1994, Shock waves in dilute bubbly liquids, *J. Fluid Mech.*, **274**, 349–381.
- Wijngaarden, L. van, 1968, On the equations of motion for mixtures of liquid and gas bubbles, *J. Fluid Mech.*, **33**, 465–474.
- Zabolotskaya, E.A., 1977, Two self-action mechanisms for sound waves propagating in a gas-liquid mixture, *Sov. Phys. Acoust.*, **23**, 338–340.
- Zhang, D.Z. & Prosperetti, A., 1994, Ensemble phase-averaged equations for bubbly flows, *Phys. Fluids*, **6**, 2956–2970.

Part II

DIRECT NUMERICAL SIMULATION OF THERMOACOUSTIC REFRIGERATORS

O. Knio

Contents

1	Introduction and Summary	II-3
2	Physical Formulation	II-4
2.1	Governing equations	II-5
2.2	Normalization	II-6
2.2.1	Flow, fluid and material characteristic parameters	II-6
2.2.2	Geometrical parameters	II-7
2.3	Boundary Conditions	II-7
2.3.1	Condition at Matching Surfaces	II-8
2.3.2	Boundary conditions in the cross-stream direction	II-8
2.3.3	Thermal boundary conditions at the solid surfaces	II-9
3	Numerical Scheme	II-10
3.1	Discretization and notation	II-10
3.2	Time stepping	II-11
3.3	Domain decomposition	II-12
3.3.1	Streamfunction Distribution	II-12
3.3.2	Potential Distribution	II-13
3.4	Concluding remarks	II-16
4	Summary of Major Results	II-17
4.1	Flow Visualization	II-17
4.2	Mechanical Energy Losses	II-18
4.3	Validation and Analysis	II-19
4.4	Optimization of Heat Exchangers	II-25
Appendix		II-26
Bibliography		II-28

Chapter 1

Introduction and Summary

This part of the ONR-funded project focused primarily on the development of two-dimensional, unsteady, physical model and direct numerical simulation scheme for the study of simplified thermoacoustic refrigerators.

The model is based on the so-called zero-Mach-number approximation of the compressible conservation equations. The advantages of this asymptotic-based approach is that it enables us to overcome the large scale disparity that characterizes thermo-acoustic devices. Specifically, the approach combines a simplified representation of the action of acoustic waves, with detailed multi-dimensional resolution of the flow and temperature fields in the neighborhood of thermoacoustic stacks and heat exchangers.

Based on this attractive physical modeling approach, a vorticity-based numerical scheme was developed for efficient simulation of thermal and mechanical behavior of thermo-acoustic refrigerators. Specifically, the numerical scheme combines domain decomposition / boundary Green's function techniques with FFT-based elliptic equations solvers, which results in highly efficient approach for the simulation of thermo-acoustic devices.

At the start of this project, we started with a reduced formulation based on an adiabatic flow assumption and a physical model incorporating a single stack with no heat exchangers. This initial formulation was subsequently relaxed and the model underwent several levels of refinement. Various milestones have been summarized in a number of archival publications [1, 2, 3, 4, 5, 6, 7], and the refinements culminated in Dr. Besnoin's Ph.D. thesis [8].

In Chapter 2, a summary of the most refined version of the physical model is presented. Chapter 3 then outlines the corresponding numerical scheme. We conclude in Chapter 4 with a summary of major findings.

Chapter 2

Physical Formulation

The physical formulation has been specifically adapted to the simplified thermoacoustic refrigerator geometry illustrated in figure 2.1. The governing equations are derived by following the procedure described in [6] which is summarized below. First, the Navier-Stokes equations are made dimensionless using an appropriate choice of normalizing parameters. The gas dynamic variables are then expanded in terms of the Mach number and the corresponding asymptotic series is substituted for each variable, and the leading order equations are derived.

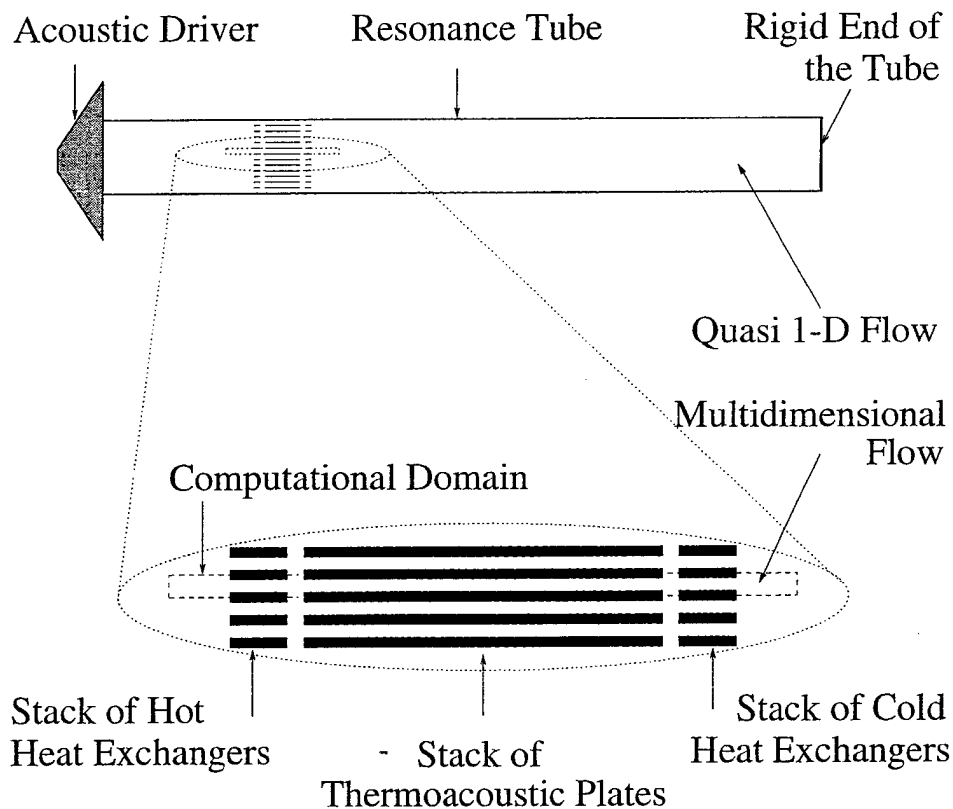


Figure 2.1: Schematic illustration of the thermoacoustic refrigerator (top) with a magnified view of the computational domain (bottom).

2.1 Governing equations

The formulation is based on the assumptions that: (a) the amplitude of the pressure oscillations in the inner region is small compared to the background pressure; (b) the flow field is two-dimensional; (c) the stack and heat exchangers are non-intrusive, meaning that they don't affect the flow in the "outer region", which remains quasi-1D; (d) the stack and heat exchangers have dimensions that are much smaller than the wavelength of the acoustic standing wave, so that the inner computational domain can be assumed to be acoustically compact [2, 6]; and (e) the gas is Newtonian and has constant viscosity and thermal conductivity.

Under these assumptions, the Mach number ($M = \tilde{u}_{ref}/\tilde{c}$) is small and a low Mach number expansion of each gas dynamic in an asymptotic series in terms of $\epsilon = \gamma M^2$ is appropriate. Here, γ is the specific heat ratio, \tilde{u}_{ref} is the reference velocity and \tilde{c}_{ref} is the sonic velocity. By expanding the equation variables in an asymptotic series in terms of M , and by suitably combining the state, continuity and energy equations, the normalized Navier-Stokes equations governing the motion of the gas are reduced to [9, 2]:

1. The equation of state:

$$P = \rho T \quad (2.1)$$

2. The equation for the evolution of the pressure:

$$\frac{V}{\gamma} \frac{dP}{dt} = -P \int_{\partial D} \mathbf{u} \cdot \mathbf{n} dA + \frac{1}{Pe} \int_{\partial D} \nabla T \cdot \mathbf{n} dA + \frac{Ec}{Re} \int_D \Phi dV \quad (2.2)$$

which can also be written as:

$$\int_{\partial D} \mathbf{u} \cdot \mathbf{n} dA = \frac{1}{P} \left[-\frac{V}{\gamma} \frac{dP}{dt} + \frac{1}{Pe} \int_{\partial D} \nabla T \cdot \mathbf{n} dA + \frac{Ec}{Re} \int_D \Phi dV \right] \quad (2.3)$$

3. The Helmholtz decomposition is used to decompose the velocity field into an irrotational part $\nabla\phi$ and a divergence free rotational part $\nabla \times (\psi \mathbf{k})$:

$$\mathbf{u} = \nabla\phi + \nabla \times (\psi \mathbf{k}) \quad (2.4)$$

$$\nabla^2\psi = -\zeta \quad (2.5)$$

$$\nabla^2\phi = -\frac{1}{P} \left[\frac{1}{\gamma} \frac{dP}{dt} + \frac{1}{Pe} \nabla^2 T + \frac{Ec}{Re} \Phi \right] \quad (2.6)$$

4. The vorticity transport equation:

$$\frac{\partial \zeta}{\partial t} = -\nabla \times (\zeta \times \mathbf{u}) - \frac{\nabla \rho}{\rho} \times \frac{D\mathbf{u}}{Dt} + \frac{1}{\rho Re} \nabla^2 \zeta \quad (2.7)$$

5. The energy equation for the fluid:

$$\rho \frac{\partial T}{\partial t} = -\rho \mathbf{u} \cdot \nabla T + \frac{\gamma - 1}{\gamma} \frac{dP}{dt} + \frac{1}{Pe} \nabla^2 T + \frac{Ec}{Re} \Phi \quad (2.8)$$

Here $\mathbf{u} = (u, v) = \tilde{u}/\tilde{u}_{ref}$ is the velocity vector, ζ the vorticity, ϕ the velocity potential, ψ the streamfunction, \mathbf{k} is the right-handed normal to the plane of motion, P the thermodynamic pressure, T the temperature, ρ the density, Φ the viscous dissipation function [10], $D/Dt = \partial/\partial t + \mathbf{u} \cdot \nabla$ the material derivative, γ the specific heat ratio, while D denotes the computational domain, ∂D its boundary, and \mathbf{n} the outer normal at ∂D . $Re = \tilde{u}_{ref} \tilde{l}_{ref}/\tilde{\nu}$ is the Reynolds number, ν is the kinematic viscosity. $Pe = \tilde{\rho}_{ref} \tilde{C}_p \tilde{u}_{ref} \tilde{l}_{ref}/\tilde{k}$ is the Peclet number for the gas, \tilde{k} is the thermal conductivity of the gas and C_p is the specific heat at constant pressure of the gas. $Ec = \tilde{\rho}_{ref}/(\tilde{C}_p \tilde{T}_{ref})$ is the Eckert number. \tilde{T}_{ref} , ρ_{ref} , \tilde{l}_{ref} , are the reference temperature, fluid density and length, respectively.

The temperature distribution within the plates is governed by the unsteady heat conduction equation:

$$\frac{\partial T_s}{\partial t} = \frac{1}{Pe_s} \nabla^2 T_s, \quad (2.9)$$

where $Pe_s = \tilde{\Omega} \tilde{H}^2 / \tilde{\alpha}_s$ is the Peclet number for the solid. Finally, the hot and cold heat exchangers are treated as isothermal. Their respective temperatures \tilde{T}_h and \tilde{T}_c are imposed.

One of the key features of the present model is that it enables us to isolate a small neighborhood of the stack and heat exchangers. Within this region, which is assumed to be “acoustically compact”, the model ignores elastic effects but retains bulk compressibility and convective nonlinearities in a stratified medium. This enables us to avoid sonic CFL limitations and thus efficiently analyze the details of the 2D flow.

2.2 Normalization

The variables are normalized with respect to the appropriate combination of angular frequency $\tilde{\Omega}$ of the acoustic standing wave, stack plate spatial periodicity \tilde{H} , mean pressure \tilde{P}_m , mean temperature \tilde{T}_m , and mean density of the fluid $\tilde{\rho}_m$. Thus, we have:

- $\tilde{t}_{ref} = \tilde{\Omega}^{-1}$
- $\tilde{l}_{ref} = \tilde{H}$
- $\tilde{P}_{ref} = \tilde{P}_m$
- $\tilde{T}_{ref} = \tilde{T}_m$
- $\tilde{\rho}_{ref} = \tilde{\rho}_m$

The choice of \tilde{H} and $\tilde{\Omega}^{-1}$ as length and time scales leads to the reference velocity scale $\tilde{u}_{ref} = \tilde{\Omega} \tilde{H}$.

2.2.1 Flow, fluid and material characteristic parameters

The normalization process leads to the definition of the following dimensionless parameters:

- Reynolds number, $Re \equiv \tilde{\Omega} \tilde{H}^2 / \tilde{\nu}$
- Eckert number, $Ec \equiv \tilde{\rho}_m / (\tilde{C}_p \tilde{T}_m)$
- Gas Peclet number $Pe \equiv \tilde{\Omega} \tilde{H}^2 / \tilde{\alpha}$
- Solid Peclet number, $Pe_s \equiv \tilde{\Omega} \tilde{H}^2 / \tilde{\alpha}_s$, which describes the thermal properties of the plate material.

Here $\tilde{\alpha}_s$ and $\tilde{\alpha} = \tilde{k}/(\tilde{\rho} \tilde{C}_p)$ denote the thermal diffusivities of the solid and the gas, respectively. In addition to these four dimensionless numbers which appear during the derivation of the governing equation, the following parameters are relevant in the study of the thermally stratified flows in thermoacoustic refrigerators:

- The viscous penetration depth $\tilde{\delta}_v \equiv \sqrt{2\tilde{\nu}/\tilde{\Omega}}$. Within a distance $\tilde{\delta}_v$ from the solid surfaces, viscous shear forces cause gradients in oscillating velocities.
- The thermal penetration depth $\tilde{\delta}_k \equiv \sqrt{2\tilde{\alpha}_f/\tilde{\Omega}}$. The thermal penetration depth is a scale for the distance that heat diffuses through the fluid in an acoustic period. In conventional thermoacoustic engines, $\tilde{\delta}_k$ ranges from O (0.1 mm) to O (1 mm), and is orders of magnitude smaller than the acoustic wavelength $\tilde{\lambda}$. Gas particles located further than $\tilde{\delta}_k$ from the solid surfaces undergo essentially adiabatic oscillations and do not contribute to the thermoacoustic effects.
- The particle displacement amplitude $\tilde{R}_p \equiv \tilde{u}_a / \tilde{\Omega}$, where $\tilde{u}_a \equiv \tilde{c} D r \sin(kx) / \gamma$, is the local velocity amplitude derived using linear acoustics in the resonance tube. In the literature, the particle displacement is sometimes referred to as the tidal displacement, which is equivalent to $2R_p$.

- The Prandtl number $\text{Pr} \equiv \tilde{\mu}\tilde{C}_p/\tilde{k} \equiv (\delta_v/\delta_k)^2$. The Prandtl number is a dimensionless measure of the ratio of viscous to thermal effects. In the case of monatomic ideal gases, $\text{Pr} \simeq 2/3$.
- The acoustic Reynolds number $\text{Re}_a \equiv 2\tilde{u}_a/\sqrt{\tilde{\nu}\tilde{\Omega}}$. The acoustic Reynolds number is a dynamic Reynolds number based on the acoustic wave velocity \tilde{u}_a . Note that $\text{Re}_a^2 = 4 \text{Re} R_p^2$. Re_a can be used to determine whether the Stokes boundary layers are stable or undergo transition to turbulence [11].

2.2.2 Geometrical parameters

The geometry of the resonance tube, stack and heat exchangers (Fig. 2.2) is specified in terms of:

- \tilde{H} , the stack plate spatial periodicity, or centerline separation distance.
- \tilde{d} , the thickness of plate and heat exchangers. In the idealized refrigerator depicted in figure 2.2, the plates and heat exchangers are assumed to have the same thickness.
- \tilde{h} is the spacing between two consecutive plates or heat exchangers. We have $\tilde{H} = \tilde{d} + \tilde{h}$.
- The blockage ratio, $\text{BR} \equiv h/H$, which is used to study the blockage effect of the stacks on the flow.
- \tilde{L}_h and \tilde{L}_c , which denote the length of the hot and cold heat exchangers, respectively. When \tilde{L}_h and \tilde{L}_c have the same value, both parameters are synthetised using $\tilde{L}_{h/c}$.
- \tilde{g} , the gap width that separates the thermoacoustic stack from the stacks of heat exchangers. The distance between the stack plates and the cold heat exchangers and the distance between the stack plates and the hot heat exchangers can be different. However, in all the computations, both distances are considered equal, which justifies the absence of subscripts in the notation.
- $D_{he-\partial D}$ is the distance which determines the location of the acoustic matching surfaces.
- kx is the dimensionless wave-number based on the non-dimensional wave-number k and the distance of the stack from the rigid end of the tube x .

All the parameters are listed in the nomenclature.

2.3 Boundary Conditions

The simulations are based on the assumption that the thermoacoustic stack is composed of a large number of identical, equi-spaced plates and that the hot and cold heat exchangers have the same number of plates and the same plate spacing H as the stack (fig. 2.2). We model this setting by restricting the simulations to a single period and imposing periodic boundary conditions in the direction normal to the acoustic axis.

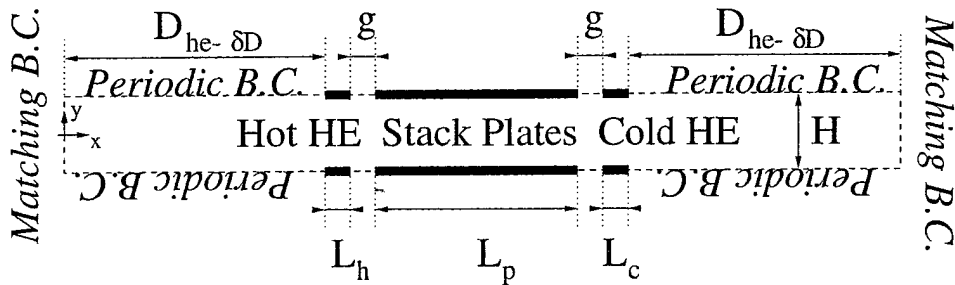


Figure 2.2: Schematic illustration of the computational domain, showing the dimensions of the stack and heat exchanger plates, the gap g between the stack and heat exchangers, the channel height H and the location of the matching boundaries.

As shown in figure 2.3, the boundary of the computational domain is divided into 8 sets, $\partial D = \bigcup_{i=1}^8 \Gamma_i$. In the cross-stream direction, the computational domain is limited by the sets Γ_2 , Γ_3 , Γ_5 and Γ_6 , where periodic boundary conditions are imposed. The inlet/outlet surfaces Γ_1 and Γ_4 limit the computational domain in the “streamwise” direction. On these surfaces, the solution matches the wave representation in the “outer region”, which is assumed to be dominated by a quasi-1D, idealized acoustic standing wave. In the following, we refer to these computational surfaces as matching boundaries.

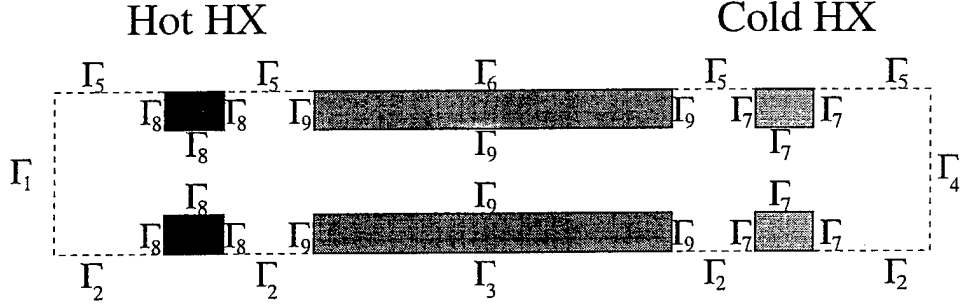


Figure 2.3: Schematic illustration of the computational domain and the limiting boundaries.

2.3.1 Condition at Matching Surfaces

The action of the standing wave is represented by prescribing oscillations of the thermodynamic pressure, P , and the mean flow velocity. Here, the integral constraint in (Eq. 2.3) is used to compute the oscillating velocities at the ends of the computational domain, which in turn are used to impose the boundary conditions for the vorticity, streamfunction and velocity potential on Γ_1 and Γ_4 . The *computed* inlet and outlet velocities u_1 and u_2 are obtained by adequately combining equations (2.10) and (2.11).

The difference between the velocities is computed using Eq. (2.3), the left hand side of which can be re-written as:

$$u_2 - u_1 = \frac{1}{A} \int_{\partial D} \mathbf{u} \cdot \mathbf{n} dA \quad (2.10)$$

The second constraint is obtained assuming that the average of the inlet and outlet flow velocities matches the prescribed instantaneous mean flow velocity u_a at the location of the stack. u_a is obtained by using linear acoustics in the resonance tube. This leads to:

$$\frac{1}{2}(u_2 + u_1) = u_a = \frac{Dr}{\gamma M} \sin(kx) \cos(t) \quad (2.11)$$

Thermal boundary conditions at the matching surfaces correspond to the vanishing flux conditions [3, 4, 12]:

$$\frac{\partial T}{\partial y} = 0 \text{ on } \Gamma_1 \text{ and } \Gamma_4 \quad (2.12)$$

These conditions are motivated by the fact that as one moves away from the stack and heat exchangers the thermoacoustic effect is expected to essentially vanish, so that the axial thermal gradients should decrease as well.

2.3.2 Boundary conditions in the cross-stream direction

In the fluid and the stack plate, the periodicity boundary conditions on surfaces Γ_2 to Γ_5 are implemented by imposing:

$$\phi(y, t)|_{\Gamma_2} = \phi(y, t)|_{\Gamma_5} \quad (2.13)$$

$$\psi(y, t)|_{\Gamma_2} = \psi(y, t)|_{\Gamma_5} \quad (2.14)$$

$$T(y, t)|_{\Gamma_2} = T(y, t)|_{\Gamma_5} \quad (2.15)$$

and

$$T_s(y, t)|_{\Gamma_3} = T_s(y, t)|_{\Gamma_6} \quad (2.16)$$

As noted in [2], the imposition of periodicity conditions on the potential (2.13) and streamfunction (2.14) is desirable, since it prevents the development of a mean flow along the y direction, and thus avoids potential difficulties associated with imposing periodicity conditions on the velocity itself.

Γ_9 is an internal boundary, which represents the surface of the plate; Γ_7 and Γ_8 represent the surfaces of the cold and hot heat exchangers respectively. At these 3 surfaces, no slip and zero-normal velocity conditions are used and are implemented by imposing,

$$\frac{\partial \phi}{\partial n} = 0 \quad (2.17)$$

$$\psi = 0 \quad (2.18)$$

$$\frac{\partial \psi}{\partial n} = -\frac{\partial \phi}{\partial p} \quad (2.19)$$

where n is the normal to the plate surface and $p = n \times k$ is the unit vector tangent to the plate surface. Note that, as discussed in 2.3.1, the particular choice of velocity potential and streamfunction boundary conditions corresponds to letting the potential velocity carry the entire volume flux through the domain. Thus, the streamfunction distribution does not induce a mean flow and describes a non-linear vortical perturbation to an otherwise ideal, irrotational flow.

2.3.3 Thermal boundary conditions at the solid surfaces

The heat exchangers are treated as isothermal solid bodies with constant hot temperature T_h , and cold temperature T_c , which are imposed on Γ_8 and Γ_7 respectively.

Meanwhile, on Γ_9 , the conduction solution within the stack plates is coupled to the energy equation for the gas. We require that the temperature solutions and the corresponding conduction fluxes within the gas and solid coincide at the plate surface. Thus, we impose:

$$T(q, t) = T_s(q, t) \quad (2.20)$$

$$\frac{\partial T}{\partial n}(q, t) = \kappa \frac{\partial T_s}{\partial n}(q, t) \quad (2.21)$$

where q is a coordinate variable along Γ_9 and $\kappa \equiv \tilde{k}_s/\tilde{k}$ is the ratio of the thermal conductivity in the solid to the thermal conductivity of the gas.

Chapter 3

Numerical Scheme

The numerical simulation of the model equations is based on a finite difference methodology. Spatial derivatives are approximated using second-order centered differences, and time integration is based on the third-order Adams-Bashforth scheme.

The construction of the scheme can be decomposed into two parts. First, the model variables are updated, following a procedure which varies according to the type of representation for the acoustic standing wave discussed in 2.3.1. Both procedures are developed in section 3.2. The second step consists in reconstructing the velocity fields from the vorticity and divergence fields. The reconstruction of the velocity involves the solution of two elliptic equations which are inverted using fast Poisson solvers. The fast solvers are based on domain-decomposition / boundary Green's functions techniques, the construction of which is discussed in 3.3.

3.1 Discretization and notation

The numerical implementation developed in [6] was extended in order to accommodate the presence of heat exchangers. The discretization also carries out a wider variety of boundary conditions at the matching surfaces. The model equations are discretized using a finite difference method. Specifically, the model variables are discretized on a rectangular mesh with size Δx and Δy in the x and y directions (Fig. 3.1). In the cross-stream direction, NX is used to denote the number of cells between Γ_2 and Γ_5 in domains D_1 , D_3 , D_5 and D_7 , whereas $NX2$ denotes the number of cells between two consecutive plate or heat exchanger surfaces. In the streamwise direction, NY_i indicates the number of cells in the corresponding domain D_i .

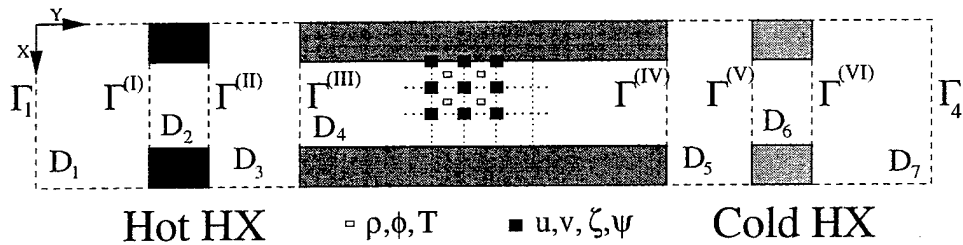


Figure 3.1: Schematic illustration of the computational domain mesh grid and of the internal boundaries

Velocity, streamfunction and vorticity distributions are discretized on the edges of the computational cells. Density, temperature and velocity potential are discretized on the cell centers as shown on Fig 3.1. Time integration of the system of discrete evolution equations is performed using the explicit, third-order Adams-Bashforth scheme.

Spatial derivatives are discretized using second-order differences. On a rectangular grid, a standard

center-difference approximation to the gradient and Laplacian operators respectively yields:

$$\nabla_h f_{i,j}^n = \frac{f_{i+1,j}^n - f_{i-1,j}^n}{2\Delta x} + \frac{f_{i,j+1}^n - f_{i,j-1}^n}{2\Delta y} \quad (3.1)$$

and

$$\nabla_h^2 f_{i,j}^n = \frac{f_{i+1,j}^n - 2f_{i,j}^n + f_{i-1,j}^n}{\Delta x^2} + \frac{f_{i,j+1}^n - 2f_{i,j}^n + f_{i,j-1}^n}{\Delta y^2} \quad (3.2)$$

The material derivative at time $n\Delta t$ is approximated using:

$$\begin{aligned} \frac{Du_{i,j}^n}{Dt} &\simeq \frac{\partial u_{i,j}^n}{\partial t} + u_{i,j}^n \nabla_h u_{i,j}^n \\ &\simeq \frac{3u_{i,j}^n - 4u_{i,j}^{n-1} + u_{i,j}^{n-2}}{2\Delta t} + u_{i,j}^n \nabla_h u_{i,j}^n \end{aligned} \quad (3.3)$$

i.e., the temporal derivative is estimated using a second-order backward difference while the convective term is computed using a standard centered-difference formula.

As shown in figure 3.1, the computational domain for the flow field can be divided into seven rectangular internal sub-domains D_1 to D_7 , bounded in the streamwise direction by the matching boundaries Γ_1 and Γ_4 , and by six internal boundaries $\Gamma^{(I)}$ to $\Gamma^{(V)}$. Boundaries $\Gamma^{(I)}$ to $\Gamma^{(V)}$ are computational boundaries used in the numerical solution of elliptic equations (sections 3.3.1 and 3.3.2).

3.2 Time stepping

Implementation of the numerical scheme to the simulation of the unsteady 2D flow is based on successive repetition of the following steps.

1. Update the pressure, the pressure derivative and the mean flow velocity:

$$P^{n+1} = 1 + Dr \cos(kx) \sin[(n+1)\Delta t] \quad (3.4)$$

$$\left(\frac{dP}{dt}\right)^{n+1} = Dr \cos(kx) \cos[(n+1)\Delta t] \quad (3.5)$$

$$u_a^{n+1} = \frac{Dr}{\gamma M} \sin(kx) \cos[(n+1)t] \quad (3.6)$$

Compute the right hand side (rhs_3) of equation 2.3 :

$$\begin{aligned} rhs_3^{n+1} &= \frac{1}{P^{n+1}} \left[-\frac{V}{\gamma} \left(\frac{dP}{dt} \right)^{n+1} + \frac{1}{Pe} \int_{\partial D} \nabla T_{i,j}^n \cdot \mathbf{n} dA \right. \\ &\quad \left. + \frac{Ec}{Re} \int_D \Phi_{i,j}^n dV \right] \end{aligned} \quad (3.7)$$

Combine equations 2.10 and 2.11 so as to update the velocities at the matching surfaces Γ_1 and Γ_2 :

$$u_1^{n+1} = u_a^{n+1} - \frac{1}{2} rhs_3^{n+1} \quad (3.8)$$

$$u_2^{n+1} = u_a^{n+1} + \frac{1}{2} rhs_3^{n+1} \quad (3.9)$$

2. Integrate equation (2.7) in order to determine the vorticity values in the interior of the domain at the new time step. We set:

$$\begin{aligned} \zeta_{i,j}^{n+1} &= \zeta_{i,j}^n + \Delta t \sum_{k=0}^2 \beta_k \left[-\nabla_h \times (u_{i,j}^{n-k} \times \zeta_{i,j}^{n-k}) - \frac{\nabla_h \rho_{i,j}^{n-k}}{\rho_{i,j}^{n-k}} \times \frac{Du_{i,j}^{n-k}}{Dt} \right. \\ &\quad \left. + \frac{1}{\rho_{i,j}^{n-k} Re} \nabla_h^2 \zeta_{i,j}^{n-k} \right] \end{aligned} \quad (3.10)$$

3. Integrate the energy equation (2.8) in order to determine the new temperature distribution at interior points in the fluid domain. We use:

$$T_{i,j}^{n+1} = T_{i,j}^n + \Delta t \sum_{k=0}^2 \beta_k \left[- u_{i,j}^{n-k} \cdot \nabla_h T_{i,j}^{n-k} + \frac{\gamma - 1}{\gamma \rho_{i,j}^{n-k}} \frac{dP^{n-k}}{dt} + \frac{1}{Pe \rho_{i,j}^{n-k}} \nabla_h^2 T_{i,j}^{n-k} + \frac{Ec}{Re} \Phi_{i,j}^{n-k} \right] \quad (3.11)$$

4. Integrate the heat conduction equation (2.9) in order to update the temperature field at interior points within the solid. Thus, we set:

$$T_s|_{i,j}^{n+1} = T_s|_{i,j}^n + \frac{\Delta t}{Pe_s} \sum_{k=0}^2 \beta_k \nabla_h^2 T_s|_{i,j}^{n-k} \quad (3.12)$$

5. Determine the temperature distribution at solid surfaces by requiring that the heat flux be continuous there, i.e. by enforcing (eq. 2.21):

$$T_{surf}|_{i,j}^{n+1} = \frac{(4T_s|_{i-1,j}^{n+1} + 4\kappa T_{i+1,j}^{n+1}) - (T_s|_{i-2,j}^{n+1} + \kappa T_{i+2,j}^{n+1})}{3(1 + \kappa)} \quad (3.13)$$

6. Determine the new density field in the fluid from the equation of state (2.1). We set:

$$\rho_{i,j}^{n+1} = \frac{P^{n+1}}{T_{i,j}^{n+1}} \quad (3.14)$$

7. Determine the new streamfunction distribution and velocity potential by inverting the discrete Poisson equations corresponding to equations (2.5) and (2.6). This step is discussed in sections 3.3.1 and 3.3.2.
8. Reconstruct the velocity field from the divergence and vorticity fields (eq. 2.4) using the centered-difference approximations to the gradient operator described in 3.1.
9. And finally, update the vorticity at the surface of the heat exchangers and plate by imposing no-slip conditions at the solid surfaces. For more details, see [4].

Note that steps 1–6, 8 and 9 only involve straightforward algebraic manipulation. On the other hand, step 7 requires the inversion of two discrete elliptic operators, which accounts for most of the CPU time in the computations. The inversion of the streamfunction Poisson equation and determination of the potential distribution are performed using the fast domain-decomposition solver discussed in sections 3.3.1 and 3.3.2. The efficiency of both solvers was examined in [2]. Comments on the advantages of the inversion technique can be found in [6].

3.3 Domain decomposition

The inversion procedures for the determination of the streamfunction distribution and the velocity potential are summarized below. The procedures were first developed by Worlikar and Knio in [2, 6, 4] and are adapted to accommodate the inversion of the Laplacian operator in the computational domain shown in figure 3.1. Here, the technique is extended to the decomposition of the computational domain into 7 sub-domains.

3.3.1 Streamfunction Distribution

The streamfunction distribution at the new time level is governed by the following Poisson equation,

$$\nabla_h^2 \psi_{i,j}^{n+1} = -\zeta_{i,j}^{n+1} \quad (3.15)$$

with homogeneous Dirichlet boundary conditions on Γ_1 , Γ_4 and Γ_9 , and periodicity conditions on Γ_2/Γ_5 . The inversion is performed using a domain decomposition technique which subdivides the computational domain into seven non-overlapping regions, $D = \bigcup_{l=1}^7 D_l$. As sketched in figures 2.3 and 3.1, D_1 is bounded by the surfaces Γ_1 , Γ_2 , Γ_5 , Γ_8 and $\Gamma^{(I)}$, D_2 by $\Gamma^{(I)}$, Γ_8 and $\Gamma^{(II)}$, D_3 by $\Gamma^{(II)}$, $\Gamma^{(III)}$, Γ_2 , Γ_5 , Γ_8 and Γ_9 , D_4 by $\Gamma^{(III)}$, Γ_9 and $\Gamma^{(IV)}$, D_5 by $\Gamma^{(IV)}$, $\Gamma^{(V)}$, Γ_2 , Γ_5 , Γ_7 and Γ_9 , D_6 by $\Gamma^{(V)}$, Γ_7 and $\Gamma^{(VI)}$, and D_7 by $\Gamma^{(VI)}$, Γ_2 , Γ_5 , Γ_7 and Γ_4 .

The streamfunction distribution within individual sub-domains is decoupled using a boundary Green's function technique which is based on constructing, in a pre-processing step, M elementary solutions in each sub-domain, Ψ_m^l in D_l , $l = 1, 2, 3, 4, 5, 6, 7$, $m = 1, \dots, M$, where M is the number of internal boundary points on $\Gamma^{(I)}, \Gamma^{(II)}, \Gamma^{(III)}, \Gamma^{(IV)}, \Gamma^{(V)}$ and $\Gamma^{(VI)}$, $\{z_m\}_{m=1}^M$. The boundary Green's functions Ψ_m^l are the solutions of the following elementary problems:

$$\nabla_h^2 \Psi_m^l = 0 \text{ in } D^l \quad (3.16)$$

$l = 1, \dots, 7$, $j = 1, \dots, M$, with homogeneous Dirichlet boundary conditions on Γ_1 , Γ_4 , Γ_7 , Γ_8 and Γ_9 , periodicity conditions on Γ_2 and Γ_5 , and the following boundary conditions on the internal boundaries $\Gamma^{(I)}, \dots, \Gamma^{(VI)}$:

$$\Psi_j^l = \begin{cases} 1 & \text{if } x = z_j \\ 0 & \text{otherwise} \end{cases} \quad (3.17)$$

The individual streamfunction solutions at the new time level are expressed as a linear combination of the boundary Green's and of auxiliary solutions. We thus write:

$$\psi^{l,n+1} = \bar{\psi}^{l,n+1} + \sum_{m=1}^M \eta_m^{n+1} \Psi_m^l \quad l = 1, \dots, 7, \quad (3.18)$$

where the auxiliary solutions $\bar{\psi}^{l,n+1}$ are determined by inverting:

$$\nabla_h^2 \bar{\psi}^{l,n+1} = -\zeta^{l,n+1} \quad (3.19)$$

with homogeneous Dirichlet conditions on Γ' and Γ'' , periodicity conditions on Γ_2 and Γ_5 , and homogeneous Dirichlet conditions on Γ_1 , Γ_4 and Γ_7 . The unknown coefficients η_m^{n+1} are determined by requiring that the normal derivative of the streamfunction at internal boundaries –approximated within individual sub-domains using second-order one-sided derivatives– be continuous at $\Gamma^{(I)} - \Gamma^{(VI)}$. This results in an $M \times M$ system of linear equations, whose corresponding influence matrix is denoted by A . Its inverse, A^{-1} , is determined by Gaussian elimination in a pre-processing step, and then fed to the computations. The advantage of the domain decomposition / boundary Green's function approach is that it decouples the inversion procedures in elementary sub-domains and facilitates the implementation of fast solvers. In the computations, we take advantage of the fact that the sub-domains $D_1 - D_7$ are rectangular, and of the nature of the boundary conditions on horizontal surfaces. Specifically, in D_1, D_3, D_5 and D_7 we exploit of the periodicity conditions on Γ_2/Γ_5 by using a discrete FFT of the governing equations [13, 14]. In D_2, D_4 and D_6 , we take advantage of the homogeneous Dirichlet conditions on the streamfunction by implementing a fast sine transform. These transformations lead to decoupled tridiagonal systems for the Fourier/sine coefficients, which are efficiently determined using the Thomas algorithm [13, 14]. Thus, the streamfunction distribution is determined using a procedure that requires essentially $O(N \log N)$ operations.

3.3.2 Potential Distribution

The velocity potential is governed by the following Poisson equation:

$$\nabla_h^2 \phi_{i,j}^{n+1} = \epsilon_{i,j}^{n+1} \equiv \frac{1}{P} \left[-\frac{1}{\gamma} \frac{dP^{n+1}}{dt} + \frac{1}{Pe} \nabla_h^2 T_{i,j}^{n+1} + \frac{Ec}{Re} \Phi_{i,j}^n \right] \quad (3.20)$$

with periodicity conditions on Γ_2 and Γ_5 , non-homogeneous Neumann conditions on Γ_1 and Γ_4 given by equations (2.10,2.11), and a homogeneous Neumann condition on the solid surfaces, Γ_7 , Γ_8 and Γ_9 . Fast

solution of the above system is performed using a domain decomposition technique which was developed by Worlikar and Knio [4] and which is summarized below.

The construction of the velocity potential solver is more involved than that of the streamfunction solver, in large part due to the Neumann boundary conditions imposed on the solid surface, Γ_7 , Γ_8 and Γ_9 and the acoustic matching surfaces, Γ_1 and Γ_4 . One difficulty is that the use of Dirichlet conditions on the coupling surfaces $\Gamma^{(I)} - \Gamma^{(VI)}$ would lead to a mixed Dirichlet/Neumann problem on $\Gamma^{(I)}/\Gamma_8 - \Gamma^{(VI)}/\Gamma_7$, which would greatly complicate (or prevent) implementation of a fast Fourier solver. An additional concern is that the potential distribution is only determined up to an additive, arbitrary constant; thus, the coupling of solutions across sub-domain boundaries must carefully account for this feature. Also, sufficient care must be exercised so that the compatibility condition for the original problem (3.20), which is guaranteed in light of (2.2), remains satisfied. In order to address these issues, we first note that in the implementation of the domain decomposition technique it is only necessary to determine, within individual sub-domains, potential distributions that (i) satisfy compatibility conditions *locally* over each sub-domain, and (ii) yield *velocity* predictions that are continuous across computational surfaces joining different sub-domains ($\Gamma^{(I)}$ to $\Gamma^{(VI)}$). This is the case because it is only the gradient of the velocity potential that enters in the formulation of the physical model. Based on this observation, we proceed as follows. We use the same domain sub-division used in section 3.3.1 and express the solution within individual sub-domains as:

$$\phi^{l,n+1} = \bar{\phi}^{l,n+1} + \sum_{k=1}^{M'} \sigma_k^{n+1} \Phi_k^l, \quad l = 1, \dots, 7, \quad (3.21)$$

where M' is the total number of segment centers lying on $\Gamma^{(I)} - \Gamma^{(VI)}$, $\{z'_k\}_{k=1}^{M'}$. Note that $M' = M + 6$, and that the collocation points along the interface differ from those used for the streamfunction, i.e. $z_k \neq z'_k$ for all k . For clarity of the presentation, we assume that the collocation points z' are indexed consecutively such that $z'_k \in \Gamma^{(I)}$ for $1 \leq k \leq N_\Gamma$, $z'_k \in \Gamma^{(II)}$ for $N_\gamma + 1 \leq k \leq 2N_\gamma$, $z'_k \in \Gamma^{(III)}$ for $2N_\gamma + 1 \leq k \leq 3N_\gamma$, $z'_k \in \Gamma^{(IV)}$ for $3N_\gamma + 1 \leq k \leq 4N_\gamma$, $z'_k \in \Gamma^{(V)}$ for $4N_\gamma + 1 \leq k \leq 5N_\gamma$ and $z'_k \in \Gamma^{(VI)}$ for $5N_\gamma + 1 \leq k \leq M'$. The elementary boundary Green's functions are elementary solutions of the following *non-homogeneous* Neumann problems:

$$\nabla_h^2 \Phi_k^l = \epsilon^l, \quad l = 1, \dots, 7, \quad (3.22)$$

where

$$\epsilon^l = \frac{\Delta y}{|D_l|} \quad (3.23)$$

and $|D_l|$ is the volume of domain D_l . In conjunction with (3.22), we use periodicity conditions on Γ_2 and Γ_5 , homogeneous Neumann conditions on Γ_1 , Γ_4 , Γ_7 , Γ_8 and Γ_9 , and the following Neumann conditions,

$$\begin{cases} \frac{\partial \Phi_k^l}{\partial y} = 1 & \text{if } x = z'_k \\ \frac{\partial \Phi_k^l}{\partial y} = 0 & \text{otherwise} \end{cases} \quad (3.24)$$

on $\Gamma^{(I)} - \Gamma^{(VI)}$. Note that since the Φ_k^l are solutions of Neumann problems they are only determined up to an additive arbitrary constant, and that the compatibility condition for (3.22) is automatically satisfied following the definition of ϵ^l (3.23). The potential distributions $\bar{\phi}^{l,n+1}$, $l = 1, \dots, 7$, are the numerical solutions of:

$$\nabla_h^2 \bar{\phi}^{l,n+1} = \epsilon^l, \quad (3.25)$$

with periodicity conditions on Γ_2 and Γ_5 , homogeneous Neumann conditions on Γ_7 , Γ_8 and Γ_9 , and the following inhomogeneous Neumann conditions on Γ_1 , Γ_4 , $\Gamma^{(I)} - \Gamma^{(VI)}$,

$$\left. \frac{\partial \bar{\phi}^{1,n+1}}{\partial y} \right|_{\Gamma_1} = u_1(t^{n+1}) \quad (3.26)$$

$$\left. \frac{\partial \bar{\phi}^{7,n+1}}{\partial y} \right|_{\Gamma_4} = u_2(t^{n+1}) \quad (3.27)$$

$$\frac{\partial \bar{\phi}^{l,n+1}}{\partial y} \Big|_{\Gamma^{(I)}} = \bar{U}^{(I)} \equiv \frac{1}{h} \left[\int_{D_1} \epsilon^{1,n+1} dV + u_1(t^{n+1}) H \right], \quad l = 1, 2 \quad (3.28)$$

$$\frac{\partial \bar{\phi}^{l,n+1}}{\partial y} \Big|_{\Gamma^{(II)}} = \bar{U}^{(II)} \equiv \frac{1}{h} \left[\int_{D_2} \epsilon^{2,n+1} dV \right] + \bar{U}^{(I)}, \quad l = 2, 3 \quad (3.29)$$

$$\frac{\partial \bar{\phi}^{l,n+1}}{\partial y} \Big|_{\Gamma^{(III)}} = \bar{U}^{(III)} \equiv \frac{1}{h} \left[\int_{D_3} \epsilon^{3,n+1} dV \right] + \bar{U}^{(II)}, \quad l = 3, 4 \quad (3.30)$$

$$\frac{\partial \bar{\phi}^{l,n+1}}{\partial y} \Big|_{\Gamma^{(IV)}} = \bar{U}^{(IV)} \equiv \frac{1}{h} \left[\int_{D_4} \epsilon^{4,n+1} dV \right] + \bar{U}^{(III)}, \quad l = 4, 5 \quad (3.31)$$

$$\frac{\partial \bar{\phi}^{l,n+1}}{\partial y} \Big|_{\Gamma^{(V)}} = \bar{U}^{(V)} \equiv \frac{1}{h} \left[\int_{D_5} \epsilon^{5,n+1} dV \right] + \bar{U}^{(IV)}, \quad l = 5, 6 \quad (3.32)$$

$$\frac{\partial \bar{\phi}^{l,n+1}}{\partial y} \Big|_{\Gamma^{(VI)}} = \bar{U}^{(VI)} \equiv \frac{1}{h} \left[\int_{D_6} \epsilon^{6,n+1} dV \right] + \bar{U}^{(V)}, \quad l = 6, 7 \quad (3.33)$$

respectively. Note that the solvability conditions for (3.25) in $D_1 - D_6$ are automatically satisfied by construction of the non-homogeneous Neumann conditions (3.28) to (3.33), respectively, while the compatibility condition for (3.25) in D_7 follows from the compatibility condition of the original problem (3.20). Also note that, by construction, the combination of boundary Green's functions and auxiliary solutions (3.21) automatically satisfies the continuity of the normal derivative of ϕ at $\Gamma^{(I)} - \Gamma^{(VI)}$. Thus, the obvious next step would be to determine the unknown coefficients σ_k^{n+1} by requiring continuity of the potential itself at $\Gamma^{(I)} - \Gamma^{(VI)}$. However, such an exercise would be complicated since both the auxiliary solutions $\bar{\phi}^{l,n+1}$ and the boundary Green's functions Φ_k^l are determined up to an arbitrary additive constant. To avoid this difficulty, while at the same time accounting for the indeterminacy of ϕ , we first observe that if a reference value for the potential in each subdomain is correctly selected at one point along the interface, then continuity of the potential at the remaining points would follow from continuity of the *tangential* derivative. The selection of the reference point is of course arbitrary; for convenience, we choose the first collocation points on $\Gamma^{(I)} - \Gamma^{(VI)}$ as reference points, and so require the continuity of the tangential derivative at the remaining points. This results in:

$$\left\{ \begin{array}{l} \text{For } j = 2, \dots, N_\Gamma: \\ \sum_{k=1}^{M'} \sigma_k^{n+1} \left[\frac{\partial \Phi_k^1}{\partial x}(z'_j) - \frac{\partial \Phi_k^2}{\partial x}(z'_j) \right] = \frac{\partial \bar{\phi}^{2,n+1}}{\partial x}(z'_j) - \frac{\partial \bar{\phi}^{1,n+1}}{\partial x}(z'_j) \\ \text{For } j = N_\Gamma + 2, \dots, 2N_\Gamma: \\ \sum_{k=1}^{M'} \sigma_k^{n+1} \left[\frac{\partial \Phi_k^2}{\partial x}(z'_j) - \frac{\partial \Phi_k^3}{\partial x}(z'_j) \right] = \frac{\partial \bar{\phi}^{3,n+1}}{\partial x}(z'_j) - \frac{\partial \bar{\phi}^{2,n+1}}{\partial x}(z'_j) \\ \text{For } j = 2N_\Gamma + 2, \dots, 3N_\Gamma: \\ \sum_{k=1}^{M'} \sigma_k^{n+1} \left[\frac{\partial \Phi_k^3}{\partial x}(z'_j) - \frac{\partial \Phi_k^4}{\partial x}(z'_j) \right] = \frac{\partial \bar{\phi}^{4,n+1}}{\partial x}(z'_j) - \frac{\partial \bar{\phi}^{3,n+1}}{\partial x}(z'_j) \\ \text{For } j = 3N_\Gamma + 2, \dots, 4N_\Gamma: \\ \sum_{k=1}^{M'} \sigma_k^{n+1} \left[\frac{\partial \Phi_k^4}{\partial x}(z'_j) - \frac{\partial \Phi_k^5}{\partial x}(z'_j) \right] = \frac{\partial \bar{\phi}^{5,n+1}}{\partial x}(z'_j) - \frac{\partial \bar{\phi}^{4,n+1}}{\partial x}(z'_j) \\ \text{For } j = 4N_\Gamma + 2, \dots, 5N_\Gamma: \\ \sum_{k=1}^{M'} \sigma_k^{n+1} \left[\frac{\partial \Phi_k^5}{\partial x}(z'_j) - \frac{\partial \Phi_k^6}{\partial x}(z'_j) \right] = \frac{\partial \bar{\phi}^{6,n+1}}{\partial x}(z'_j) - \frac{\partial \bar{\phi}^{5,n+1}}{\partial x}(z'_j) \\ \text{For } j = 5N_\Gamma + 2, \dots, M': \\ \sum_{k=1}^{M'} \sigma_k^{n+1} \left[\frac{\partial \Phi_k^6}{\partial x}(z'_j) - \frac{\partial \Phi_k^7}{\partial x}(z'_j) \right] = \frac{\partial \bar{\phi}^{7,n+1}}{\partial x}(z'_j) - \frac{\partial \bar{\phi}^{6,n+1}}{\partial x}(z'_j) \end{array} \right. \quad (3.34)$$

i.e. a linear system of $M' - 6$ equations in the M' unknown Green's function coefficients. To complete the system, two additional equations are used which require that the overall source term (divergence) corresponding to (3.21) coincides to that of the original (undecomposed) problem (3.20). Thus, we impose:

$$\sum_{k=1}^{N_T} \sigma_k^{n+1} = 0 \quad (3.35)$$

and

$$\sum_{k=N_T+1}^{M'} \sigma_k^{n+1} = 0 \quad (3.36)$$

The combined influence matrix, B , corresponding to (3.34), (3.35) and (3.36) is inverted in a pre-processing step, and its inverse B^{-1} is stored for use in the unsteady simulations.

3.4 Concluding remarks

With the present procedure, the unknown coefficients of the boundary Green's functions are uniquely determined. The end result is a potential distribution that satisfies the original governing equation within individual subdomains, and guarantees continuity of the normal and tangential derivatives of the potential along computational boundaries separating the subdomains. Since the physical model only involves the gradient of the velocity potential, continuity of the potential itself does not need to be guaranteed. The primary advantage of the present approach is that it facilitates the implementation of fast solvers for individual Neumann problems in (3.22) and (3.25). In the present computations, we exploit the special structure of the problems by using a fast Fourier solver D_1, D_3, D_5 , and D_7 and a fast cosine transform in D_2, D_4 and D_6 . Consequently, the overall algorithm is also $O(N \log N)$. Note that although the streamfunction and velocity potential are discretized using different grids, the Fourier-based techniques used in the fast inversion of the corresponding Poisson problems are compatible, i.e. they rely on the *same number* of points. The advantage of using a staggered grid for ϕ is that the potentially-delicate task of imposing Neumann conditions at the plate corners is avoided. In the simulations, computational grids are used that have a relatively large number of points. As a consequence, it is impractical to store the boundary Green's functions for the streamfunction and the potential. To overcome this problem, the inversion of the Poisson equations for the streamfunction and the velocity potential is performed twice. The first inversion enables us to determine the correct conditions at the computational boundaries $\Gamma^{(I)} - \Gamma^{(VI)}$, while the second inversion yields the complete solution. Despite the additional effort, the utilization of the fast solver remains quite attractive [6].

Chapter 4

Summary of Major Results

Direct numerical simulations have been extensively applied in a fundamental investigation of thermoacoustic refrigerators, with specific attention to thermal and mechanical behavior of the stack and heat exchangers. These analyses fell within the following four areas:

- Quantitative visualization of the flow field in the neighborhood of thermoacoustic stacks [1, 2, 6];
- Analysis of mechanical energy losses [4];
- Validation studies and fundamental analysis of thermal stack behavior [3, 8]; and,
- Optimization of heat exchanger configuration [7, 8].

Highlights from these studies are briefly discussed below.

4.1 Flow Visualization

As briefly outlined above, a detailed study of the unsteady flow field was carried out in [1, 2]. For brevity, for one configuration from the case study in [2] is described here.

The details of the flow-field are illustrated for a stack with a blockage ratio $BR = 0.666$ and a plate length parameter $L/H = 1.32$. The Reynolds number and the drive ratio are $Re = 2132$ and $Dr = 1.0\%$, respectively. The stack is kept at a position mid-way between the velocity node and the anti-node ($kx = 3\pi/4$).

The model is allowed to run till a quasi-steady periodic state is reached, i.e. the flow shows the same variation over consecutive acoustic cycles. Figure 4.1 shows the streamlines plotted for one acoustic cycle. The frames are generated one-eighth of a cycle apart and the arrows at the left of the frame indicate the magnitude and direction of the mean velocity at the center of the stack. The first frame is plotted at the start of the acoustic cycle when the acoustic velocity at the center is zero. The flow starts accelerating upwards till the velocity is maximum in frame (c). The flow then starts decelerating till the velocity vanishes in frame (e). The fluid then starts accelerating in the downward direction, reaches a maximum downward velocity in frame (g) and starts decelerating again. This sequence is repeated after frame (h).

As the flow starts accelerating upward (frame (b)), recirculation bubbles are formed just at the entrance of the channel. At the same time, an eddy is shed from the exit of the channel. An eddy at the entrance which was formed in the earlier cycle, gets crushed against the forward face of the channel and slides over the recirculation eddy formed at the entrance of the channel and migrates towards the centerline forming a vortex bubble near the centerline of the channel which then travels with the flow. As the flow accelerates upward, the recirculation zone at the entrance of the channel moves upward within the channel. Meanwhile, the separation bubbles at the exit of the channel continues to intensify as does the separation bubble in the channel near the entrance. As the flow is reversed (frames e-h), these processes are reversed – i.e. a recirculation eddy is formed behind the bottom end of the channel, whereas a recirculation zone is formed at the throat at the top end of the channel.

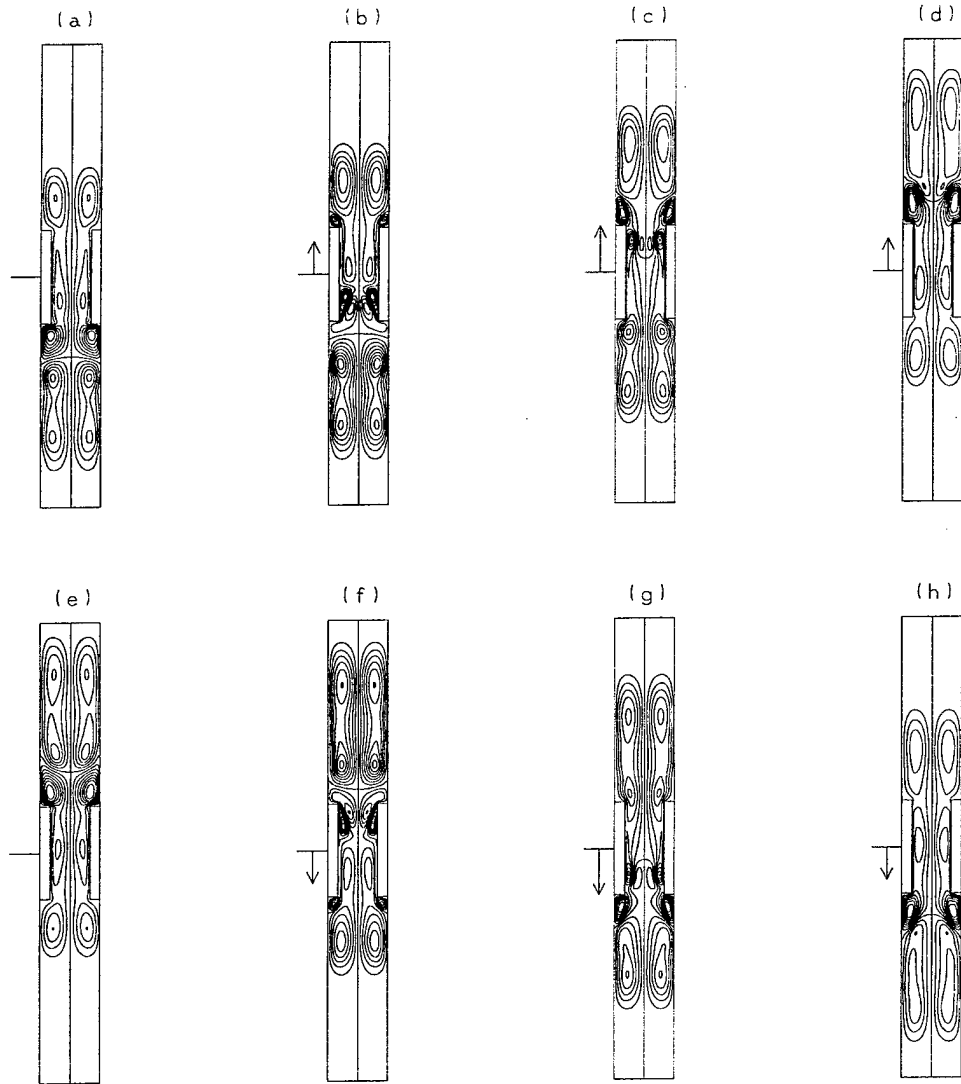


Figure 4.1: Evolution of streamfunction distribution for a stack with $h/H = 0.66$, $L/H = 1.32$, $Dr = 1.0\%$. The frames are generated at times (a) $t = 32\pi/4$, (b) $t = 33\pi/4$, (c) $t = 34\pi/4$, (d) $t = 35\pi/4$, (e) $t = 36\pi/4$, (f) $t = 37\pi/4$, (g) $t = 38\pi/4$ and (h) $t = 39\pi/4$.

As illustrated in figure 4.1, our analysis reveals that the flow field is strongly modulated by the motion of complex vortical structures which form due to the shedding of Stokes layers, and by the impingement of these structures on solid surfaces. As discussed below, these motions substantially affect the heat transfer rates and thermal performance of the refrigerator.

4.2 Mechanical Energy Losses

Extensive computations based on a simplified version of the low-Mach-number number were carried out in [5] in order to analyze the fluid force balance and mechanical energy losses in a thermoacoustic stack at low to moderate drive ratios.

In particular, this study has tested the hypothesis that the net hydrodynamical effect on the momentum balance of a stack of narrowly spaced plates in an otherwise essentially one-dimensional resonant acoustic field can be represented by effective impedance laws similar to those used in linear theory. To this end, the analysis assumed a purely sinusoidal input of mean mass flux and weak (acoustic) compressibility to drive an

inelastic two-dimensional, weakly compressible flow around a stack of rectangular plates. The forces imposed by the plates on the surrounding flow were consequently analyzed.

The force balance was first used to show that the response of the stack on the outer sinusoidal driving is sinusoidal as well, up to errors of no more than 2% in all the cases considered. Explicit simplified formulae of the plate forces were then derived based on the linear theory. The simplest version assumes Poiseuille flow between the plates at all times, a more sophisticated one accounts for the dependence of the velocity profile on inertia and viscous effects. By comparison with the force balance from the detailed numerical simulation good agreement was obtained for the elaborate theory, but unsatisfactory agreement was found for the simplified Poiseuille-flow model.

From the force estimates explicit impedance laws were further obtained that can be used in quasi-one-dimensional simulations as approximate models of the effect of the thermoacoustic stack on the outer long wave acoustics. Comparison of the semi-heuristic estimates for the impedance with the results of the computations showed that for plate length to plate spacing ratios larger than about $L/H = 8$ and for Reynolds numbers in the range of $20 \leq Re \leq 550$, the linear theory yields reliable estimates of the effective impedance of the stack. A distinctive feature of the impedance calculations in [5] is that they account for finite thickness effects. This is a crucial aspect since the 2D flow simulations indicate that the pressure drag exerted by the plate has a comparable magnitude to the friction force, even for stacks having long plates and blockage ratios as large as 0.9.

4.3 Validation and Analysis

Detailed computations have also been performed in order to establish the validity of the model predictions [6, 3, 8], and to analyze the limitations of linearized predictions.

A sample of these validation studies are provided in figure 4.2, which contrasts computed predictions and experimental measurements of the steady state temperature difference across an unloaded thermoacoustic stack. Good agreement is evident between the experimental results and the computations at all the values of the drive ratio considered. The computations are in excellent agreement with the predictions of the theory at low drive ratio, $Dr \leq 1\%$. However, as Dr increases, the predictions of the linear theory deviate significantly from both the experimental measurements and the computations. At moderate drive ratios, the deviation can be substantial, and exceeds 25% at a drive ratio of 0.02. In addition, as previously noted in [15], the theoretical estimates tend to overpredict ΔT at all stack positions, except in the neighborhood of the velocity node where the thermoacoustic effect naturally vanishes. Note that the computed stack position where ΔT peaks, $kx \sim 2.8$, coincides with the corresponding experimental measurement. On the other hand, the simulations and experiments are in slight disagreement with the linear theory, which predicts that the peak temperature difference occurs at $kx \sim 2.7$.

The distribution of the energy flux density in the neighborhood of the cold end of the stack is plotted in figure 4.3 for two values of the drive ratio. At $Dr = 0.5\%$, figure 4.3 shows that as they leave the cold end of the stack the energy pathlines rapidly curve around the corner and then follow an essentially straight path towards the hot end. Meanwhile, at $Dr = 2\%$, figure 4.3 shows that as they exit the end and side of the plate the energy pathlines first contour a large well-defined recirculation region before they enter into the channel. Thus, for the presently considered conditions, the mean energy path between the ends of the stack significantly increases with increasing drive ratio. This phenomenon, and to some extent the occurrence of a relatively important 2D motion within the gap, are the major effects of the increase in Dr and appear to be at the origin of the departure between the theory and the computations.

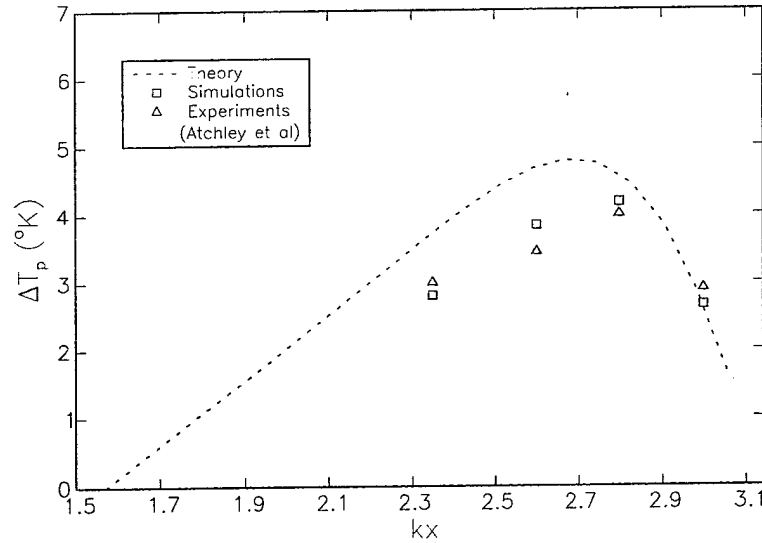
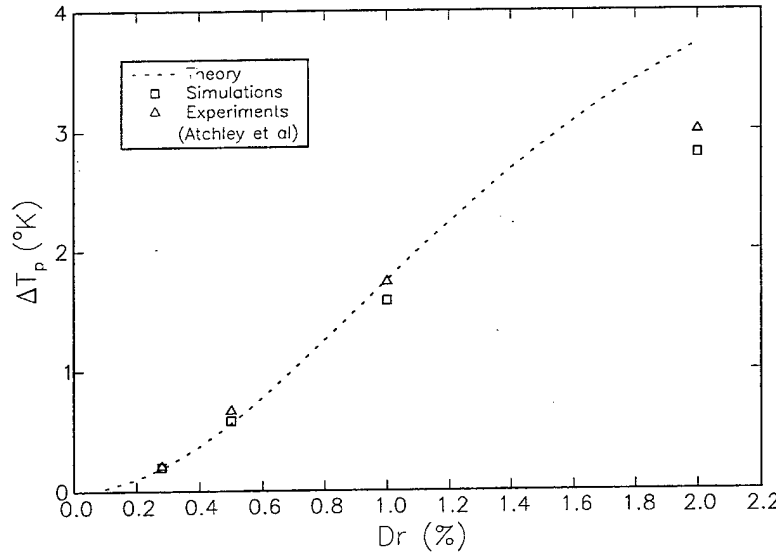


Figure 4.2: Top: Variation of temperature difference across the stack with drive ratio. The stack is located at $kx = 3\pi/4$. Bottom: Variation of temperature difference across the stack with position at $Dr = 2\%$. Experimental data are adapted from [15], and correspond to TAC # 3. The stack plates are a 0.1905-mm thick, laminate of stainless steel and fiberglass, with an effective thermal conductivity $\tilde{k}_s = 5.76 \text{ W/m}^\circ\text{K}$. The stack is 6.85-mm long with a half gap $\tilde{y}_0 = \tilde{h}/2 = 0.669 \text{ mm}$. Thus, the stack has a blockage ratio $h/H = 0.875$ and a plate length parameter of $L/H = 4.48$. The physical dimensions of the stack are approximated in the computations by using a blockage ratio $h/H = 0.837$ and a plate length parameter $L/H = 4.5$. Also shown are the predictions of the linear theory.

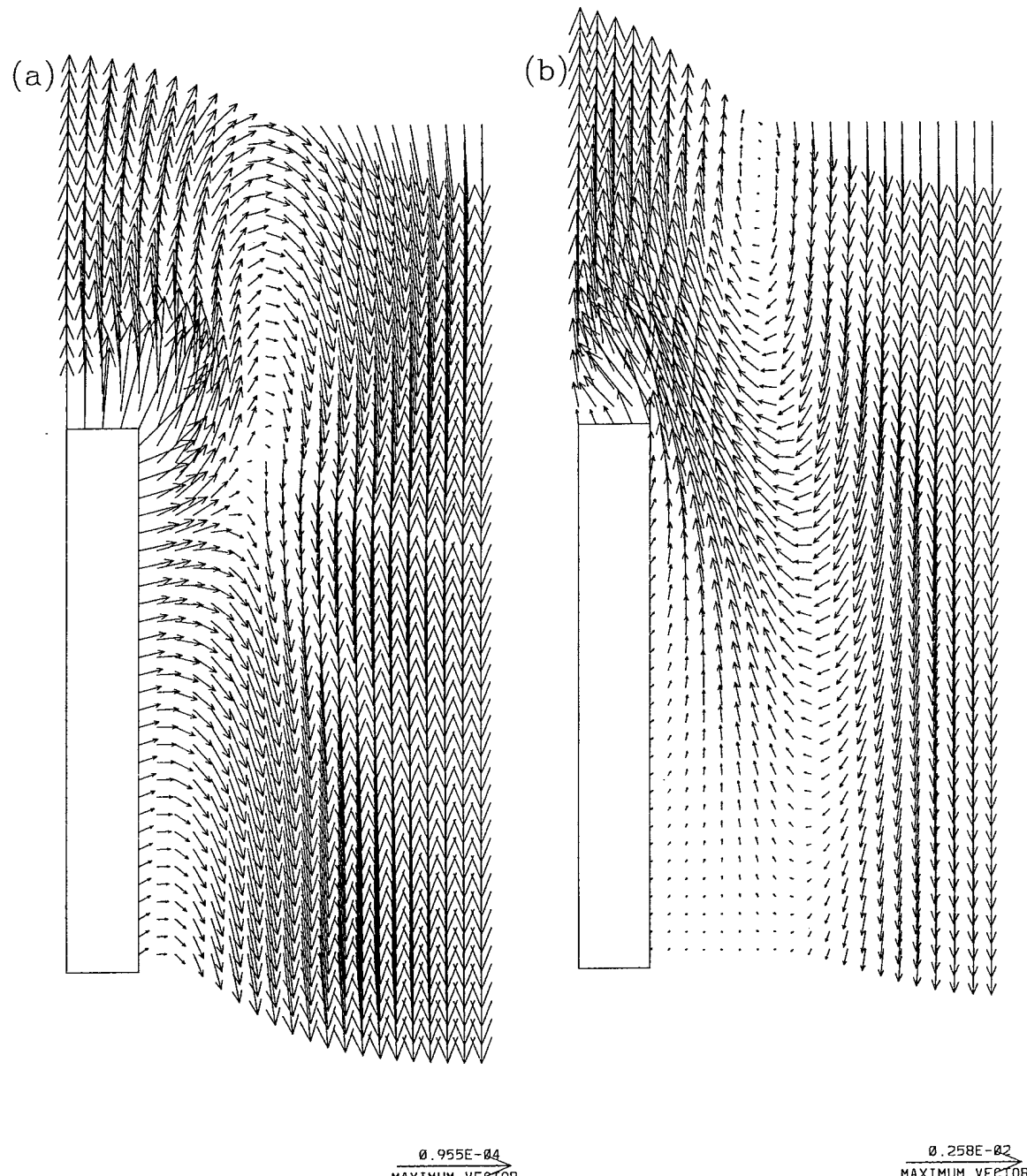


Figure 4.3: Vector map of the energy flux density near the cold end of the stack at $D\tau = 0.5\%$ (left) and $D\tau = 2\%$ (right).

Computations have also been performed in [8] to validate velocity field predictions. A sample of this validation study is provided in figures 4.4 and 4.5, which contrast computations and measurements of the instantaneous velocity field in the neighborhood of a stack edge.

As summarized in Table 4.1, two stack configurations are considered in the experiments [16]. In both cases, the center of the stack is located midway between the velocity node and the velocity anti-node, i.e. at a non-dimensional wave-number $kx = 3\pi/4$. In addition to the geometrical parameters of the stack, the computations use as input the thermal properties of the stack plates and of air, as well as the mean pressure and temperature, respectively $P_m = 10^5 \text{ N/m}^2$ and $T_m = 300^\circ\text{K}$. The experimentally-observed frequency of the resonant standing wave, $f = 200 \text{ Hz}$ is also used as input. Meanwhile, the amplitude of the standing wave is expressed in terms of the drive ratio, Dr , which expresses the ratio of the acoustic pressure amplitude to the mean pressure (Table 4.1).

The two stack configurations are geometrically similar, and are nearly equal in length. However, the thickness and spacing of the stack plates are significantly smaller in configuration A than they are in configuration B. These differences are also highlighted by providing the ratios h/δ_v and d/δ_v , where δ_v is the viscous penetration depth [17]. Thus, d is substantially larger than δ_v in configuration A, but is close to δ_v in configuration B. Accordingly, we shall refer to these two stacks as thick-plate and thin-plate configurations, respectively.

	d (mm)	h (mm)	L_p (mm)	Dr (%)	h/δ_v	d/δ_v
Configuration A	1.0	2.0	25.8	0.5	13.	6.5
Configuration B	0.15	1.0	24.0	1.5	6.7	1.0

Table 4.1: Geometric and flow parameters for configurations A and B.

Figure 4.4 depicts two instantaneous realizations of the velocity and vorticity fields for configuration A. Shown on the top row are experimental results obtained at $t_0 + T/4$ and $t_0 + 3T/8$; the bottom row depicts computational predictions obtained at $t_p + 3T/16$ and $t_p + 5T/16$. Thus, in both the experiments and computations the two frames are $T/8$ apart. Note that the frame of the computational results has also been restricted to match the $4.2 \times 4.2 \text{ mm}^2$ window of the PIV measurements [16].

For the present configuration, both the experimental and computational results reveal the presence of concentrated vortices near the edge of the plate. Also evident is the presence of both signs of vorticity, both inside the channel and in the open region. The generation of alternating layers of vorticity within the channel is not surprising, since the ratio of channel height to viscous penetration depth is large and the development of Stokes layers within the channel is accordingly expected. As can be observed in Figure 4.4, the vorticity distribution outside the channel can also exhibit complex structure, especially when separated vortices are driven back into the channel and impinge on the edge of the plates.

Comparison of the experimental and computational results in Figure 4.4 reveals a close correspondence between the predictions. In particular, at both phases, very good agreement can be observed between peak vorticity values as well as the size of the recirculating regions.

Figure 4.5 provides computed and experimental results obtained for configuration B. Shown on the left column are computed velocity and vorticity distribution at three selected phases within the cycle; plotted on the right columns are contours of the experimental vorticity distribution at the corresponding times. The figure is generated in a similar fashion as in Fig. 4.4, i.e. the computational test section is restricted so that it matches the experimental window. In the present case, the PIV measurements are performed in a $2.9 \times 2.3 \text{ mm}^2$ window, also located near the cold end of the stack.

The present predictions are thus in sharp contrast with earlier observations. Specifically, in the present case the results do not show the formation of well-defined eddies. The vorticity distribution in the wake exhibits the presence of elongated layers that extend well outside the channel. However, significant rollup of these layers is not observed, although evidence of very weak recirculating motion near the plate corners can be detected in the last computational frame.

Note that the top and bottom frames in Fig. 4.5 correspond to t_p and $t_p + T/2$, times at which the acoustic pressure is maximal and minimal, respectively. At these phases, the streamwise extent of the vortical wake, is

found to be maximal and the direction of the flow in the middle of the channel is opposite to that of the flow along the plate surface. As noted by Duffourd [16], these observations are in good qualitative agreement with the velocity profiles derived using the linear theory [17, 18] for the same configuration. The computed and measured velocities, which are in good agreement with each other, are slightly larger than those predicted by the theory. As discussed in [2], this discrepancy is most likely due to blockage effects which are ignored by the linear theory [2].

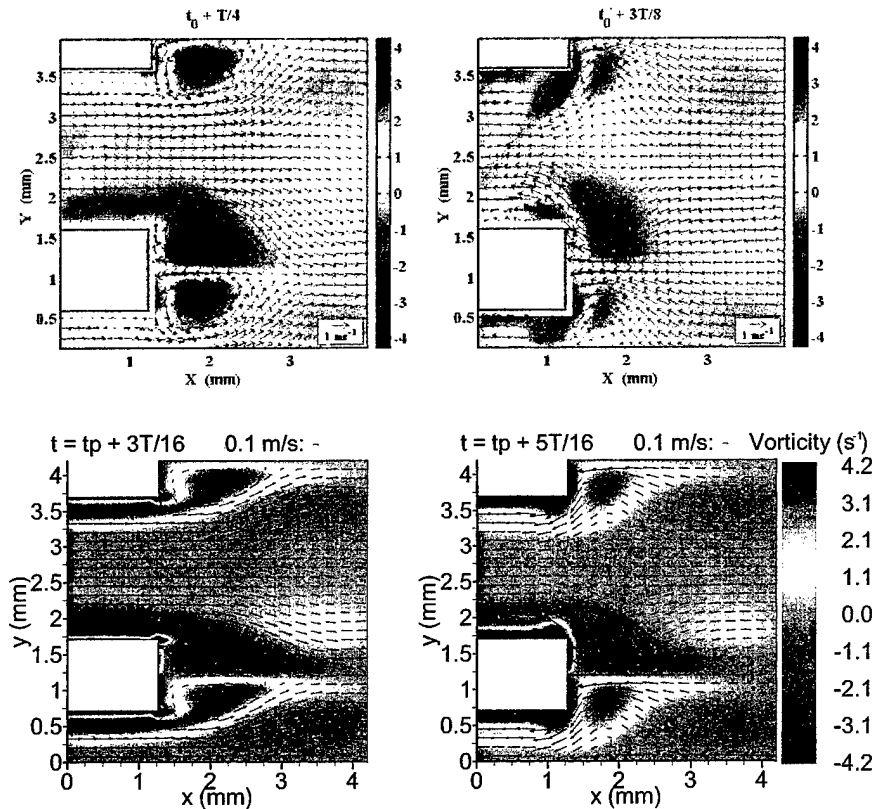


Figure 4.4: Instantaneous velocity (vectors) and vorticity (contours) fields around the cold end of the stack in configuration A. Top row: experimental PIV measurements; bottom row: computations. The times at which the frames are generated are indicated in the labels.

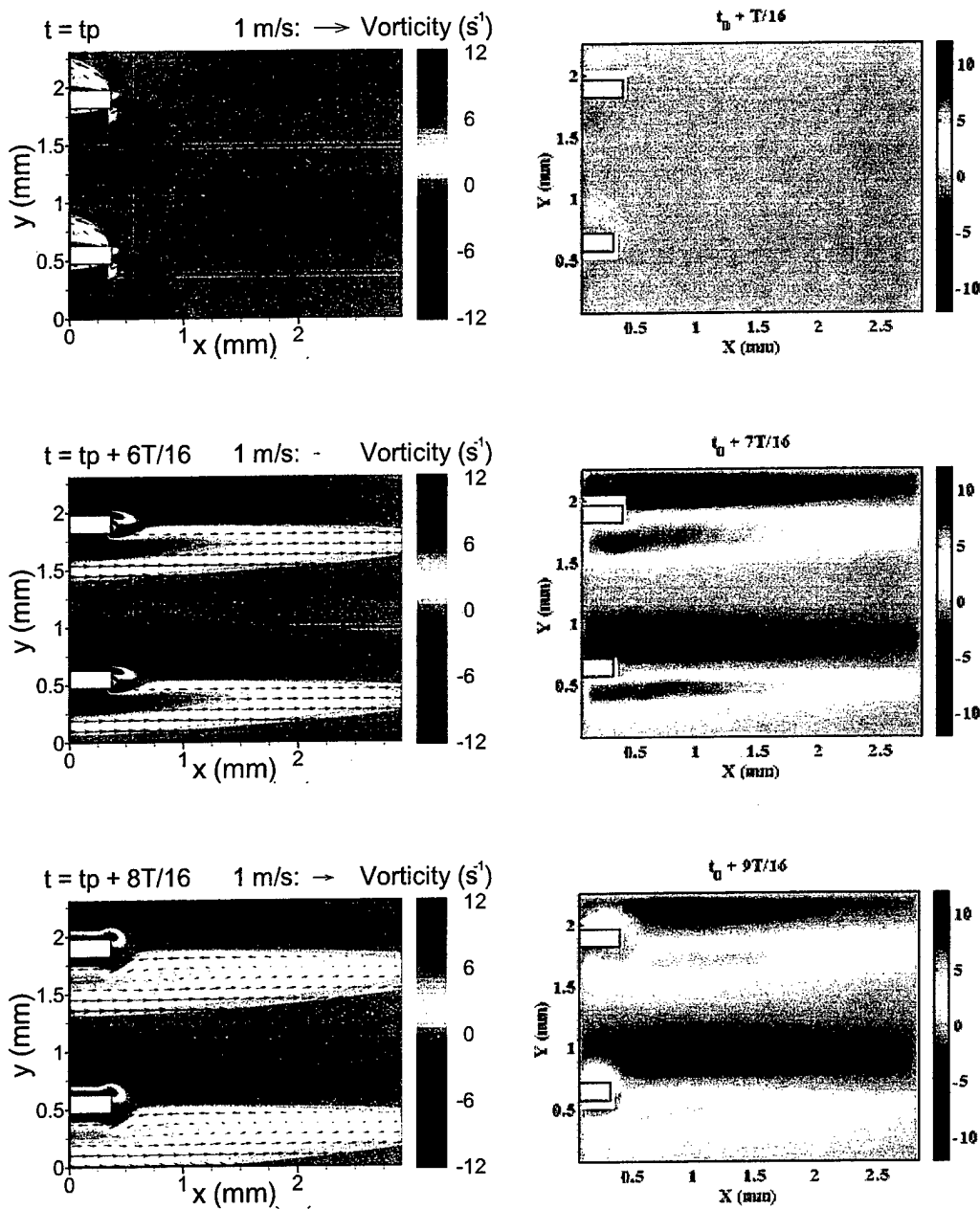


Figure 4.5: Left: Computed velocity (vectors) and vorticity (contours) fields at selected times for configuration B. Right: instantaneous vorticity contours from PIV measurements. The times at which the frames are generated are indicated in the labels.

4.4 Optimization of Heat Exchangers

A detailed study has been recently conducted in [8] of the effects of geometrical and operating parameters on the performance of the device. Specifically, a parametric study has been performed of the effect on the cooling load $\tilde{Q}_{m,f \rightarrow c}$ of drive ratio ($2\% \leq Dr \leq 8\%$), temperature difference between the hot and cold heat exchangers ($6 K \leq \Delta \tilde{T} \leq 21 K$), gap width \tilde{g} between the heat exchangers and the stack plates, heat exchanger length \tilde{L}_c , position of the stack in the resonance tube kx , thickness of the plates \tilde{d} , and plate spacing \tilde{h} .

Analysis of the computations revealed that the heat exchanger length, gap width, drive ratio, temperature difference between the heat exchangers, position of the stack in the resonance tube, heat exchanger and plate spacing have a combined effect on the performance of the device. More specifically, the cooling load has been found to peak at a well-defined combination of the gap width and heat exchanger length.

Two parameters, namely the optimal heat exchanger length and the optimal gap width, were independently determined. The optimal length varied only with the gap width and with the plate separation distance; it did not depend on any of the other parameters studied. On the other hand, the optimal gap width was independent of the drive ratio only. It became wider when (a) the temperature difference between the heat exchangers was increased, (b) the plates were stacked closer together. It also varied with the stack location in the tube.

The power density peaked when the plates were separated by a distance about 2.5 times the thermal penetration depth, and when the thickness of the plates was slightly smaller than the thermal penetration depth. With thinner or thicker plates, the power density dropped sharply.

Detailed analysis has also been performed in [8] of the impact of proper optimization of heat exchanger parameters. In particular, it has been shown that the cooling load fluctuates above 90% of its maximal value whenever the length of the heat exchangers fell within $0.8 \leq L_{h/c}/(2.R_p + \delta_k) \leq 2$. For shorter heat exchangers, the cooling dropped sharply.

In addition, the optimization study also showed that the gap width between the heat exchangers the stack plates should be accurately selected. The introduction of a finite gap between the stack plates and heat exchangers can lead to a significant increase in the cooling load. Specifically, for a large temperature difference between the heat exchangers, optimization of the gap width was shown to have a dramatic impact on the cooling load and the thermal performance of the device.

Appendix

Nomenclature

Roman

BR	Blockage ratio ($\equiv (\tilde{H}/(\tilde{H} - \tilde{d}))$)
Dr	Drive ratio ($\equiv \tilde{P}_0/\tilde{P}_m$)
D/Dt	Material derivative ($\equiv \partial/\partial t + \mathbf{u} \cdot \nabla$)
Ec	Eckert number ($\equiv \tilde{\rho}_m/(\tilde{C}_p\tilde{T}_m)$)
H	Stack centerline spacing
L_o	Normalizing parameter ($\equiv 2R_p + \delta_k$)
L_p	Length of the stack plates
L_g	Length of the gap between the stack and each heat exchanger
$L_{h/c}$	Length of the hot/cold heat exchangers
P	Thermodynamic pressure
Pe	Peclet number ($\equiv \tilde{\rho}_m \tilde{\Omega} \tilde{H}^2 C_p / k$)
Pe_s	Peclet number for the plate ($\equiv \tilde{\Omega} \tilde{H}^2 / \tilde{\alpha}_s$)
Pr	Prandtl number ($\equiv \tilde{\mu} \tilde{C}_p / \tilde{k}$)
$Q_{c \rightarrow f}$	Heat transfer from the cold heat exchanger to the gas
R	Specific gas constant
Re	Reynolds number ($\equiv \tilde{\Omega} \tilde{H}^2 / \tilde{\nu}$)
Re_a	Acoustic amplitude Reynolds number ($\equiv \tilde{u}_a / \sqrt{\tilde{\nu} \tilde{\Omega}}$)
R_p	Particle displacement parameter ($\equiv \tilde{u}_a / \tilde{\Omega} \tilde{H}$)
T	Temperature
V	Volume of the computational domain
d	Stack and heat exchanger thickness
g	Spacing between stack and heat exchangers
h	Stack gap ($\equiv 2.y0$)
kx	Dimensionless wave number ($\equiv \tilde{\Omega} \tilde{x} / \tilde{c}$)
p	Hydrodynamic pressure
n	Outward normal to the boundary of the computational domain
t	Time
t_p	Time at which the pressure rate of change is minimal
\mathbf{u}	Velocity vector

Greek

Φ	Viscous dissipation
α	Thermal diffusivity ($\equiv \tilde{k}/(\tilde{\rho} \tilde{C}_p)$)
∂D	Boundary of the computational domain
ϕ	Velocity potential
γ	Specific heat ratio
κ	Ratio of gas thermal conductivity to plate thermal conductivity

ψ	Streamfunction
ρ	Density
ζ	Vorticity

Subscripts

a	Acoustic
c	Cold heat exchanger
f	Fluid
h	Hot heat exchanger
m	Mean
s	Solid

Superscripts

\sim Dimensional quantity

Dimensional variables

\tilde{C}_p	Isobaric specific heat ($\text{J kg}^{-1} \text{ K}^{-1}$)
\tilde{k}	Thermal conductivity ($\text{J m}^{-1} \text{ s}^{-1} \text{ K}^{-1}$)
\tilde{P}_0	Pressure amplitude (N/m^2)
\tilde{c}	Speed of sound (m/s)
$\tilde{\Omega}$	Angular frequency of the standing wave (rad/s)
$\tilde{\delta}_v$	Viscous penetration depth in the fluid (m) ($\equiv \sqrt{2\tilde{\nu}/\tilde{\Omega}}$)
$\tilde{\delta}_k$	Thermal penetration depth in the fluid (m) ($\equiv \sqrt{2\tilde{\alpha}_f/\tilde{\Omega}}$)
$\tilde{\delta}_p$	Nominal plate thickness (m)
$\tilde{\nu}$	Kinematic viscosity ($\text{N}\cdot\text{m/s}$)
$\tilde{\lambda}$	Wavelength of the standing wave (m)
\tilde{u}_a	local velocity amplitude ($\equiv \tilde{c}Dr\sin(kx)/\gamma$)

Mathematic Operators and Indexes

∇	Nabla Operator, $= \left(\frac{\partial}{\partial x}, \frac{\partial}{\partial y}, \frac{\partial}{\partial z} \right)^T$
\circ	Dyadic Product
\cdot	Scalar Product
Δt	Time step
Δx	Mesh size in the x-Direction
Δy	Mesh size in the y-Direction

Bibliography

- [1] A.S. Worlikar. Numerical study of unsteady flow around a thermoacoustic stack. S.m. thesis, The Johns Hopkins University, 1995.
- [2] A.S. Worlikar and O.M. Knio. Numerical simulation of a thermoacoustic refrigerator. part i : Unsteady adiabatic flow around the stack. *J. Comput. Phys.*, 127:424–451, 1996.
- [3] A.S. Worlikar, O.M. Knio, and R. Klein. Numerical simulation of thermoacoustic refrigerator part ii: Stratified flow around the stack. *J. Comput. Phys.*, 144:299–324, 1998.
- [4] A.S. Worlikar and O.M. Knio. Numerical study of oscillatory flow and heat transfer in a loaded thermoacoustic stack. *Numerical Heat Transfer, Part A*, 35:49–65, 1999.
- [5] A.S. Worlikar, O.M. Knio, and R. Klein. Numerical study of the effective impedance of an idealized thermoacoustic stack. *Acustica*, 85:480–494, 1999.
- [6] A.S. Worlikar. Numerical simulation of thermoacoustic refrigerators. Ph.d. thesis, The Johns Hopkins University, 1997.
- [7] E. Besnoin and O.M. Knio. Numerical study of thermoacoustic heat exchangers in the thin plate limit. *Numerical Heat Transfer*, 45:445–471, 2001.
- [8] E. Besnoin. Numerical study of thermoacoustic heat exchangers. Ph.d. thesis, The Johns Hopkins University, 2001.
- [9] A. Majda and J. Sethian. The derivation and numerical solution of the equations for zero mach number combustion. *Combust. Sci. Tech.*, 42:185–205, 1985.
- [10] H. Schlichting. *Boundary Layer Theory*. McGraw-Hill Inc., 1987.
- [11] P. Merkli and H. Thoman. Transition to turbulence in oscillating pipe flow. *Journal of Fluid Mechanics*, 68:567–576, 1975.
- [12] N. Cao, J.R. Olson, G.W. Swift, and S. Chen. Energy flux density in a thermoacoustic couple. *J. Acoust. Soc. Am.*, 99:3456–3464, 1996.
- [13] C.A.J. Fletcher. *Computational techniques for fluid dynamics*. Wiley, New York, 1987.
- [14] C. Hirsch. *Numerical computation of internal and external flow*. Wiley, New York, 1989.
- [15] A.A. Atchley, T.J. Hofler, M.L. Muzzeral, M.D. Kite, and C. Ao. Acoustically generated temperature gradients in short plates. *J. Acoust. Soc. Am.*, 88:251–263, 1990.
- [16] S. Duffourd. Refrigerateur thermoacoustique: etudes analytiques et experimentales en vue d'une miniaturisation. Ph.d. thesis, Ecole Centrale de Lyon, 2001.
- [17] G.W. Swift. Thermoacoustic engines. *J. Acoust. Soc. Am.*, 84:1145–1180, 1988.
- [18] H. Bass W.P. Arnott and R. Raspot. General formulation of thermoacoustics for stacks having arbitrarily shaped pore cross sections. *J. Acoust. Soc. Am.*, 90:3228–3237, 1991.

**THERMO-FLUID MECHANIC STUDY OF
THERMOACOUSTIC DEVICES
- EXPERIMENTAL EFFORTS -**

Final Report

April 2002

Co-Investigator

Dr. Cila Herman, Associate Professor

Heat Transfer Lab

Department of Mechanical Engineering

The Johns Hopkins University

Phone: (410) 516 4467, Fax: (410) 516 7254

E-mail: herman@titan.me.jhu.edu

Grant #: N00014-94-1-0063

ONR Program Officer: Logan Hargrove

1. SUMMARY

Long-term research objective: The long-term objective of this component of the study is the experimental investigation of heat transfer in the thermoacoustic stack and heat exchangers with the purpose of developing better models and designs of heat exchangers.

Technical and research objectives: The heat exchangers of a thermoacoustic refrigerator deliver the heat absorbed in the refrigerated volume to the cold side of the thermoacoustic stack and absorb the heat transported from the cold to the hot side of the stack, which is then released to the ambient. Improving their performance is key to improving the overall performance of thermoacoustic refrigerators. Only few studies reported in the literature focus on the modeling and design of heat exchangers for thermoacoustic devices.

Technical approach: The approach taken on our research is to first visualize and measure the high-speed oscillating temperature fields in the thermoacoustic stack using holographic interferometry combined with high-speed cinematography. Results of the heat transfer measurements, specifically the measured heat transfer coefficients were used as input data for the models that were developed to analyze the performance of thermoacoustic heat exchangers.

Publications: During the past years 6 papers were published in peer-reviewed journals (J1-J6, attached), one paper (J7) was accepted and two are in preparation (J8 and J9). One invited book chapter on heat transfer in oscillatory flow was completed (B2, attached) as well as one on heat transfer enhancement of heat exchangers (B1). A contribution was made to the Dictionary of Acoustics (B3). Six papers were published in proceedings of conferences (C1-C6) as well as nine abstracts in conference proceedings (C7-C15). The research has resulted in one dissertation (D1), two Master's degrees and 7 European diploma degrees equivalent to a Master's degree in collaboration with universities from Europe.

Presentations: The work has been presented at 14 conferences and at 31 invited lectures in the USA, Switzerland, Turkey, France and Germany. Two invited lectures will be given at the NATO Advanced Study Institute on *Low-temperature and Cryogenic Refrigeration* to be held this summer in Cesme, Turkey. One of the objectives of the research program was to familiarize the engineering and especially heat transfer community with thermoacoustic refrigeration. This goal was accomplished by presenting the results of this research at mechanical engineering conferences and by giving seminars at research labs, institutions and universities in the United States and Europe.

Organization of conference sessions: A session on *Emerging Refrigeration Technologies* and one on *Transport Phenomena in Oscillatory Flows* was organized by Cila Herman and Omar Knio at the *National Heat Transfer Conference in Baltimore, August 10-12, 1997*. Seven papers were submitted for the sessions and four of the presentations focused on thermoacoustics. The papers were published in the proceedings of the conference, AIChE Symposium Series, Volume 93, 1997, Mohamed S. El-Genk, Volume Editor. Two session with a similar topics were organized at the *National Heat Transfer Conference in Albuquerque, New Mexico, Aug. 15-19, 1999*. Cila Herman and Martin Wetzel organized the *Special Session on Thermoacoustics* (2 sessions, 6 invited lectures, 16 papers) at the *137th Meeting of the Acoustical Society of America and the 2nd Convention of the European Acoustics Association* held March 13-17, 1999 in Berlin, Germany.

Impact/Navy relevance: The Navy is interested in efficient, environmentally safe large-scale and small-scale refrigeration systems, for example for air-conditioning, cooling of food or electronic equipment, etc. The development of more efficient heat exchangers can lead to smaller, lighter and more efficient thermoacoustic refrigerators, which is of particular importance in systems where size and weight is critical. Systematic design optimization tools are essential in commercial applications. Miniature thermoacoustic refrigerators (MEMS) are a potential solution for a range of practical applications.

Technology transfer: The two design optimization algorithms developed for the project were used to evaluate the performance of the miniature thermoacoustic refrigerator for electronic cooling applications and improve its design for a project carried out with Rockwell Science Corporation, CA. A series of lectures was given at the Universite Pierre et Marie Curie (Paris 6), Ecole Centrale Lyon and Ecole Centrale Paris in France as well as the University of Hannover in Germany. The French army and industry in France and Germany showed great interest in thermoacoustic refrigeration technology. Copies of papers were distributed to scientists in Europe.

2. RESEARCH ACCOMPLISHMENTS

The theory, research and applications of heat transfer equipment, such as thermoacoustic refrigerators or heat exchangers for thermoacoustic refrigerators, involve a variety of tasks and problems. In general, two fundamentally different tasks can be distinguished both from the engineering as well as theoretical point of view; namely the design problem and the performance prediction. The first task, the design problem, which is frequently called the sizing problem, deals with a design of a new device for a specific set of input data specified by operating, thermophysical and material parameters as well as geometry constraints. The second task, the performance analysis or rating problem, involves the analysis and prediction of the performance

of a device. Sometimes, the performance problem is treated as the performance sensitivity analysis. This term emphasizes the fact that the prediction also focuses on the performance of a system under conditions away from the operating point for which the device was originally designed.

An effective design of heat transfer equipment typically involves optimization; the choice of the optimization method and the performance criteria depends on the specific character of a device, optimization function and constraints. Optimization methods were frequently implemented to design one of the most widespread classes heat transfer equipment, the heat exchangers. One of the oldest optimization methods is the "Least-Material Optimization" was described by Eckert, Drake, 1950 (*Introduction to the transfer of heat and mass*, McGraw-Hill, New York, 1950, pp. 32-34). Similarly, "Least-Volume Optimization" or "Optimization for Minimum Flow Resistance" can be used, as discussed by Bejan, 1995 (*Convection heat transfer*, John Wiley & Sons, Inc., New York, 1995, p.132, 139, 202). Thermodynamic optimization methods are based on the minimization of enthalpy exchange irreversibility (Bejan, *The concept of irreversibility in heat exchanger design: Counterflow heat exchangers for gas-gas applications*, J. Heat Transfer, Trans. ASME, 99, 1977, pp. 374-380; Sekulic and Herman, *One approach to irreversibility minimization in compact crossflow heat exchanger design*, Int. Com. Heat Mass Transfer, 13, 1986, pp. 23-32) and on the entropy generation minimization (Bejan, *Entropy generation through heat and fluid flow*, John Wiley & Sons, New York, 1982; Bejan et al., *Thermal design and optimization*, Wiley, New York, 1996; and Bejan et al., *Thermodynamic optimization of geometry: T- and Y-shaped constructs of fluid streams*. Int. J. Therm. Sci., 39, 2000, pp. 949-960). There are numerous additional influences that can affect the design, such as economic criteria (initial or operating or total costs) as well as the limitations imposed by the available technologies ("Design for Manufacturability" - see Iyengar, Bar-Cohen, *Design for manufacturability of SISE parallel plate forced convection heat sinks*, 7th Inter Society Conference on Thermal Phenomena, Therm 2000, Las Vegas, May 2000, pp. 141-148).

However, the field of thermoacoustic refrigeration as well as the design of ThermoAcoustic Refrigerators (TAR) is rather young, in particular when compared with the heat exchanger tradition, thus spectrum of optimization methods for TAR is quite limited. Often, TAR design is supported by experience and intuition, which are the two main sources for the designer's ad hoc choices. A performance analysis in a step following the design process verified an initiation estimate (e.g., Hofler, 1986). Both steps, the design problem and performance analysis, are typically repeated in an iterative cycle when optimization of system performance is necessary. Sometimes a new design can be supported by the knowledge of previous devices or designs, and represents an incremental modification of a well-tested solution (e.g. Garrett's approach, 1991, who used an experimental experience by Hofler, 1986). Another optimization attempt where a cost function of performance was minimized using the simplex method, was proposed by Minner et al. (1995). Recently, a design optimization algorithm was developed by Wetzel and Herman (1997), where the coefficient of performance was used as a criterion of the performance of the thermoacoustic core.

The heat transfer research carried out in the Heat Transfer Lab of the Johns Hopkins University focused on the following issues:

2.1 DESIGN OPTIMIZATION OF THERMOACOUSTIC REFRIGERATORS FOR MAXIMUM COEFFICIENT OF PERFORMANCE (COP) (Ref. J1)

The coefficient of performance and coefficient of performance compared to Carnot's (*COP* and *COPR*, respectively) play an important role in a design of the TAR. The first major achievement of our research is the development of the systematic design and optimization algorithm for thermoacoustic refrigerators (Wetzel and Herman, 1997) that relies on the first law of thermodynamics and maximizes the COP or COPR. This algorithm is based on new scaling arguments that allowed significant simplification of the existing theory by reducing the number of design parameters from 19 dimensional parameters to 10 nondimensional parameters, using the simplified linear model of thermoacoustics, the short stack boundary layer approximation. The methodology is based on the first law of thermodynamics. The analysis suggests a separate optimization of the four main modules of the thermoacoustic refrigerator: (i) thermoacoustic core (consisting of the stack plates and the working fluid between the stack plates), (ii) resonance tube, (iii) heat exchangers and the (iv) acoustic driver. An upper limit on the thermoacoustic refrigerator's performance is set by the heat pumping capacity of the thermoacoustic core. Calculations of the thermoacoustic core's performance indicate that thermoacoustic refrigeration can achieve COPRs competitive to commercially available refrigeration systems, and predict up to 40-50% of Carnot's efficiency for the thermoacoustic core. The design optimization algorithm introduced in Ref. J1 provides fast and simple engineering estimates that are essential for the development of prototypes. This is particularly important nowadays, when commercial applications are sought. A copy of the paper, Ref. J1, is attached.

2.2 DESIGN OPTIMIZATION OF THERMOACOUSTIC REFRIGERATORS FOR MAXIMUM COOLING LOAD (Ref. J8)

Although use of the *COP* and *COPR* as the performance criterion is thermodynamically correct and the importance of these criteria obvious, both COP and COPR are relative parameters, and therefore have to be used with caution. Recent studies focusing on the design of a thermoacoustic refrigerator for the thermal control of electronics have shown that the design optimization can require an absolute criterion (Travnicek and Herman, 2002, Ref. J8). A reason for this is that a TAR with relatively high *COP* as well as *COPR* (both are desirable) can have rather small cooling load, which is unacceptable in some applications. Hence the cooling load of the TAR (Q_C) was chosen as the criterion for optimizing a TAR by maximizing the Q_C . Theoretically, this approach is based on the knowledge that the maxima in *COP* and Q_C do not coincide. However, both *COP* and Q_C can be large for a relatively wide range of system parameters, as pointed out by Swift (1988, p.1171) for the thermoacoustic engine (prime mover) and for the corresponding pair of relative and absolute parameters, i.e. "engine efficiency" and "extracted work flux", respectively.

The TAR optimization methodology based on the maximization of Q_C developed in the Heat Transfer Lab of the Johns Hopkins University by Z. Travnicek and C. Herman appears to be a logical and adequate approach in a wide range of applications. Moreover, the requirement of high Q_C -values is intuitively and automatically taken into account by the designer. A paper describing this design methodology is currently in preparation (Ref. J8).

2.3 HOLOGRAPHIC INTERFEROMETRY IN THE VISUALIZATION AND MEASUREMENT OF HIGH-SPEED, UNSTEADY TEMPERATURE FIELDS IN THE VICINITY OF THE THERMOACOUSTIC STACK (Refs. J2, J3, J4)

Temperature measurement by holographic interferometry in the presence of pressure variations (Refs. J2, J3 and J4)

In order to quantitatively reconstruct the temperature distributions in the region of the thermoacoustic stack, it was necessary to develop a new algorithm for the evaluation of the interference fringe patterns generated by HI to obtain accurate data in the presence of pressure variations. The algorithms that were previously described in the literature do not account for the pressure variations. Thus, by developing two new evaluation algorithms, we have expanded the applicability of HI to temperature measurements in situations where pressure variations accompany the temperature oscillations. Copies of the papers describing the measurement and reconstruction techniques, Refs. J2, J3 and J4, are attached.

Improving the accuracy of temperature measurements by holographic interferometry by using temperature as tracer (Ref. J3)

We have also shown that it is possible to enhance the spatial resolution and accuracy of interferometric measurements by imposing a steady-state temperature distribution to the oscillating flow. The latter technique can be considered as using temperature as tracer to resolve the small, time dependent temperature fluctuations in the acoustic field. A copy of the paper, Ref. J3, is attached.

2.4 EXPERIMENTAL STUDY OF THERMOACOUSTIC EFFECTS ON A SINGLE STACK PLATE: TEMPERATURE FIELDS AND HEAT TRANSFER (Refs. J5 and J6)

Experiments with the modular thermoacoustic refrigerator

Experiments were carried out with a modular thermoacoustic refrigerator to study the thermal performance of the stack region. To investigate the influence of key parameters of the thermoacoustic refrigerator on heat transfer, we built a modular thermoacoustic refrigerator based on the design algorithm developed by Wetzel and Herman (1997-J1) which represents the design parameters in dimensionless form. Introducing dimensionless design parameters has the advantage that the results are not restricted to one particular experimental/hardware configuration. Additionally, the approach allows comparison with existing designs and reduces the number of experiments that need to be conducted. The modular structure of the refrigerator allows easy modification of stack and heat exchanger geometries, such that the influence of the different system parameters on the heat transfer can be investigated.

In addition to conventional sensors, HI combined with high-speed cinematography was applied as measurement technique, as described in Section 2.3. The main advantage of this approach is that it allows high spatial (up to 2700 dpi) and high temporal resolutions (up to 0.1ms). Thus it represents the ideal tool to investigate the temperature fields in a thermoacoustic refrigerator that oscillate with frequencies of a few hundred hertz.

We designed and built three stacks for the modular thermoacoustic refrigerator. Stack 1 was used for temperature measurements with thermocouples as well as HI. Stack 2 was identical in its dimensions and instrumentation to stack 1, but had copper strips that act as heat exchangers attached at both ends. Stack 3 was also identical in its dimensions to stack 1, but instead of

thermocouples it was equipped with a pressure transducer. The pressure transducer measures pressure at the stack center position. All three stacks were movable within the resonance tube, and therefore temperature and pressure measurements for different stack center positions could be performed. By conducting temperature measurements with stacks 1 and 2, the effect of the heat exchangers on the temperature distributions was investigated. Pressure measurements with stack 3 allow quantifying the effect of the stack on the acoustic standing wave. The pressure distribution along the acoustic standing wave can be determined by measuring the pressure at different locations along the resonance tube with a second pressure transducer.

Visualization and measurement of the oscillating temperature fields at the edge of the thermoacoustic stack plates (Refs. J5 and J6)

The second major achievement of the experimental part of the project is the measurement of oscillating temperature fields as well as heat fluxes in a thermoacoustic refrigerator model using a combination of real-time holographic interferometry (HI) and high-speed cinematography. The thermal interaction between a heated solid plate and the acoustically driven working fluid was investigated in the Heat Transfer Laboratory of the Johns Hopkins University by visualizing and quantifying the temperature fields in the neighborhood of the solid plate. With these experiments the thermoacoustic effect was visualized for the first time. The measurements the existence of high time-averaged local heat fluxes at the edge of the stack plates, as predicted by numerical and theoretical treatments of the problem. A better knowledge of these temperature fields is essential to develop systematic design methodologies for heat exchangers in oscillatory flows.

Key results of these studies were reported in two papers, refs. J5 and J6 (attached). The difference between heat transfer in oscillatory flows with zero mean velocity and steady flows is discussed in the papers. In the experiments, the thermoacoustic effect was visualized through temperature measurements. A novel evaluation procedure that accounts for the influence of the acoustic pressure variations on the refractive index was applied to accurately reconstruct the high-speed, two-dimensional oscillating temperature distributions. Heat fluxes close to the edge of a heated solid plate aligned parallel to the axis of the acoustic standing wave were measured for drive ratios $DR \equiv P_A / P_m$ of 1, 2 and 3%. At the highest drive ratio (3%), the resulting heat flux vector at the edge of the plate is directed into the plate, opposite to the direction of the heat flux imposed by the resistive heaters within the plate. This observation confirms the thermoacoustic effect previously discovered in the visualized temperature fields. Through the energy balance the magnitudes of the heat fluxes into the plate, caused by the thermoacoustic effect, were determined. The measured data are in good agreement with numerical and analytical predictions.

2.5 IMPACT OF FLOW OSCILLATIONS ON CONVECTIVE HEAT TRANSFER (Ref. B2)

Flow oscillations and their impact on heat transfer from solid surfaces play a key role in the modeling and performance of heat exchangers for thermoacoustic applications. A review paper in the form of a book chapter, discussing the impact of flow oscillations on heat transfer in self-sustained oscillatory flows, jets and some acoustically driven flows was prepared (Ref. B2, attached).

2.6 A SIMPLIFIED MODEL OF HEAT TRANSFER IN PARALLEL CHANNEL HEAT EXCHANGERS AND STACK PLATES OF THERMOACOUSTIC DEVICES (Ref. J7)

The heat exchangers of a thermoacoustic refrigerator deliver the heat absorbed in the refrigerated volume to the cold side of the thermoacoustic stack and absorb the heat transported from the cold to the hot side of the stack, which is then released into the ambient. To improve the performance of the heat exchangers, it is essential to gain better insight into the thermoacoustic heat transfer process. So far, neither theoretical nor numerical models are available that can accurately predict the overall heat transfer performance of heat exchangers as part of thermoacoustic devices (numerical results regarding temperature and velocity distributions around the stack plates were reported in the literature) and their influence on the overall performance of the TAR. Therefore, one of the goals of the project involved quantifying thermoacoustic heat transfer in the heat exchangers in a combined modeling and experimental effort.

Standard heat exchanger design methods are available for conventional applications (steady forced convection) for a wide range of heat exchanger designs, flow arrangements and working fluids. Up to date it has not been evaluated to which extent conventional methods are suitable for the design of heat exchangers operating in oscillatory flows with zero mean velocity. Currently it is being explored if it is feasible to modify existing methods as opposed to developing new models and methods suitable for predicting the behavior thermoacoustic heat exchangers. The theoretical analysis will provide information on the experimental data, regarding both heat transfer and pressure drop, that are necessary for the design and modeling of the heat exchangers. Finally, the heat exchanger models will be incorporated into the optimization algorithm described in J1.

Mathematical models of the thermal behavior of several types of heat exchangers were developed for: (i) the parallel flat-channel heat exchanger using a liquid as the transport fluid (J7), (ii) the simple, parallel-fin heat exchanger that relies on heat conduction as well as (iii) 2D computational models for several, more complex heat exchanger configurations.

A simplified model of heat transfer in parallel channel heat exchangers and stack plates of thermoacoustic devices was developed. The model took advantage of previous results regarding the thermal behavior of the thermoacoustic core and the measurements of local heat transfer at the edge of the stack plates for investigations of the performance of heat exchangers attached to the thermoacoustic core. Geometrical and operational parameters as well as thermophysical properties of the heat exchangers, the stack plate, and the working fluid were organized into dimensionless groups that allowed accounting for their impact on the performance of the heat exchangers. Numerical simulations were carried out with the model. Nonlinear temperature distributions and heat fluxes were observed near the edge of the stack plate. Effects of different parameters on the thermal performance of the heat exchangers were investigated.

2.7 DEVELOPMENT OF A SIMPLIFIED MODEL OF THE HEAT EXCHANGERS RELYING ON HEAT CONDUCTION – PARALLEL STRIP HEAT EXCHANGERS (Ref. J9)

The simple, parallel fin heat exchanger design that relies on heat conduction to transport heat to and from the thermoacoustic core delivers satisfactory heat transfer rates for smaller thermoacoustic refrigerators because of the small cross sectional area of the resonance tube. The mechanism of heat transfer along the fins is conduction. The conductive resistances of the fins scale with the fin length, and are small for miniature systems. This solution for the design of the heat exchangers offers the advantage of simplicity, it eliminates the problem of sealing at the locations where the pipe with the heat exchanger liquid enters the resonance tube and the manufacturing of the heat exchanger hardware is easier than for heat exchangers that use liquids.

In the first step we assume that the temperature of the heat exchanger fin is uniform along the acoustic axis x . This assumption is justifiable: the thermal conductivity of the fin material (typically copper) is high and the dimension along the acoustic axis is small. The steady state temperature distribution along the fin was determined analytically and numerically. Heat transfer from the oscillating flow (with zero mean velocity) is described by means of an equivalent constant heat transfer coefficient h (measured, numerically determined or estimated values were used in the calculations). The ring that spans the heat exchanger fins is assumed to be at the ambient temperature, which corresponds to the temperature of the fin base. The solution of the model yields temperature and heat flux distributions in the heat exchangers. Initially a solution for a single fin (the longest one) was determined; temperature distributions in the shorter fins were found using appropriate scaling.

2.8 DESIGN OF A MINIATURE THERMOACOUSTIC REFRIGERATOR FOR ELECTRONIC COOLING APPLICATIONS (Ref. J9)

Design issues were considered that influence the performance of miniature thermoacoustic refrigerators with application to the cooling of electronic equipment. In the design optimization process the design objective was to maximize the cooling load. It was found that the design that maximizes the cooling load is not identical to the design that maximizes the coefficient of performance of the system, COP. It was found that Helium as working fluid will have the highest cooling load. The influence of the geometry and thermophysical parameters on the performance of the thermoacoustic refrigerator was studied systematically and a performance sensitivity analysis was carried out. Key results are being summarized in a paper by Travnicek and Herman (2002), Ref. J9.

2.9 INCORPORATION OF HEAT EXCHANGER MODELS INTO THE DESIGN OPTIMIZATION ALGORITHM BY WETZEL AND HERMAN (1997)

The models of the heat exchangers will be incorporated into the design optimization algorithms developed by *Wetzel and Herman (1997)*, Ref. J1, and *Travnicek and Herman (2001)*, Ref. J9, to allow the quantification of the impact of heat exchangers on the overall performance of thermoacoustic devices. Performance limitations of miniature thermoacoustic refrigerators will be evaluated.

2.10 FUTURE WORK

Measurement of temperature and velocity profiles within the viscous and thermal penetration depths

One major research issue that needs to be addressed is to experimentally determine the time dependent temperature and velocity profiles within the thermal and viscous penetration depths, respectively. This knowledge is important for two reasons. First, practical thermoacoustic devices will most likely operate in non-linear regimes. Therefore, it is necessary to identify the influence of non-linear effects on the phasing between temperature and velocity within the thermal penetration depth, since it is this phasing that generates the hydrodynamic transport of heat along the stack plates. Second, in order to accurately measure the time dependent heat fluxes within the stack and the heat exchangers in thermoacoustic devices, it is essential to accurately determine the derivative of the temperature profile near the solid boundary. It is planned to acquire a Laser Doppler Anemometer to measure the velocity profile within the viscous penetration depth.

The data obtained in these experiments will be compared quantitatively to results of numerical simulations (obtained by Omar Knio, for example) to verify the numerical model. It is expected that the numerical model will provide fundamental data necessary for the optimization of heat exchangers. However, comparisons with experimental data will be necessary after any significant change in the numerical algorithm or physical model.

Development of a micro heat pipe serving as heat exchanger in thermoacoustic refrigerators

Apart from conventional heat exchangers heat pipes can also be implemented to remove heat from the refrigerated volume and deliver it to the thermoacoustic refrigerator. Heat pipes offer the advantage of being passive devices, which makes them particularly suitable for applications where high reliability is essential. A micro-heat pipe serving as heat exchanger will be designed and built based on the information regarding pressure, velocity and temperature distributions obtained experimentally.

Improving the design optimization algorithms and incorporating heat exchanger models into the performance calculation

The optimization criteria used in the development and design of thermoacoustic devices depend on the application, as described in sections 2.1-2.2 (Refs. J1 and J8). Additional criteria may be required in novel applications as well as when coupling thermoacoustic prime movers with thermoacoustic, Stirling or pulse tube refrigeration systems. A systematic investigation and optimization of the coupling requires further study. Also, incorporating models of the heat exchangers into the design optimization algorithms will lead to further enhancement of the performance of thermoacoustic systems, which is essential in practical implementations.

3. PUBLICATIONS

3.1 Peer-reviewed journal papers

- J1. Wetzel, M., Herman, C., 1997, *Design optimization of thermoacoustic refrigerators*, International Journal of Refrigeration, Vol. 20, No.1, pp. 3-21.
- J2. Wetzel, M., Herman, C., 1998, *Accurate measurement of high-speed, unsteady temperature fields by holographic interferometry in the presence of periodic pressure variations*, Measurement Science and Technology, Vol. 9, No. 6, pp. 939-951.
- J3. Herman, C., Kang, E., Wetzel, M., 1998, *Expanding the applications of holographic interferometry to the quantitative visualization of complex, oscillatory thermofluid processes*, Experiments in Fluids, Vol. 24, pp. 431-446.
- J4. Wetzel, M., Herman, C., 1998, *Limitations of temperature measurements with holographic interferometry in the presence of pressure variations*, Experimental Thermal and Fluid Science, Vol. 17, pp. 294-308.
- J5. Wetzel, M., Herman, C., 2000, *Experimental study of thermoacoustic effects on a single stack plate - Part I: Temperature fields*, Heat and Mass Transfer, Vol. 36, pp. 7-20.
- J6. Wetzel, M., Herman, C., 1999, *Experimental study of thermoacoustic effects on a single stack plate - Part II: Heat Transfer*, Heat and Mass Transfer, Vol. 35, pp. 433-441.
- J7. Chen, Y., Herman, C., 2001, *A simplified model of heat transfer in parallel, flat-channel heat exchangers for thermoacoustic applications*, accepted for publication in Heat and Mass Transfer.

- J8. Travnicek, Z., Herman, C., 2002, *Optimization of thermoacoustic refrigerators for maximum cooling load*, in preparation.
- J9. Travnicek, Z., Herman, C., 2002, *Thermoacoustic refrigerator for the cooling of electronic equipment*, in preparation.

3.2 Invited and peer-reviewed book chapters

- B1. Herman, C., 1999, *Heat exchangers for thermoacoustic refrigerators: Heat transfer issues in oscillatory flow*, Energy Conservation through Heat Transfer Enhancement of Heat Exchangers, Editors: S. Kakac et al., NATO Advanced Science Institute Series E, Vol. 355, Kluwer Academic Publishers, Dordrecht, pp. 285-299, peer-reviewed and invited contribution.
- B2. Herman, C., 2000, *The impact of flow oscillations on convective heat transfer*, Annual Review of Heat Transfer, Editor: C.-L. Tien, Vol. XI, Chapter 8, pp. 495-562, invited contribution.
- B3. Herman, C., 2001, one section in the *Dictionary of Acoustics*, Editor: D. Basu, CRC Press, Boca Raton, invited contribution.

3.3 Conference papers

- C1. Herman, C., Wetzel, M., Leungki Y. S., 1995, *Visualization of oscillating temperature and flow fields in a thermoacoustic refrigerator*, Proceedings of the Seventh International Symposium on Flow Visualization, Seattle Washington, Begell House, Inc. New York, pp. 334-340.
- C2. Herman, C., Wetzel, M., 1995, *Design of a thermoacoustic refrigerator - a case study*, AES-Vol.35, ASME, pp. 195-203.
- C3. Wetzel, M., Herman, C., 1996, *Design issues of a thermoacoustic refrigerator and its heat exchangers*, ASME Proc. of the 31st National Heat Transfer Conference, HTD-Vol. 331, pp. 137-144.
- C4. Wetzel, M., Herman, C., 1996, *Parameter spaces and design optimization of thermoacoustic refrigerators*, AES-Vol. 36: 1071-6947, Proc. 1996 ASME IMECE, Symposium on Thermodynamics and the Design, Analysis and Improvement of Energy Systems, Atlanta, pp. 355-363.
- ASME Student Design Paper Award.
- C5. Wetzel, M., C. Herman, *Accurate measurements of temperature fields by holographic interferometry in the presence of pressure variations*, Proc. 8th Int. Symp. on Flow Visualization, Editor Ian Grant, Sorrento, Italy, Sept. 1998.
- C6. Chen, Y., C. Herman, 1999, *A simplified model of heat transfer in heat exchangers and stack plates of thermoacoustic devices*, Proc. National Heat Transfer Conference, Albuquerque, NM, Paper NHTC99-310, pp. 1-8.

3.4 Conference proceedings - abstract published

- C7. Herman, C., Bartscher, C., Wetzel, M., Volejnik, M., 1994, *Experimental visualization of heat transfer and fluid flow processes in a thermoacoustic device*, J. Acoust. Soc. Am, Vol. 96, No. 5, Pt. 2, pp. 3220-3221.
- C8. Herman, C., Wetzel, M., Volejnik, M., 1995, *Visualization of oscillating temperature and flow fields in the stack region of a thermoacoustic refrigerator model*, J. Acoust. Soc. Am, Vol. 97, No. 5, Pt. 2, p. 3410.

- C9. Herman, C., Wetzel, M., Wagner, J., 1995, *Holographic interferometry: An approach to study the unsteady temperature fields in the stack region and its neighborhood*, J. Acoust. Soc. Am., Vol. 98, No. 5, Pt. 2, p. 2962.
- C10. Wetzel, M., Herman, C., 1996, *Optimization of the performance of thermoacoustic refrigerators applying the short stack boundary layer approximation*, J. Acoust. Soc. Am., Vol. 99, No. 4, Pt. 2, p. 2559.
- C11. Wetzel, M., Herman, C., 1996, *Measurements of oscillating temperature fields in the stack region of a thermoacoustic refrigerator model*, J. Acoust. Soc. Am., Vol. 100, No. 4, Pt. 2, p. 2846.
- C12. Wetzel, M., Herman, C., 1997, *Heat transfer measurements in a thermoacoustic refrigerator*, J. Acoust. Soc. Am., Vol. 101, No. 5, Pt. 2, pp. 3021-3022.
- C13. Wetzel, M., Herman, C., 1997, *Design of a thermoacoustic refrigerator for visualization measurements*, J. Acoust. Soc. Am., Vol. 102, No. 5, Pt. 2, pp. 3071-3072.
- C14. Wetzel, M., Herman, C., 1998, *Heat transfer measurements on a single-plate thermoacoustic refrigerator*, 136th Meeting of the Acoustical Society of America, Norfolk, VA, Oct. 1998, J. Acoust. Soc. Am., Vol. 104, No. 3, Pt. 2, Sept. 1998.
- C15. Herman, C., *Conventional heat exchanger design methods and their applicability to thermoacoustics*, Acta Acoustica, Vol. 85, Suppl. 1, p. 86, 1999.

3.5 Dissertation

- D1. M. Wetzel, *Experimental investigation of heat transfer in a single-plate thermoacoustic refrigerator*, thesis defense scheduled July 14, 1998.

4. LECTURES AND PRESENTATIONS AT CONFERENCES

1. *Experimental visualization of heat transfer and fluid flow processes in a thermoacoustic device*, Herman, C., Bartscher, C., Wetzel, M., Volejnik, 128th Meeting of Acoust. Soc. Am, Austin, TX, Nov. 28-Dec. 2, 1994.
2. *Visualization of oscillating temperature and flow fields in the stack region of a thermoacoustic refrigerator model*, Herman, C., Wetzel, M., Volejnik, M., 129th Meeting of Acoust. Soc. Am, Washington, D.C., May 30-June 03, 1995.
3. *Visualization of oscillating temperature and flow fields in a thermoacoustic refrigerator*, Herman, C., Wetzel, M., Leungki Y. S., Seventh International Symposium on Flow Visualization, Seattle Washington, 1995.
4. *Design of a thermoacoustic refrigerator - a case study*, Herman, C., Wetzel, M., IMECE, San Francisco, November 1995.
5. *Holographic interferometry: An approach to study the unsteady temperature fields in the stack region and its neighborhood*, Herman, C., Wetzel, M., Wagner, J., 130th Meeting of Acoust. Soc. Am, St. Louis, MO, Nov. 27-Dec.01, 1995.
6. *Visualization of high-speed heat transfer phenomena*, Department of Mechanical Engineering, University of Maryland Baltimore County, Baltimore, December 8, 1995.
7. *A method of quantitative visualization of complex, unsteady thermofluid processes*, Herman, C., Kang, E., ASME Fluids Engineering Division Conference, San Diego, 1996.
8. *Design issues of a thermoacoustic refrigerator and its heat exchangers*, Wetzel, M., Herman, C., 31st National Heat Transfer Conference, Houston, TX, August 03-06, 1996.
9. *Parameter spaces and design optimization of thermoacoustic refrigerators*, Wetzel, M., Herman, C., IMECE, Atlanta, November 1996.

10. Optimization of the performance of thermoacoustic refrigerators applying the short stack boundary layer approximation, Wetzel, M., Herman, C., 131th Meeting of Acoust. Soc. Am, Indianapolis, IN, May. 13-17, 1996.
11. Measurements of oscillating temperature fields in the stack region of a thermoacoustic refrigerator model, Wetzel, M., Herman, C., 132th Meeting of Acoust. Soc. Am, Honolulu, HI. Dec. 02-06,1996.
12. Heat transfer measurements in a thermoacoustic refrigerator, Wetzel, M., Herman, C., 133th Meeting of Acoust. Soc. Am, State College, PA, June 15-20, 1997.
13. Design of a thermoacoustic refrigerator for visualization measurements, Wetzel, M., Herman, C., 134th Meeting of Acoust. Soc. Am, San Diego, CA. Dec. 1,1997.
14. Simultaneous measurement and visualization of oscillatory temperature and flow fields by holographic interferometry, Ecole Politechnique Federale de Lausanne, Lausanne, Switzerland, January 12, 1998.
15. Advances in the study of forced convection heat transfer processes using holographic interferometry, National Institute of Standards and Technology, Gaithersburg, MD, Feb. 3, 1998.
16. Cool sound - The history and future of thermoacoustic refrigeration, Baltimore Chapter of ASHRAE, Feb. 19, 1998.
17. Using temperature as tracer: new possibilities for an "old" tool - real-time holographic interferometry - in the study of high-speed thermofluid processes, University of Maryland, College Park, Feb. 27, 1998.
18. Thermoacoustic refrigeration, Women's Science Forum, Space Telescope Science Institute, Baltimore, Feb. 28, 1998.
19. Experimental investigation of thermoacoustic refrigeration, Colorado State University, Fort Collins, March 5, 1998.
20. Experimental investigation of thermoacoustic refrigeration, University of Florida, Gainesville, March 20, 1998.
21. Heat exchangers for thermoacoustic refrigerators: Heat transfer issues in oscillatory flow, invited lecture, NATO Advanced Study Institute series on Energy Conservation through Heat Transfer Enhancement of Heat Exchangers, May 25 - June 5, 1998, Cesme/Izmir, Turkey.
22. Quantitative visualization of high-speed convective heat transfer processes, Dynafloow Corporation, Baltimore, Sept. 1998.
23. Heat transfer measurements on a single-plate thermoacoustic refrigerator, 136th Meeting of the Acoustical Society of America, Norfolk, VA, Oct. 1998.
24. Quantitative visualization of high-speed heat transfer phenomena: Applications in thermoacoustics, The Jamie Whitten National Center for Physical Acoustics, University of Mississippi, Dec. 8, 1998.
25. Heat exchangers, conventional methods of heat exchanger design, and their role and applicability in thermoacoustics, The Jamie Whitten National Center for Physical Acoustics, University of Mississippi, Dec. 10, 1998.
26. Experimental investigation of thermoacoustic refrigeration, University of California at Los Angeles, Los Angeles, December 14, 1998.
27. Progress in the experimental investigation of thermoacoustic refrigeration, invited lecture, Thermoacoustics Review Meeting – TARM – organized by the Office of Naval Research, The Jamie Whitten National Center for Physical Acoustics, University of Mississippi, Jan. 7, 1999.

28. *Experimental investigation of thermoacoustic refrigeration*, Drexel University, Philadelphia, January 29, 1999.
29. *A simplified model of heat transfer in heat exchangers and stack plates of thermoacoustic refrigerator*, Joint Meeting: ASA/EAA/DEGA, Berlin, March 16, 1999.
30. *Thermoacoustic refrigerators: Design optimization and experimental investigation*, Reunion ThermoAcoustique, Meeting of the French Thermoacoustics Research group, Ecole Centrale de Lyon, France, March 24, 1999.
31. *Experimental investigation of thermoacoustic refrigeration*, Ecole Centrale Paris, France, March 26, 1999.
32. *Thermoacoustic refrigeration: Design optimization, experiments and miniaturization*, Rockwell Science Corporation, CA, April 12, 1999.
33. *Experimental investigation of thermoacoustic refrigeration*, NASA Glenn Research Center, Cleveland, OH, Sept. 8, 1999.
34. *Experimental investigation of thermoacoustic refrigeration*, Case Western Reserve University, Cleveland, OH, Sept. 10, 1999.
35. *Design optimization of thermoacoustic refrigerators*, Universite Pierre et Marie Curie (Paris 6) – CNRS - LIMSI, Orsay, France, June 7, 2000.
36. *Expanding the application of holographic interferometry to the measurement of high-speed, unsteady temperature distributions In the presence of pressure variations - application to thermoacoustics*, Universite Pierre et Marie Curie (Paris 6) – CNRS - LIMSI, Orsay, France, June 14, 2000.
37. *Experimental study of thermoacoustic effects on a single stack plate: temperature fields and heat transfer*, Universite Pierre et Marie Curie (Paris 6) – CNRS - LIMSI, Orsay, France, June 21, 2000.
38. *A simplified model of heat transfer in parallel channel heat exchangers and stack plates of thermoacoustic devices*, Universite Pierre et Marie Curie (Paris 6) – CNRS - LIMSI, Orsay, France, June 23, 2000.
39. *Performance of miniature thermoacoustic refrigerators*, Universite Pierre et Marie Curie (Paris 6) – CNRS - LIMSI, Orsay, France, June 26, 2000.
40. *Visualization of high-speed flow and temperature fields in the stack of a thermoacoustic refrigerator*, National Heat Transfer Conference Pittsburgh, August 20, 2000.
41. *Advances in the investigation of thermoacoustic refrigeration: modeling and experiments*, University of Michigan, Ann Arbor, January 19, 2001.
42. *Verbesserung thermoakustischer Kältemaschinen (Improving the performance of thermoacoustic refrigerators)*, Thermodynamics Colloquium, University of Hannover, Hannover, Germany, Nov. 23, 2001.
43. *Thermoacoustic refrigeration for electronics cooling*, Navy Electronics Cooling Workshop, US Naval Academy, Annapolis, MD, Feb. 26, 2002.
44. *Low-temperature applications of thermoacoustic refrigeration*, invited lecture to be presented at the NATO Advanced Study Institute on "Low-temperature and cryogenic refrigeration - fundamentals and applications", June 23 - July 5, 2002, Altin Yunus-Çesme, Izmir, Turkey.
45. *Refrigeration systems for low-temperature electronics*, invited lecture to be presented at the NATO Advanced Study Institute on "Low-temperature and cryogenic refrigeration - fundamentals and applications", June 23 - July 5, 2002, Altin Yunus-Çesme, Izmir, Turkey.

5. AWARDS AND HONORS DURING PROJECT PERIOD

During the project period both the co-PI, Cila Herman, and the graduate student employed on this project, Martin Wetzel, received awards which are listed below.

5.1 Awards: Cila Herman

Major awards

1. **Presidential Early Career Award for Scientists and Engineers: PECASE** - October 1997, Nominating agency: NASA. For details see under Grants and Contracts.
2. **National Science Foundation (NSF) - CAREER Award** - July 1997. For details see under Grants and Contracts.
3. **1996 Distinguished Faculty Award for Commitment to Undergraduate Research** - awarded by the Student Council of the Johns Hopkins University.
4. **National Science Foundation (NSF) - Research Initiation Award** - August 1993. For details see Grants and Contracts.

Awards, fellowships

Teaching

1. **Kenan Award for Innovative Projects in Undergraduate Education** - May 1995. *Development of an Experiment for Investigation of Forced Convection Heat Transfer.* Awarded by the Kenan Fund of the Johns Hopkins University.
2. **Subcommittee for Electronic and Distance Education** - SEDE and the Provost's Educational Technology Award Program: C. Herman and M. Karweit, January 1996. For details see under Grants and Contracts.

Research

1. **NATO fellowship** for participation as invited lecturer in the NATO Advanced Study Institute on Low-Temperature and Cryogenic Refrigeration - Fundamentals and Applications, June 23 - July 5, 2002, Altin Yunus-Çesme, Izmir, Turkey.
2. **Visiting Associate Professor**, Universite Pierre et Marie Curie (Paris 6), Paris, France, June 1 – July 3, 2000.
3. **Chief of Naval Research Visiting Scientists Program**: fellowship for the visit to the Jamie L. Whitten National Center for Physical Acoustics, The University of Mississippi, Dec. 7-11, 1998.
4. **NATO fellowship** for participation in the NATO Advanced Study Institute on Energy Conservation through Heat Transfer Enhancement of Heat Exchangers, May 25 - June 5, 1998, Cesme/Izmir, Turkey.
5. **NATO fellowship** for participation in the NATO Advanced Study Institute on Cooling of Electronic Systems, June 21 - July 2, 1993, Cesme/Izmir, Turkey.

5.2 Awards: Martin Wetzel

1. **Martin Wetzel**: Deutscher Akademischer Austauschdienst (DAAD - German Academic Exchange Organization) fellowship for graduate studies at the Johns Hopkins University, 1994/95 and 1995/96.
2. **Martin Wetzel**: ASME Student Design Paper Award for paper C3, 1996.

6. PROJECT PARTICIPANTS

6.1 Post-doctoral scientists

1. **Dr. Yuwen Chen**, *Modeling of heat exchangers for thermoacoustic refrigerators*, Sept. 1998 – Aug. 1999.
2. **Dr. Zdenek Travnicek**, *Design of miniature thermoacoustic refrigerators*, Nov. 2000 – April 2001, permanent position with the Institute of Thermomechanics, Academy of Sciences of the Czech Republic.

6.2 Graduate students

Ph.D. Students

1. **Martin Wetzel**, *Thermo-fluid mechanic study of thermoacoustic devices*, earned M.S. degree in Spring 1997, completed Ph.D. July 1998, currently with BMW Research, Munich Germany.

Students who have earned their M.S. degree

1. **Martin Wetzel**, *Research topic: Thermo-fluid mechanic study of thermoacoustic devices*, graduated in Spring 1997.
2. **Ozan Tutunoglu**, *Research topic: Design of a miniature thermoacoustic refrigerator*, graduated Spring 2000.

Graduate students - in collaboration with European universities

(Diploma Thesis at these universities approximately corresponds to a Masters Thesis)

I Technical University of Munich, Germany:

1. **Christoph Bartscher**, *Experimental investigation of thermoacoustic phenomena*, graduated June 1994.
2. **Michal Volejnik**, *Experimental investigation of a thermoacoustic refrigerator*, graduated February 1995.
3. **Joachim Wagner**, *Experimental investigations of the oscillating flow and temperature fields in a thermoacoustic refrigerator*, graduated January 1996.
4. **Markus Mohne**, *Experimental study of heat transfer in a thermoacoustic refrigerator*, graduated in Jan. 1997.
5. **Andreas Geishauer**, *Experimental measurements of temperature and pressure fields in a thermoacoustic refrigerator*, graduated August 1997.

II Fachhochschule Furtwangen, Germany:

1. **Daniel Herrmann**, *Design, instrumentation and initial experiments on a thermoacoustic stack and its heat exchangers*, graduated Sept. 1997.

II University of Lyon, France:

1. **Magali Brouillat**, *Pressure and temperature measurements in a thermoacoustic refrigerator model*, graduated in Dec. Oct. 1996.

7. ORGANIZATION OF CONFERENCES AND CONFERENCE SESSIONS

1. Session Organizer

The 32nd National Heat Transfer Conference, Baltimore, MD, August 8-12, 1997

Session I: Emerging Refrigeration Technologies, C. Herman Chair, O. Knio Co-Chair.

Session II: Transport Phenomena in Oscillatory Flows, C. Herman Chair, O. Knio Co-Chair.

2. **Session Chair** at NATO Advanced Study Institute on Energy Conservation through Heat Transfer Enhancement of Heat Exchangers, May 25 - June 5, 1998, Cesme/Izmir, Turkey.

3. Session Organizer and Session Chair

2 sessions at the 137th Meeting of the Acoustical Society of America, Berlin, 13-17 March, 1999

Session: Physical Acoustics: Thermoacoustics, 6 invited lectures, 16 papers.

4. The 33rd National Heat Transfer Conference, Albuquerque, NM, Aug. 15-17, 1999

Session Organizer: Session I: *Emerging Refrigeration Technologies*

Session II: *Transport Phenomena in Oscillatory Flows*

8. TECHNOLOGY TRANSFER

The design optimization algorithm developed by Wetzel and Herman (1997) was used as the starting point for the development of the MEMS thermoacoustic refrigerator in the project sponsored by the Rockwell Science Corporation.